DELFT UNIVERSITY OF TECHNOLOGY

Microstructure for Thermal Impedance Spectroscopy for Biofuel Composition Measurement

Bo Jiang

Microstructure for Thermal Impedance Spectroscopy for Biofuel Composition Measurement

by

Bo Jiang

Student number: 4495977

This work was performed in:

Electrical Instrumentation Laboratory

Department of Microelectronics

Faculty of Electrical Engineering, Mathematics and Computer Science

Delft University of Technology

DELFT UNIVERSITY OF TECHNOLOGY

FACULTY OF

ELECTRICAL ENGINEERING, MATHEMATICS AND COMPUTER SCIENCE

The undersigned hereby certify that they have read and recommend to the Faculty of Electrical Engineering, Mathematics and Computer Science for acceptance a thesis entitled:
"**Microstructure for Thermal Impedance Spectroscopy for Biofuel Composition Measurement**"
by
Bo Jiang
in partial fulfillment of the requirements for the degree of
Master of Science.

Dated: November 24, 2017

Supervisor: Dr. ir. R. F. Wolffenbuttel

Thesis Committee:

Dr.ir A. Bossche

Dr. ir. C. J. M. Verhoeven

Dr. M. Ghaderi

Abstract

Biofuel sensors for measuring the ethanol and gasoline concentrations in bio-ethanol blends, have been studied world-wide and currently used in engine management in Flex-Fuel cars fabricated by amongst others, Ford Motor Company. However, water that results from ethanol sugar cane is inevitable present in the ethanol blend and requires a sensor that is capable of measuring the full ternary ethanol/gasoline/water compostion.

This thesis presents design of biofuel sensors, which can be used for the determination of compositions of ternary liquid mixtures of ethanol, gasoline and water. Firstly, the technical background and societal relevance of this thesis are given. Subsequently, the different physical domains are introduced that are in principle suitable for liquid composition sensing, such as the electrical, the acoustic, the optical and the thermal domains. As a next step, the thermal domain was selected with injected heat flux, J_h, as the through parameter and the resulting temperature difference, ΔT, as the across parameter. The basic principle of thermal impedance spectroscopy by frequency scanning was presented. Next, the thermal equivalent circuit model was used to simplify the thermal problem by transferring the thermal issue into an electrical topic. The main design challenge is to have the heat injected into the liquid rather than the substrate and to have a temperature-difference measurement not affected by the presence of the thermally conductive substrate. Different design properties such as heater, sensors, doping level, heat efficiency improvement and thermopile optimization, are explained in detail. After the interpretation on design properties, the fabrication process is introduced in detail and followed by the fabrication results. Finally, measurement results were obtained and used for validating the simulations and model and for drawing the final research conclusions.

Acknowledgments

I would like to express my gratitude to my supervisor Dr. Reinoud Wolffenbuttel, who gave me the chance to do my graduation project in his group. He taught me not only the knowledge and skills on sensor design and development but the way and attitude of studying, researching and solving problems. Thanks also to Reinoud for inspiring me to participate in the Eurosensors conference, which was the unique and precious experience for a master student to publish and present a scientific paper. Many thanks to my daily supervisor Dr. Mohammadamir Ghaderi, without whom this thesis could never be achieved. With his help and support, I learned how to use simulation tool for finite element analysis and lithography layout design. Amir was also the one who fabricated the designed-device in the clean room of EKL (as known as DIMES). Also, he has always been so patient and helpful for my questions concerning simulation, design, measurement and of course, writing.

Moreover, I would like to thank Luke Middelburg for providing essential background and knowledge on this project in optical domain. I also want to thank Accel Prouza for providing data and suggestions, Dr. Pelin Ayerden for giving some useful suggestion and help on measurement, Zuyao Chang for packaging and gluing the sensors, Yu Xin for help on measurement. In addition, I want to thank the guys in master room on 15th floor, for the laugh we have and memory we share. I also want to thank my friends in Delft: Yixin shi, Yuzhu Yan, Meng Wang, Yang Qiao, Kangli Huang, Xianwei Zeng, Guanchu Wang, Dezhi Lin, Jiahan Lu, Jinyi Liu, Xuefei You, Yang Liu, Hao Fan, He Zhang. Life would be boring and troublesome without those friends. My thanks also go to those who ever helped me in the past two years and thesis committee for their precious time for attending my defence and valuable comment on this thesis.

I would like to acknowledge the support received from the Ford Poling Challenge.

Finally, thanks to my parents, for the love they give me and love is all I need.

Bo Jiang

Table of Contents

Table of Figures

Chapter 1. Introduction

This thesis describes the design of biofuel sensors, which can be used for the determination of the composition of ternary liquid mixtures. In this work, a thermal system is considered that is composed of a heater and a temperature sensor for measuring the liquid-specific thermal impedance. The unique definition of a ternary mixture requires two parameters, which could be the real and imaginary part of the thermal impedance at a carefully selected frequency or the magnitude for at least two frequencies. The most general approach is based on thermal impedance spectroscopy with a heater injecting an AC heat into the system and temperature sensors to measure the increase in temperature at that frequency. The real part and imaginary part of impedance correspond to the thermal conductivity and heat capacity respectively of the mixtures.

In this chapter, the motivation of this thesis is firstly described by stating the problems addressed in this thesis and is followed by the selection of energy domains which could be used to implement the measurement by impedance spectroscopy. Subsequently previous research on this topic is presented. Furthermore, the schematic diagrams of the basic structures of initial design thermos-resistors and thermopiles are described. At the end of this chapter, the organization of this thesis is given.

1.1 Motivation

The global ambition for fuel from renewable sources has led to the trend from fossil fuel to biofuels, which normally contain ethanol and gasoline. However, as the ethanol mostly comes from sugar cane and corn which typically result in water content [1], water composition depends on the organic sources which vary from countries to countries. Secondly, water might be added manually on purpose to increase the profits. Biofuel hence contains not only ethanol and gasoline, but also water .

The presence of water content causes mainly three problems: firstly, water might prevent the engine from starting up when the composition of water is large enough. Secondly, water in the fuel would causes incomplete combustion which yields more by-product such as carbon monoxide, carbon dioxide, solid carbon particles etc. Thirdly, fuel separation might occurs

when car sits for a while if the water composition is large enough, which would cause damage to the engine if the motor sucks up water into the engine [2].

In principle one could compensate the measurement result of an ethanol-gasoline sensor for water content in case water concentration is constant. This is indeed implemented in state-of-the-art capacitive E85 sensors. However, the water content in bio-ethanol produced from corn in the United States is different from Brazil that produced for sugar cane. Global trade in biofuel results in an uncertainty of water compositions in ethanol blend sold somewhere.

Bio-ethanol helps reduce carbon emission when mixed with gasoline because the vegetation that is used to make ethanol absorbs carbon dioxide while growing. In other words, ethanol is "cleaner" than gasoline. The environmental benefits have promoted the mixing of bioethanol and gasoline. Initially only 10 % (referred to as E10). This small amount of ethanol can be added to gasoline without any problem to the engine. At a later stage a high bioethanol mixture was introduced; E85 with 85% bioethanol. Cars able to drive on E85 need a special engine management system. Farmers like bioethanol, but many people worry about the use of farmland for biofuel production rather than growing food for people.

Literature [3] reports confirm a reduction of greenhouse gas emission by the use of bioethanol and a reduced use of non-renewable fossil fuel.

The use of bioethanol with a variable water content requires a sensor system that is suitable for measuring the volume fractions of a ternary mixture which consists of ethanol, gasoline and water. At least two parameters that depend on liquid compositions are needed. Moreover, these need to be as independent as possible (preferably orthogonally dependent) to uniquely determine the ternary composition. Physical effects are generally classified according to physical domain. For biofuel composition sensing, the electrical, acoustic, optical and thermal domains have interesting properties. As for electrical domain, electrical impedance and capacitance are chosen. Sound speed and viscosity are the most promising in the acoustic domain and absorbance spectroscopy in optical domain. Thermal conductivity and heat capacity in thermal domain appear very promising and are explored here.

1.2 Selection of the domain to be used in this project

In the previous subsection, different domains were found to be the possible candidates and capable of providing at least two orthogonal properties. There were studies before this thesis. The first was done by Giuseppe Lacerenca who had investigated the feasibility of using optical spectroscopy or dielectric spectroscopy [4] in 2012. The second was done by Luke Middelburg who had studied a number of different domains, such as the electrical, optical, thermal and mechanical domain [5] in 2016. and actually implemented an approach based on electrical impedance spectroscopy in combination with optical absorption spectroscopy in the Ultra-Violet spectral range. A project on optical absorption spectroscopy for biofuel composition sensing is actually on-going by Guanchu Wang in the same group at the Electronic Instrumentation (EI) Lab.

Lacerenca found out that it is possible to determine the ternary mixtures compositions by using impedance spectroscopy. His work confirmed that the measurement of the impedance of liquids, as the function for dielectric in an electrode/fuel interaction, has the advantages of robustness. However, a unique composition measurement should include the range of the relaxation frequencies of the components in the liquid, which is up to 20 GHz and is not very practical in an automotive. [3]. Optical spectroscopy for both near-infra-red (NIR) and Raman technique has the limitation of implementation because the use of at least two LEDs is rather expensive, and Raman technique also requires the use of high power laser to get the signal.

Middelburg's work showed that electrical impedance measurement up to 30MHz delivers only to one useful valuable parameter. Relaxation frequency of ethanol is around 2 GHz which reaches to Radio Frequency (RF) range, which is not practical to implement.

Based on the previous research, thermal impedance spectroscopy is chosen for this thesis due to the high selectivity of water according to Table 1.

Table 1.1: Thermal Properties of Liquids

Liquid	Thermal Conductivity [W/(mK)]	Specific Heat Capacity [kJ/(kgK)]
Ethanol	0.179	2.44
Gasoline	0.15	2.22
Water	0.58	4.18
E85	0.175	2.41

According to Table 1.1, the thermal properties, thermal conductivity and heat capacity, differ significantly from those of ethanol and gasoline. However, the table also indicates that the ratio between the two (and thus the ratio between the real and imaginary part of the impedance) is very different. Therefore, the separate measurement of the real and imaginary part of the impedance at given frequency would not be a promising approach. Therefore, full thermal spectroscopy is explored. The resulting sensor can be expected to have a higher selectivity of water to ethanol and gasoline as compared to the selectivity between ethanol and gasoline.

1.3 Initial structure

As indicated in section 1.2, thermal impedance spectroscopy stands out due to its high selectivity for water. Likewise, the initial idea of implementing should be introduced in this section about how to create a thermal domain.

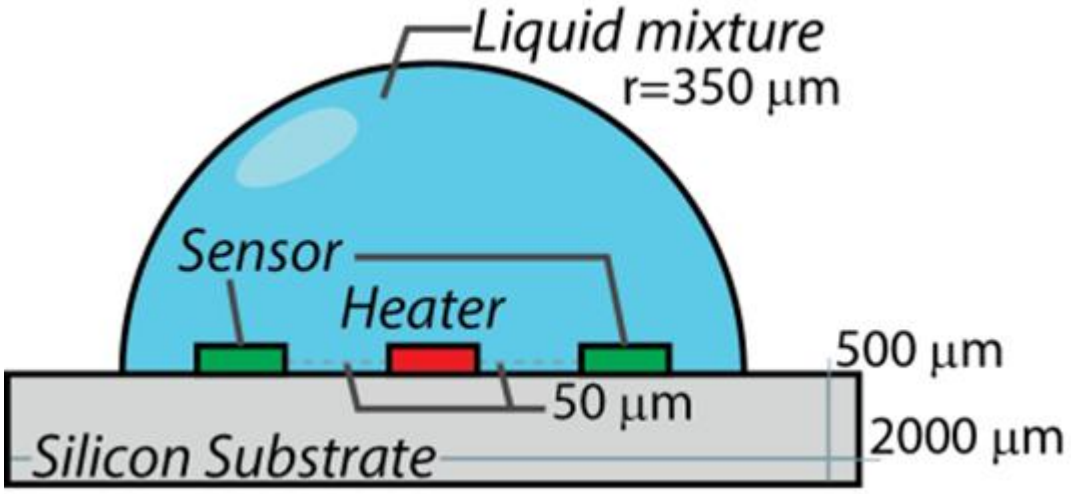

Figure 1: Schematic diagram of cross section of initial structure

The initial idea of a structural implementation of the thermal impedance spectroscopy sensor is shown simplified in Figure 1. The heater generates heat that is injected partially into the liquid and partially into the substrate. Two temperature sensors are used for measuring the resulting increase in temperature. The first is the heater itself and the other is placed 50 µm away from the heater. Two of these are used for symmetry reasons, as is discussed in detail in Chapter 3. The main design challenge of this project is to position the heater and sensors in such a way that most of the heat is injected into the liquid and that the substrate has minimum

effect on the temperature measurement. As also shown in Chapter 3, a CMOS-compatible micromachining technique is required for undercutting the structure in order to meet the requirements. Liquids mixtures that cover the heater and sensors are assumed to have the shape of a half sphere to the limit the calculation complexity of the simulation, and the radius is 350 μm for this half sphere [6].

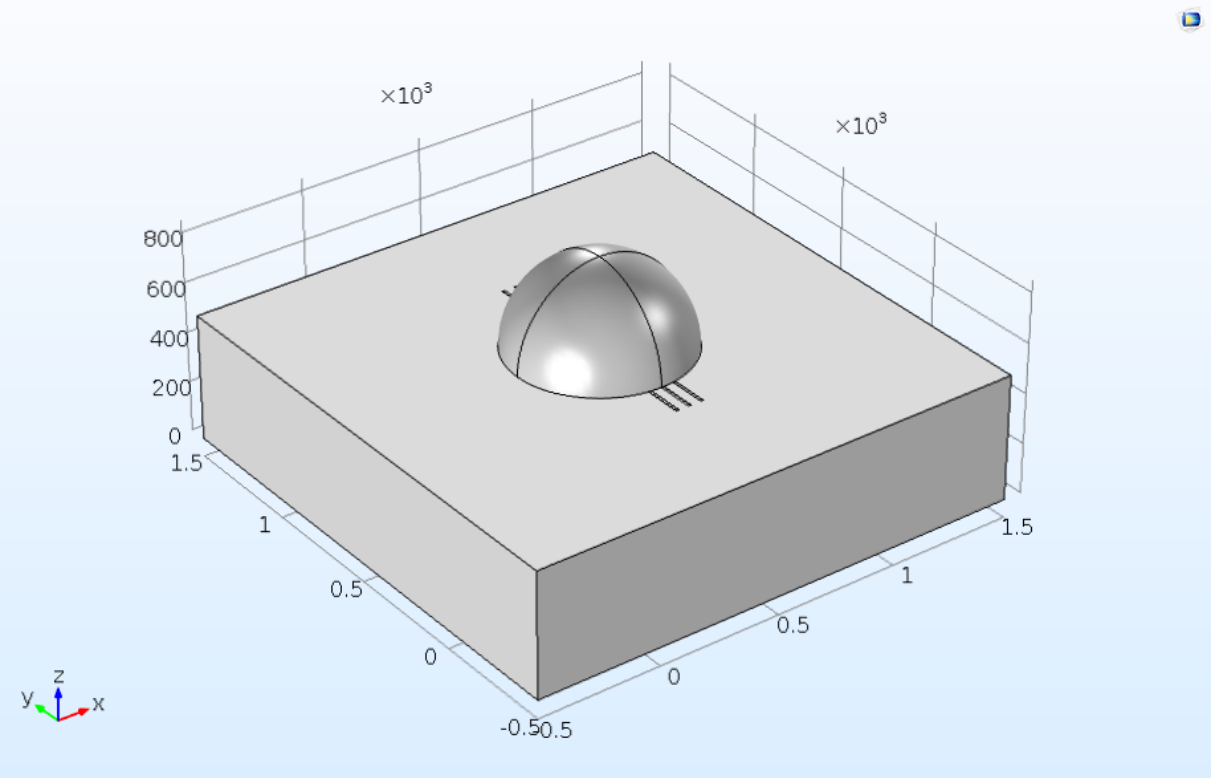

Figure 2: 3D view of initial structure

The 3D view of the initial structure is shown in Figure 2 corresponds to Figure 1. This Figure is made by COMSOL Multiphysics, which is a cross-platform finite element analysis simulation software that provides the foundation for this thesis.

1.4 Thesis Outline

This thesis design of a sensor structure for thermal impedance spectroscopy for measuring the ternary mixtures compositions of water, ethanol and gasoline.

Chapter 2 presents the overview of methods for composition measurement of liquids. Thermal impedance spectroscopy in liquids is introduced as an extension of thermal conductivity detector (TCD) in gas sensing. Moreover, electrical impedance spectroscopy, acoustic domain,

optical absorption spectroscopy, and thermal impedance spectroscopy are explained respectively for liquid sensing.

Chapter 3 firstly discusses the heater and sensor configuration which is investigated and used for optimizing detectivity. Subsequently, the concept of the thermal equivalent circuit is used to transfer the thermal problem to an electrical problem. In a next step the Seebeck sensor (thermocouple) is introduced as an alternative to the two-resistor temperature difference sensor. Furthermore, the effect of doping concentration in polysilicon layers on thermal coefficient, resistivity and Seebeck coefficient are investigated and used for optimizing detectivity. Specific issues, such as the 3ω technique for readout of temperature sensitive resistors is explained, followed by a comparison between frequency scanning and single frequency measurement. Structures are introduced for increasing the injection of heat flux into the liquid rather than the substrate. The lateral and vertical design optimization is done. Last but not the least, different thermopile structures are discussed as a possible technique for a higher sensitivity despite the also higher thermal conduction through the structure..

Chapter 4 describes the fabrication process of the designed sensors. Firstly, the overview layout of the lithography is introduced, introduced. Details are explained along with properties such as n/p doping, the width of thermopile, thermos-resistor and thermocouple etc. Then, the fabrication sequence is explained step by step to show how the sensors are fabricated in the clean room. Finally, the images under SEM are presented to show the fabrication results.

Chapter 5 presents the measurement results of resistivity, the temperature coefficient of resistance and second harmonic Seebeck voltage. Finally, the conclusion of this chapter is presented.

Chapter 6 depicts the main conclusions of this thesis and future works based on this thesis.

Reference

[1] Middelburg L M, de Graaf G, Ghaderi M, et al. Optical Spectroscopy for Biofuel Composition Sensing[J]. Procedia Engineering, 2016, 168: 55-58.

[2] https://www.revzilla.com/common-tread/ethanol-the-report

[3] Wang M, Saricks C, Santini D. Effects of fuel ethanol use on fuel-cycle energy and greenhouse gas emissions[J]. 1999.

[4] G. Lacerenza, A feasibility study of a sensor system to detect the amount of water and ethanol petrol, MSc. Thesis (2013)

[5] L. M. Middelburg, Bio-fuel composition sensing multi domain spectroscopy to determine the composition of bio-fuel mixtures, MSc. Thesis (2016)

[6] https://en.wikipedia.org/wiki/Drop_(liquid)

Chapter 2. Liquid Sensing

In Chapter 1, different domains of determining fuel compositions have been briefly analyzed. Compared to Chapter 1, these domains should be explained in detail about how the cutting-edge sensors have been developed recently in this chapter.

In this chapter, liquid sensing will be introduced to give an overview of the state-of-the-art fuel sensors that are used worldwide. Followed by the interpretations and comparison of using thermal conductivity detector (TCD) in the gas phase measurement. Moreover, different domains of spectroscopy will be explained extensively for the acoustic domain, electrical impedance spectroscopy and optical absorption spectroscopy. Last but not the least, the conclusion of this chapter will be explained.

2.1 Overview of liquid compositions sensing

In this subsection, an overview of fuel compositions sensing sensors will be introduced roughly to discuss the state-of-the-art sensors in different domains. Furthermore, the pros and cons of these sensors will be briefly explained to state the limitations. Available commercial fuel compositions sensors are typically based on dielectric constant [1][2], by measuring the capacitance at a constant frequency of 10 KHz. However, these sensors are only capable of determining the ethanol and gasoline compositions in binary mixtures instead of ternary mixtures. In operation a fixed water concentration is usually assumed to compensate for the water content present in the fuel [3]. Figure 3 shows a fuel sensor (Continental Flex) used by Ford Motor Company.

Figure 3: Fuel Composition (Flex Fuel) Sensor (E85) [4]

The Fuel Sensor is shown in Figure 3 the flex fuel sensor only measures the binary mixtures of gasoline and ethanol by measuring the impedance at a low frequency and sends an electrical signal to the engine control module to indicate ethanol percentage. The temperature sensor is embedded to compensate for temperature effects [5]. Similar to [1][2], a fixed composition of water content is also assumed, which does not agree on our intention of determining ternary mixtures.

As for dielectric constant measurement, water has a dielectric constant of 80, which is much higher than that of ethanol of 25 and gasoline of 2. Therefore, the existence of water strongly influences the dielectric constant of fuel mixtures. In other words, even a small change of water composition would result in a significant variation of dielectric constant of overall fuel. Assuming a constant water concentration leads to the uncertainty in determining full compositions.

The sensor shown in Figure 3 has an accuracy of $\pm$ 5% and resolution of 0.1% with the assumption that water concentration is constant. Some practical measurement has been carried out by Luke Middelburg [5] showed that the ethanol compositions would increase considerably if only 5% volume percent of water were present using this sensor.

Currently, no commercial fuel sensor or sensor system is available using a single domain that is capable of determining ternary mixtures. Thus, exploring the different domain of implementing measurement should be appealing and reasonable.

2.2 Electrical domain

Electrical impedance spectroscopy is based on the measurement of permittivity and dielectric as well as the resistance and capacitance of each fuel component concerning water, ethanol and gasoline. Many researches had been done so far and have been processing in the electrical domain. Santos [15] developed an impedance sensor for determining ethanol content in Brazilian gasoline using a portable electronic method. Furthermore, Rocha [16] developed an electric impedance sensor that embedded in ethanol and regular blends for determining mass ratios, which also measures the binary mixtures. Hofmann [17] developed a liquid composition sensor which measures the binary mixtures based on the determination of the capacitance and resistance of the electrode arrangement in fluids. In addition, Jafari [18] implemented an electrochemical impedance spectroscopy to investigate the corrosion

behaviour of metallic components of the fuel system. Wiziack [19] complemented an array of quartz microbalance sensors by an array of capacitors obtained from a commercial biometrics fingerprints detector, which quantify the ethanol content in gasoline.

As discussed in section 2.1, commercially available capacitive sensor [1][2] is developed by measuring the capacitance at a low frequency of 10 kHz. However, all these above-mentioned sensors are only capable of measuring the binary mixtures of ethanol and gasoline, which provides the necessity of developing a sensor that measures the ternary mixtures when water is present as it is an unavoidable component in ethanol/gasoline mixtures.

Recently, electrical impedance spectroscopy with a customized coaxial probe operating in the 10 kHz to 1 MHz frequency range was investigated and found out that electrical impedance spectroscopy only is not sufficiently accurate, because of the limited amount of spectral variability and poor quality of the conductivity measurement for ternary components [20]. Thus, additional information is required to unambiguously determine the composition of the ternary mixture via other possible domain.

2.3 Acoustic domain

The acoustic domain is implemented via surface acoustic waves (SAW), and some hands-on measurement using SAW device had been carried out by Luke Middelburg for the feasibility study [5]. SAW technique is based on the piezo electric effect which is the ability of certain materials to generate an electric response to applied mechanical. i.e. an interaction between the electrical domain and mechanical domain. Using piezoelectric effect for the application of sensors have been put into practice for a long time [13].

As for our case on fuel composition sensing, the propagation of the acoustic sound wave on the boundary exists between the deposited liquid (droplet in my case) on the device and the solid state material of the device itself [5]. Middelburg in his MSc. work [5] has studied the fuel composition using SAW sensors composed of two sets of interdigital transducers (IDTs) [14]. For the measurement, both IDTs are connected to a Vector Network Analyzer to measure the scattering of the acoustic wave in the liquid. Consequently, the speed of sound and density are acquired and total speed would be the average of the velocity of the waves through the device itself and liquid when a liquid with certain properties is deposited on the back of the SAW device.

However, none of the three liquid components is dominating the response [5]. Accordingly, no noticeable orthogonality is provided when using SAW technique. This result indicates the low sensitivity in acoustic domain, yet very useful for providing additional information that could be used for the combination with other domain such as electrical domain or optical domain. Besides, implementing acoustic technique in an automotive is not practical because of the presence of acoustic noise.

2.4 Optical Domain

A significant amount of works has been previously done by Middleburg [3][5][20] in optical spectroscopy domain. Besides, another on-going MSc graduation project which aims to the same target of determining ternary mixtures is investigated by Guanchu Wang.

According to [20], optical absorption spectroscopy in the UV spectral range between 230 and 300 nm was found to be the most appropriate range that gasoline is highly dominated in typical absorbance whereas ethanol and water are almost transparent because of the benzene absorption band in this part of the spectrum. Which makes the optical domain a promising candidate for determining gasoline content without the interference of ethanol and water.

Apart from that, Roy [21] presented an intrinsic intensity modulated fiber optic sensor for determining adulteration of petrol and diesel by kerosene. Lima [22] introduced a photo-thermal analysis for the detection of adulterants in gasoline via analyzing the vapour phase of fuel as changing the vapour compositions changes the thermal diffusivity in time. Yet, these sensors are also only capable of determining binary mixtures when water is absent or determining binary mixtures assuming the constant composition of water. Which actually does not fulfil our purpose of determining ternary mixtures when an unknown-composition of water is presented.

As indicated in Chapter 1, two orthogonal properties are required to determine the ternary mixtures. The well-known Thermal Conductivity Detector (TCD) could be used to measure the thermal conductivity of mixtures by measuring thermal conductivity and heat capacity of the fuel. However, most available TCD is used for gas phase measurement instead of liquid phase.

2.5 Thermal Conductivity

Most TCDs available in the market are used for gas phase in automotive industry and environmental monitoring [6]. These sensors that based on TCDs have the advantage of high-sensitivity, low-cost, as well as long-term stability.

The operation of a TCD is based on the specific gas thermal conductivity [6], which is measured in respect of temperature reduction in a heated element, due to the heat loss through gas. The heat loss is either through conduction or convection. The heat conduction is the phenomenon that happens when two or more objects are in physical contact. Heat is transferred in a body along a temperature gradient from the hottest part to the coldest part. In TCDs usually a temperature gradient is created via using heater.

Convective heat transfer, on the other hand, consists of two types of natural convection and forced convection [7]. Forced convection is negligible in case of micro-scale devices [8] because fuel is assumed to be still instead of flowing. Also, TCD is used for compositions measurement instead of flow measurement in this case. Furthermore, forced convection is caused by an external source like a pump or a suction device, and is not considered in this thesis.

The most common and simplest TCDs are the so-called hot-wire devices [9] where the hot-wire acts as a heater and temperature sensor at the same time. An electrical current is feed though the wire which further produces Joule heating, and depending on the surrounding gas, the temperature of the wire changes and can be detected as a change in resistance.

Recently, miniaturized TCD can be miniaturized enabling low sample volumes measurement and low fabrication cost [10]. Thanks to this miniaturization, many commercially available devices [11] have been developed based on thin metal sheets.

TCD which is partly used as physical gas sensor has the advantage of not suffering from chemical contamination, which makes them reliable and robust. Additionally, the use of gas sensor based on TCD has increased due to advances in the area of integrated circuit (IC) technology [12].

Liquid TCDs have the similar measurement principle, which requires electrical current feeding though the wire, and further produces Joule heating on surrounding liquid instead of gas, the temperature of the wire changes and can be detected as a change in resistance. State-

of-the-art liquid TCDs [23] have been developed for liquid sensing to measure the liquid water mass of collected aerosols.

2.6 Conclusion

As discussed in section 2.2-2.4. Current sensors operating at a single domain such as electrical impedance spectroscopy, acoustic domain, optical spectroscopy domain cannot provide enough and reliable information for determining full compositions of ethanol, gasoline and water. So, the ways of accomplishing this purpose are either exploring new domain that could be used to determining ternary mixtures simultaneously or combining at least two different domains that each domain resolve one composition measurement.

Middelburg chose the latter one in [3], which merges the information provided by low-frequency impedance spectroscopy with that of the optical absorption spectroscopy in the UV range since the optical absorption is highly selective for gasoline as well as the electrical impedance spectroscopy suits for water composition measurement. However, this sensor system that combines two domain is only in the stage of concept design and quantitative analysis validation as well as a few initial experiments validation using E85 assuming no water is presented. Therefore, the combined probe design and actual implementation are still on-going and soon to be achieved in the next stage, which could be regarded as the most promising method of resolving ternary mixtures problem except for this thesis work.

As an alternative approach, exploring thermal domain has been investigated and chosen in this thesis. Implementing thermal impedance spectroscopy will be explained thoroughly in the later chapters.

Reference

[1] McKay, Brian, et al. “An Onboard Ethanol Concentration Sensor for the Brazilian Market.” No. 2012-36-0249. SAE Technical Paper, 2012.

[2] Haft, Gerhard, and Rainer List. "Method and apparatus for determining the ethanol proportion of the fuel in a motor vehicle." U.S. Patent No. 8,387,445. 5 Mar. 2013.

[3] Middelburg, Luke, et al. "Combining impedance spectroscopy with optical absorption spectroscopy in the UV for biofuel composition measurement." Instrumentation and Measurement Technology Conference (I2MTC), 2017 IEEE International. IEEE, 2017.

[4] http://paceperformance.com/i-8396469-13577394-fuel-composition-flex-fuel-sensor-e85.html

[5] L. M. Middelburg, “Bio-fuel composition sensing multi domain spectroscopy to determine the composition of bio-fuel mixtures.” MSc. Thesis (2016)

[6] De Graaf, G., et al. "Micro thermal conductivity detector with flow compensation using a dual MEMS device." Sensors and Actuators A: Physical 249 (2016): 186-198.

[7] Abarca, A. N. "High Precision Flow Compensated Thermal Conductivity Detector for Gas Sensing with Read-out Circuit." (2015).

[8] Hu, Xuejiao, Ankur Jain, and Kenneth E. Goodson. "Investigation of the natural convection boundary condition in microfabricated structures." ASME 2005 Summer Heat Transfer Conference collocated with the ASME 2005 Pacific Rim Technical Conference and Exhibition on Integration and Packaging of MEMS, NEMS, and Electronic Systems. American Society of Mechanical Engineers, 2005.

[9] Bruun, Hans H. "Hot-wire anemometry-principles and signal analysis." (1995).

[10] http://www.xensor.nl/pdffiles/sheets/xen-tcg3880.pdf

[11] Boon-Brett, L., J. Bousek, and P. Moretto. "Reliability of commercially available hydrogen sensors for detection of hydrogen at critical concentrations: Part II–selected sensor test results." International Journal of Hydrogen Energy 34.1 (2009): 562-571.

[12] Manginell, Ronald P., James H. Smith, and Antonio J. Ricco. "An overview of micromachined platforms for thermal sensing and gas detection." Proc. SPIE. Vol. 3046. 1997.

[13] http://www.nanomotion.com/piezo-ceramic-motor-technology/piezoelectric-effect/

[14] Vellekoop, Michael Johannes. "A smart lamb-wave sensor system for the determination of fluid properties." (1994).

[15] Santos, Edval JP. "Determination of ethanol content in gasoline: theory and experiment." Microwave and Optoelectronics Conference, 2003. IMOC 2003. Proceedings of the 2003 SBMO/IEEE MTT-S International. Vol. 1. IEEE, 2003.

[16] Rocha, Marcelo da Silva, and J. R. Simões-Moreira. "A simple impedance method for determining ethanol and regular gasoline mixtures mass contents." Fuel 84.4 (2005): 447-452.

[17] Hofmann, T., et al. "Fluid characterization using sensor elements based on interdigitated electrodes." Sensors and Actuators B: Chemical 37.1-2 (1996): 37-42.

[18] Jafari, Hassan, et al. "EIS study of corrosion behavior of metallic materials in ethanol blended gasoline containing water as a contaminant." Fuel 90.3 (2011): 1181-1187.

[19] Wiziack, Nadja Karolina Leonel, et al. "A sensor array based on mass and capacitance transducers for the detection of adulterated gasolines." Sensors and Actuators B: Chemical 140.2 (2009): 508-513.

[20] Middelburg, L. M., et al. "Multi-domain spectroscopy for composition measurement of water-containing bio-ethanol fuel." Fuel Processing Technology 167 (2017): 127-135.

[21] Roy, Sukhdev. "Fiber optic sensor for determining adulteration of petrol and diesel by kerosene." Sensors and Actuators B: Chemical 55.2 (1999): 212-216.

[22] Da Costa, Renata S., et al. "A novel strategy to verification of adulteration in alcoholic beverages based on Schlieren effect measurements and chemometric techniques." Microchemical journal 78.1 (2004): 27-33.

[23] Lee, Chung-Te, and Shih-Yu Chang. "A GC-TCD method for measuring the liquid water mass of collected aerosols." Atmospheric environment 36.11 (2002): 1883-1894.

Chapter 3. Structure Design

As concluded from Chapter 2, thermal domain is chosen as the topic of this thesis. A schematic of a microsystem for thermal impedance spectroscopy was presented in section 1.3. This chapter discusses the design of a MEMS TCD with an emphasis optimize the structure to fulfill the requirement of ternary compositions determination.

Firstly, different configurations of heater and sensor are introduced to give the initial idea of the design, as well as the measurement technique such as 3ω technique. Secondly, the thermal equivalent circuit model is introduced to simplify the thermal problem and derive the frequency response. Thirdly, the theory of thermos-resistor and thermopile are introduced. Afterward, doping of structures is discussed since doping influence several parameters such as resistivity, Seebeck coefficient, and temperature coefficient of resistance. Sequential finite element modeling was used to increase the heat flux efficiency vertically and horizontally, several critical design properties are discussed to optimise the structure design. Finally the design of the thermopiles was optimized to minimize the temperature difference between hot junction and the heater.

3.1 Heater and Sensor Configurations

A TCD determines the composition of the liquids by measuring the thermal properties of the liquid. Thermal conductivity and heat capacity are the fundamental material properties and easiest measurable thermal properties because they are correspond to amplitude and phase in the signal. Thermal conductivity is the property of a material to conduct heat, in the unit of watts per meter-kelvin ($W/(m \cdot K)$). While heat capacity is extended to heat capacity at constant pressure, also known as specific heat, which is the amount of heat per unit mass required to raise temperature by kelvin ($J/(kg \cdot K)$). In this thesis unless otherwise indicated, the heat capacity and specific heat has been used.

In order to measure the thermal properties of liquids, thermal domain should be created by feeding electrical power though electrical-conductive resistive strip, heat would then be generated and goes through the surrounding-liquids, finally ends up at sensor.

Passing a current through a resistive strip generates heat and can be used as the heater in the TCD design. On the other hand, the resistivity of a resistive strip often depends on the

temperature. Therefore, a resistive strip can also be used as a temperature sensor in the thermo-resistor configuration. Heater and sensor could either be designed as a single resistive strip or multiple parallel strips. In general, all combinations could be concluded in Figure 4.

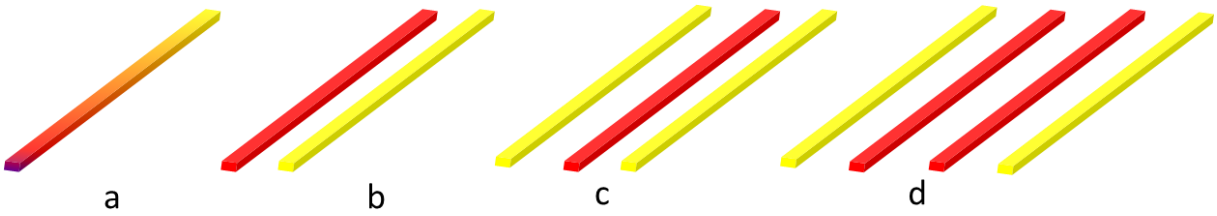

Figure 4: Red indicates the heater whereas yellow indicates the sensor: a) single heater/sensor configuration; b) single heater and sensor place parallel separately; c) single heater with two sensors placed in parallel; d) two heaters with two sensors.

Many literatures [1-8] show a promising way of measuring the thermal properties (thermal conductivity and heat capacity) of liquids by using ac heating technique such as three-omega technique in a single heater/sensor configuration (Figure 4.a). Transient hot-wire method is regarded as one of the standard techniques to determine the thermal conductivity and diffusivity of fluid sample [9].

The ac heating technique has several advantages over the conventional dc heating technique [8]. Firstly, the penetration depth of the thermal wave is small, it requires relatively small volume of the liquid sample. Secondly, the signal is more sensitive to the variation of the thermal properties of samples [14] and less severely affected by fluid flow [7] than the dc technique. In addition, the ac technique is also noise-resistant because the sensor signal is selectively acquired at a specific heating frequency. However, single wire ac-heating technique cannot provide big enough signal since 3ω technique is used and amplitude of 3ω is normally thousand times lower than amplitude of 1ω.

For transient hot-wire method [9], a thin metallic wire, typical centi-meters in length, is immersed in the sample fluid and electrically heated while monitoring the resistance variation for the thermal response. However, the size of the wire is relatively large which means that this method requires relatively large volume of liquids (at least hundreds of milliliter), which restrains the application of the device and eliminates the possibility of measuring low-volume. Furthermore, transient hot-wire method is not yet proved to be capable of measuring the heat capacity of liquids and it is not robust enough either [8]. In conclusion, hot-wire method is not suitable for single heater/sensor thermal properties measurement because it is not flow resistant.

3.1.1 3ω technique

The 3ω method is introduced in [10], which was applied to bulk amorphous solid and crystals as well as amorphous films tens of microns thick. The 3ω technique uses a radial flow of heat from a single element that is used both as a heater and thermometer(sensor), as shown in Figure 4 (a). The major difference between the 3ω technique and hot-wire as well as hot-strip [11] is use of the frequency dependence of temperature oscillations instead of the time domain response. Frequency dependence would be preferred when thermal impedance spectroscopy of the biofuel is needed because frequency variation is easier to implement.

The basic theory of 3ω technique is feeding an AC current at angular frequency ω through the strip. The consumed power hence generated heat in the resistive strip can be calculated as:

$$P = I^2R = {I_o}^2 \sin^2(2\pi\boldsymbol{\omega}t) \times R = {I_o}^2 \frac{1-\cos(2\pi\times\boldsymbol{2\omega}t)}{2} \times R \quad (3.1)$$

where $I = I_o\sin(2\pi\boldsymbol{\omega}t)$ is the AC current that goes though the heater.

Therefore, heat is generated at the heater at the angular frequency of 2ω. This heat further induces a temperature fluctuation, which can be measured through the heater's resistance (R).

$$R(\boldsymbol{2\omega}) = R_{ref}\left[1 + \alpha\left(T - T_{ref}\right)\right] = R_{ref}[1 + \alpha\Delta T(\boldsymbol{2\omega})] \quad (3.2)$$

where α is temperature coefficient of resistance.

Measuring the voltage across the heater element shows a third harmonic component due to the temperature fluctuation.

$$V(\boldsymbol{3\omega}) = I(\boldsymbol{\omega}) \times R(\boldsymbol{2\omega}) = \{I_o sin(2\pi\boldsymbol{\omega}t)\} \times \{R_{ref}[1 + \alpha\Delta T(\boldsymbol{2\omega})]\} \quad (3.3)$$

Finally, measuring the amplitude and phase of this 3ω voltage would lead to the results of thermal conductivity and heat capacity of liquids, which can further be used for determining ternary mixtures of biofuel after calculations.

The multiple resistive strip configuration shown in Figure 4 b-d can be used to measure the temperature fluctuations at locations further away from the sensor. This provides extra information needed for the characterization of ternary mixture.

The main difference between single heater/sensor and separate heater and sensor configuration is that another relatively small current at angular frequency of ω needs to be used in sensor(s), and the amplitude of this current should be relatively small compared to the

initial ω current in heater which shows in Equation (3.1). So temperature fluctuation that generated at sensor due to this current could be ignored compared to the temperature fluctuation due to heater. Therefore, Equation (3.3) would also applies but the only difference is that the I_o in this Equation should be changed into another small value whereas the phase remains the same. In this way, Equation (3.2) should be applied both to heater and sensor, while Equation 3.3 would only need to be applied to sensor.

As for the configuration of Figure 4 (b-d), extra current(s) is needed in the sensor, which makes the measurement more complicated. However, heater-sensor-separation gives extra information because in this case, heater uses 3ω technique with or without separate sensor(s), and temperature at sensor and heater could be measured via measuring the resistance of heater and senor, which gives the temperature difference. Whereas single/heater only results in one temperature result.

As for the configuration of Figure 4 (b) and (c), configuration (c) has two symmetric sensors placed at the same distance away from heater, whereas (b) has only one sensor. Configuration (b) is more sensitive to the liquid flow since any liquid flow would lead to the heat transfer in a certain direction and further lead to temperature distribution uneven and influence the temperature measurement.

However, the configuration of Figure 4.c is less sensitive to liquid flow in perpendicular to the heater and sensor. Left sensor would have the higher temperature than the right sensor if liquid is flowing right perpendicular to the heater and sensors from left to right, or any direction except the direction of parallel to the heater. As for the direction of parallel-to-heater, heat would only transfer in parallel then two sensors would still have the same temperature since sensors are placed at the same distance away from and in parallel to the heater. The configuration of Figure 4.d is more complicated than the rest, and the mismatch of heat that generates at two heaters would easily cause the unevenly heat distribution.

In conclusion, the configuration of Figure 4 (c) is superior to (a) and (b) in terms of resistant to liquid flow, (d) in terms of simplicity.

3.1.2 Frequency-scanning method versus Single-frequency Method

In the previous section, the configuration of Figure 4 (c) is proved to be the most promising configuration to measure the thermal properties of liquids by using the 3ω technique at ac technique.

However, as introduced at the beginning of Chapter 1, two methods [8] could be used for ac technique. First method is single-frequency method, only one certain optimised value of frequency is used for the measurement. The signals of this method are more sensitive to the change of the thermal conductivity than that to the change in the heat capacity [1]. Instead of obtaining the thermal response at various frequencies, the voltage signal at a single optimum frequency is acquired by the sensor. Then, either the amplitude or the phase of the voltage signal, at the frequency is used. However, the fact that either amplitude or phase can be acquired does not give enough information to determine ternary compositions since both amplitude and phase need to be determined.

The second method is frequency-scanning technique. In this method, the temperature oscillation of the heater is scanned at various frequencies instead of one single frequency. Assuming that the length of the heater is far larger than the penetration depth of the thermal waves, the thermal conductivities of the fluid and substrate can thus be obtained from the slope of the curve relating ln ω to ΔT_{real} [1].

Compare frequency-scanning method with single-frequency method, frequency-scanning takes relatively long response time to obtain the thermal conductivity of the mixtures because the signal is acquired at several frequencies to get the slope [8], and the signal at each frequency has to measured separately. Whereas in single frequency method, only a single measurement is obtained.

In conclusion, 3ω technique of frequencies-scanning is used for configuration of Figure 4 (c) due to the limitation of single-frequency technique. In addition, absolute temperature of heater and sensor could be separately measured by measuring the resistance because the resistance changes according to the temperature, which will be explained in detail in later section.

3.2 Thermal Equivalent Circuit

In section 3.1, the basic theory of measuring ternary mixtures concentrations using thermal impedance spectroscopy is discussed. In this method is based on feeding ac current through a resistive strip and creating heat that injects into surrounding liquids, heat further ends up in sensor and change the temperature of the sensor. The thermal conductivity and heat capacity are measured during this process as the heat propagates through the liquid between heater and sensor.

Heater, sensors are fabricated on a silicon substrate. Silicon wafers are low cost and commonly used in semiconductor and MEMS technology. Besides, the heater and sensor should be made of silicon or polysilicon with certain doping level. Furthermore, the reason why we use polysilicon is that the temperature coefficient of resistance (TCR) and other properties of silicon can be tuned by doping. The effect of doping at different properties will be discussed in the later section. The cross section of structure is shown in Figure 5.

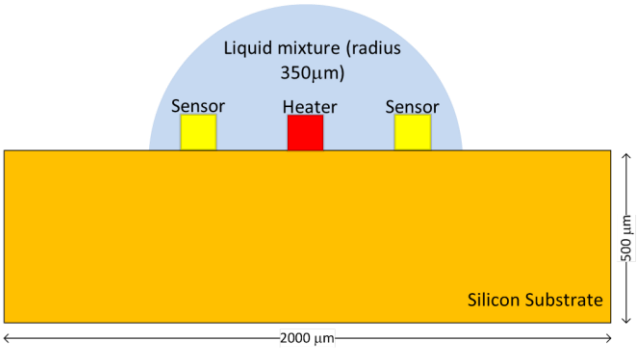

Figure 5: Cross section of initial structure

In Figure 5, AC operated resistive heater (red block), and another two resistive strips (light-yellow boxes) at a well-defined spacing for measuring the in-phase and quadrature components of the resulting AC temperature difference. For the reason of symmetry, two sensors are placed at the same distance away from the heater. It is assumed that the liquid mixture (shown here as a half-sphere) fully covers the heater and sensors.

In order to analyze how the heat transfers in the thermal domain, thermal properties of liquids and substrates and sensors should be used to determine heat transfer.

Table 3.1: Thermal Properties at room temperature.

Liquid and Solid	Thermal Cond. [W/(mK)]	Specific Heat Capacity [kJ/(kgK)]
Ethanol	0.179	2.443
Gasoline	0.15	2.22
Water	0.58	4.182
E85	0.175	2.41
Air	0.026	1.005
Silicon	130	0.7
Polysilicon	34	0.678

Table 3.1 shows the thermal properties of liquids and substrate. E85 is assumed to be composed of 85% ethanol 15% gasoline, E85 and Air are added for the use of next sections. The thermal conductivity of polysilicon is assumed be 34 W/(mK) temporary for the sake of convenient of calculation, but it depends on the doping level which will be discussed in the later sections. However, these values of thermal properties can give us neither intuitive results nor other useful information concerning heat flux and etc. Therefore, these thermal properties wouldn't be useful until it has been transferred into other domain which electrical engineers are familiar with, such as electrical domain. The parameters in electrical domain that corresponds to thermal conductivity and heat capacity are resistance and capacitance.

The thermal equivalent circuit should be discussed before the calculation of electrical resistance and capacitance because it would only make sense to see how the branches look like before finding out the actual values of each branch.

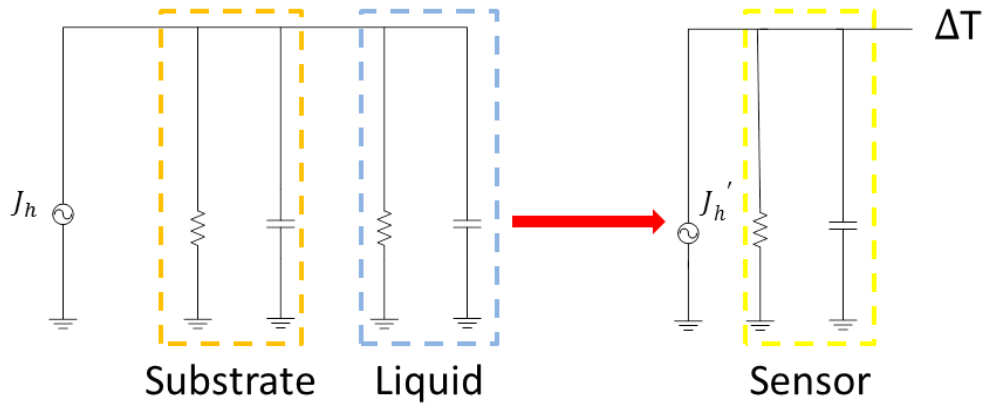

Figure 6: Thermal equivalent circuit (initial)

As shown in Figure 6, the heat that generates at heater is simplified as the current from current source of J_h, while ΔT is temperature oscillation change at sensor due to heat transfer. So all heat that generates at heater goes into the substrate, liquids in Figure 5 can be regarded as current that goes into substrate and liquids branches in Figure 6. Furthermore, as shown in Figure 5, sensor is heated up by substrate and liquids, which means that liquids and substrate have become a new heater, J_h' , that heats up sensor in Figure 6.

In Figure 6, as heat is regarded as current, each branches' resistor is proportional to the reciprocal of thermal conductivity, because the higher thermal conductivity is, the lower the resistance each branch become, and more current would flow into. This also makes sense because the reciprocal of thermal conductivity is called thermal resistivity, and one simple physical fact is that the heat would rather go into the material with higher thermal conductivity. This also explains why each branches should be in parallel, then the branch with lower resistance (higher thermal conductivity) gets more current (heat).

It is vitally important to mention that not all heat in liquids and substrate goes into the sensor, so there is a heat transfer ratio of the heat in liquids as well as the substrate to heat that goes into the sensor. In Figure 6, it is represented as a red arrow which can be regarded as a Current-controlled current source.

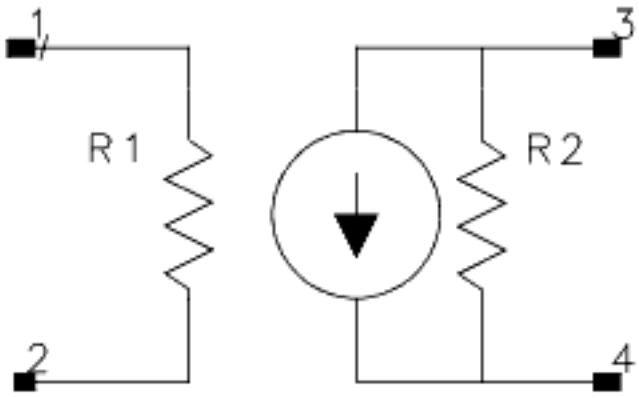

Figure 7: Linear Current-Controlled Current Source

Current-Controlled Current Source (CCCS)is shown in Figure 7 [15], and current source in Figure 7 is also the current source in Figure 6 for J_h'. There is a current gain in Figure 7 for CCCS that defines the ratio of current between mode 1 and mode 2 in R1 to the current between mode 3 and mode 4. This gain in Figure 7 is also the red-arrow-ratio in Figure 6, the difference is that this ratio is far less than 1 in Figure 6, but normally equal or more than 1 in Figure 7.

Another important feature to mention is that the heat which goes into sensor mostly come from substrate than liquids due to the large thermal conductivity of silicon substrate, which means that the substrate contributes much more than liquids in terms of heating up sensors. Therefore, there should be two different ratios for the heat transfer in Figure 6, one for the heat transfer ratio of substrate to sensor, another ratio of liquids to the sensor. However, thermal equivalent circuit is only a rough model to show heat transfer more intuitive and somehow quantify, so it does not have to be extremely accurate and Figure 6 would become relatively reliable.

In this model, liquids is a half-sphere for droplet with a radius of 350 μm in Figure 5; heater and sensors have the length of 1000 μm, the width of 10 μm and the height of 1 μm; while substrate silicon has the length of 2000 μm, width of 2000 μm and height of 500 μm.

Furthermore, calculation of resistance (R) and capacitance (C) in Figure 6 can be derived from Table 3.1 and these dimensions as well as the physical properties. The thermal conductivity and heat capacity in the thermal domain can be regarded as resistor and capacitor respectively and determine the liquids-specific low-pass frequency in a frequency scan.

The resistance in Figure 6 can be calculate as:

$$R = \frac{1}{k} \cdot \frac{L}{A} \tag{3.4}$$

Where k is the thermal conductivity ($W/(m \cdot K)$) so 1/k can be regarded as electrical resistivity in resistance definition, and L is effective length where temperature reaches to its -3dB point, A is the cross-sectional area of thermal conduct.

As for capacitance:

$$C = C_p \cdot \rho V \tag{3.5}$$

Where C_p is the heat capacity at constant pressure, ρ is the density of material, and V is effective volume of heat transfer.

For instance for the droplet of water,

$$R = \frac{1}{k} \cdot \frac{L}{A} = \frac{1}{0.58} \cdot \frac{350 \times 10^{-6}}{2\pi(350 \times 10^{-6})^2} = 784.01 \left[\frac{K}{W}\right]$$

$$C = C_p \cdot \rho V = 4182 \times 1000 \times \left(\frac{1}{2} \cdot \frac{4}{3}\pi(350 \times 10^{-6})^3\right) = 3.755 \times 10^{-4}\ [\frac{J}{K}]$$

The same method was applied to calculate resistance and capacitance for different components and the results are presented in Table 3.2.

Table 3.2: Thermal Properties and Electrical Properties at room temperature.

Liquid and Solid	Thermal Cond. [W/(mK)]	Specific Heat Capacity [kJ/(kgK)]	Electrical Resistance [K/W]	Electrical Capacitance [J/K]
Ethanol	0.179	2.443	2540.38	1.730×10^{-4}
Gasoline	0.15	2.22	3031.52	1.433×10^{-4}
Water	0.58	4.182	784.01	3.755×10^{-4}
E85	0.175	2.41	2598.44	1.685×10^{-4}
Air	0.026	1.005	***	***
Silicon	130	0.7	0.9615	3.26×10^{-6}
Polysilicon	34	0.678	***	***

In Table 3.2, electrical properties are extended compared to Table 3.1, these electrical properties are calculated from Equation 3.4 and 3.5, to determine the possible frequency range for the thermal equivalent circuit in Figure 6.

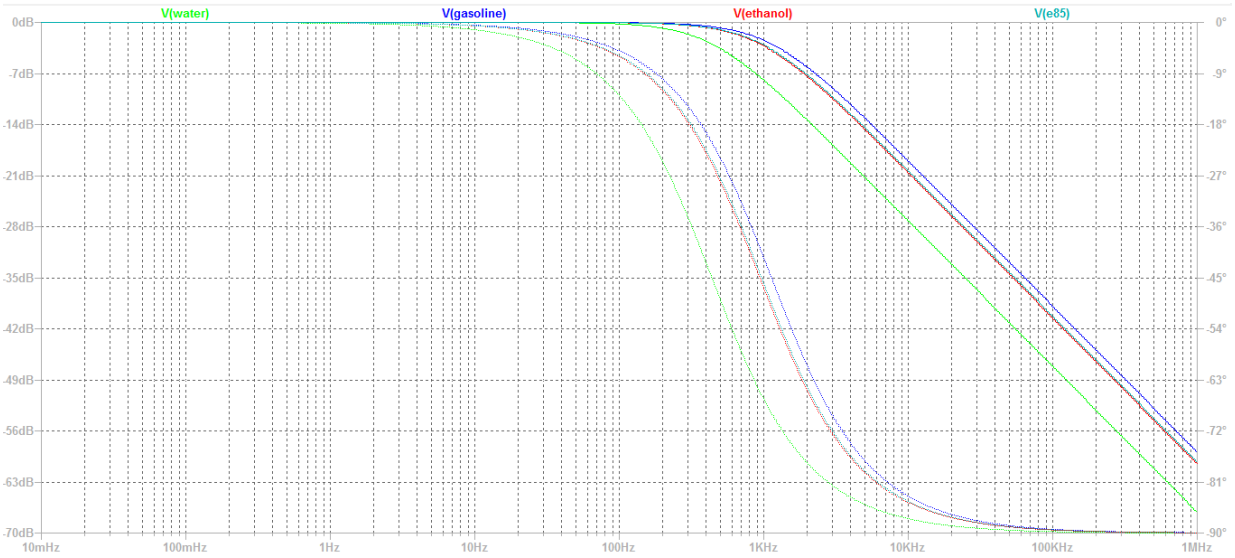

Figure 8 Frequency responses of thermal equivalent circuit with different liquids

Figure 8 is plotted by LTspice on the basic of Figure 6 and Table 3.2, different liquids such as water, gasoline, ethanol and E85 are plotted for the comparison. Two very important conclusions can be drawn from this Figure. Firstly, the bandwidth of each liquids is at few hundreds Hertz, and secondly, each liquids frequency responses are quite close to each other, which makes the sensitivity quite low, meaning that change of compositions would not be very recognizable for the system.

It is very important to mention that the values of frequency response in Figure 8 are not trustworthy mainly because the resistance and capacitance's values for calculation are not in the unit of Ohm and Farad but Kelvin per Watt and Joule per Kelvin. However, the curves show the first-order low-pass system theoretically which will be proved in the later sections with actual simulation of temperature-frequency-response.

The cut-off frequency of system for Figure 3 could be written as:

$$f_{cut-off} = \frac{1}{2\pi R_{total} C_{total}} \tag{3.6}$$

Taking water for instance, the cut-off frequency can be calculated as

$$f_{cut-off_{water}} = \frac{1}{2\pi R_{total} C_{total}} = \frac{1}{2\pi \times 0.96 \times 3.785 \times 10^{-4}} \approx 438\ Hz$$

Which fits the frequency response curve in Figure 8.

And according to Table 3.2 and Figure 6, it is clear that the total resistance (R_{total}) is limited by the resistance of substrate since the resistance of substrate is much lower than the resistance of liquids, and total capacitance (C_{total})is limited by the capacitance of liquids because the capacitance of liquids is significantly larger than the capacitance of substrate. Therefore, in order to increase the sensitivity of liquids, the best way of solving this would be increasing the resistance of substrate.

Furthermore, the ways of increasing the resistance of substrate according to Equation 3.4 could be increasing the effective length where temperature reaches to its -3dB point as well as decreasing the cross section area of thermal conduct. However, these two parameters are hard to change unless the size of structures changes, and the change of length and cross section can only be tuned slightly which means that a significant improvement of resistance of substrate cannot result from effective length of cross section area. Besides, decreasing the thermal

conductivity of the substrate is a practical method to implement because many materials have relatively lower thermal conductivity than silicon.

However, increasing the resistance of substrate without changing the resistance of liquids means that the cut-off frequency would also decreases, and further bandwidth of frequency response would decreases as well.

In conclusion, increasing the sensitivity could be achieved by increasing the resistance of substrate, and essentially decreasing the thermal conductivity of substrate, but bandwidth of frequency would also decrease. So compromising decision should be made to find the best suitable solutions to avoid much heat goes into the substrate and increase the sensitivity of liquids, as well as keep the bandwidth of frequency response in a reasonable range.

3.3 Design of Heater and Sensor

In section 3.1, the configuration of Figure 4 (c) turned out to be the best compromised configuration as heater and sensors are separately used in terms of flow-resistant and temperature measurement. However, the detail information of heater and sensor have not been discussed yet. Therefore, the basic theories of thermos-resistor and thermopile as well as its measurement technique will be discussed in this section.

Electrical power is feeding through the polysilicon resistive strip, heater, to generates heat, and temperature at heater and sensors can both be measured as showed in Figure 4 (c). These heater and sensors are called thermos-resistor because the resistance is depending on the absolute temperature (Kelvin) as

$$R = R_{ref}[1 + \alpha(T - T_{ref})] \tag{3.7}$$

Where R is the resistance at temperature "T"; and R_{ref} is the resistance at reference temperature T_{ref}, usually at room temperature of 293.15 K; α is temperature coefficient of resistance for the material; T is temperature in Kelvin.

The absolute temperature of heater and sensors are separately measured by using Equation 3.7 via measuring the resistance of the strips, then temperature difference between heater and sensors can be derived. The temperature difference varies because of the different thermal

conductivity of liquids, temperature response time at sensor varies because of the different heat capacity of liquids.

Apart from the thermo-resistor, thermopile is used to measure the temperature difference directly. Thermopile operate based on the thermoelectric effect which was discovered in 1821 by Seebeck. It has been found that a thermocouple, or rather some thermocouples forming a thermopile, can be used to measure very small temperature differences in a silicon chip very accurately [16][17].

Seebeck effect is the conversion of heat directly into electricity at the junction of different types of wire [18], and the basic theory of Seebeck effect can be showed in Figure 9.

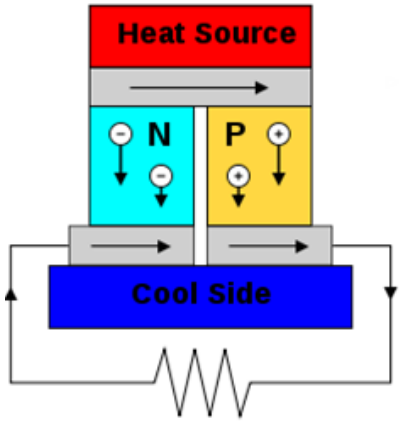

Figure 9: Semiconductor Thermoelectric Power Generator [18]

Figure 9 shows a thermoelectric circuit composed of materials of different Seebeck coefficient (p-doped and n-doped semiconductor). The heat source creates a temperature gradient where the place closer to heat source has higher temperature and areas far away the heat source has relatively lower temperature. The temperature difference between these two places creates Seebeck voltage. This Seebeck voltage can be easily measured with the read-out circuit which will be discussed in the later chapters.

In our case, the diagram should looks like Figure 7 according to Figure 1 (c).

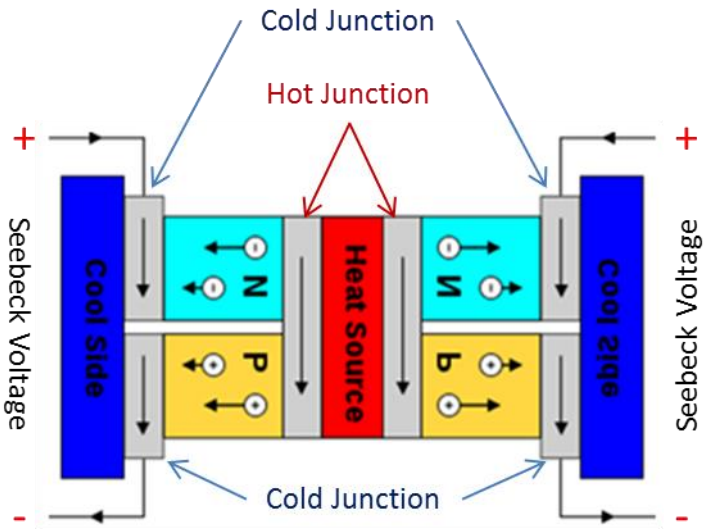

Figure 10: Diagram of Seebeck effect of thermopile

Figure 9, single polysilicon strip heater is used at centre with two thermocouples placed symmetrically, hot junctions are the junctions with a higher temperature and are closer to the heater. N-doped and P-doped are separately used to connect the hot and cold junctions, and two symmetrical Seebeck voltages can be measured in Figure 10 instead of using load resistor in Figure 9, Seebeck voltage can be written as

$$\Delta V = -S_{total} \cdot \Delta T = -[S_N - S_P] \cdot [T_{HJ} - T_{CJ}] \tag{3.8}$$

Where ΔV is the Seebeck voltage in Figure 10, S_N is the N-doped Semiconductor Seebeck coefficient and S_P is the P-doped Semiconductor Seebeck coefficient; and ΔT is the temperature difference between the temperature of hot junction (T_{HJ}) and the temperature of cold junction (T_{CJ}).

In conclusion, thermo-resistive and thermopile are separately used based on different techniques, the essential difference is that thermos-resistive measures the absolute temperatures while thermopile measures the temperature difference directly. Besides, thermos-resistive with 3ω technique requires more complex read-out circuit which will be discussed in the following chapter, and thermos-resistive might be influenced by the ambient temperature since it measures the absolute temperature. However, the structure of thermopile is more complicated and the fabrication process is more complicated since it calls for different doping for N-doped and P-doped of the thermocouple as shown in Figure 10 and also multi-layer which will be discussed in section 3.5.

3.4 Doping

In the previous section, different structures of thermos-resistive and thermopile have been introduced. Both the heater and sensors can be made of doped silicon or polysilicon. The doping level would determine the resistivity (ρ), temperature coefficient of resistance (TCR) and Seebeck coefficient (S_N, S_P).

As indicated in Equation 3.7, the resistance of a polysilicon strip at any temperature can be determined by TCR (α). Variation of the TCR with doping for N-doped polysilicon is shown in Figure 11.

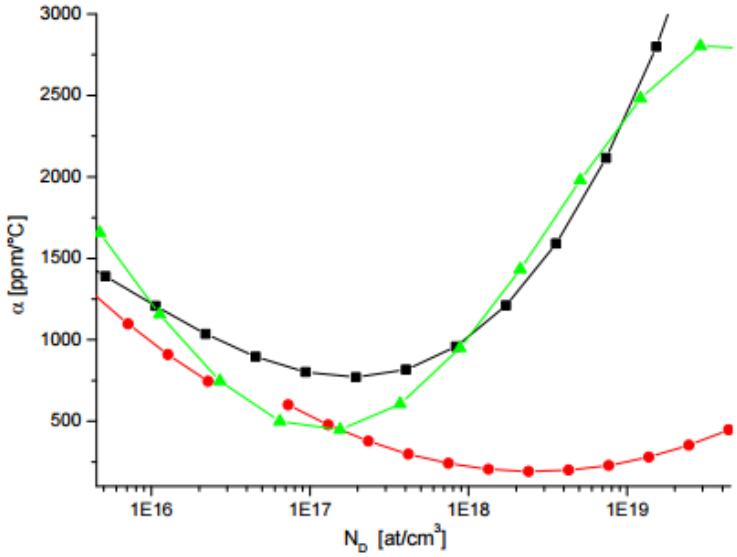

Figure 11: Variations of the thermal coefficient α as a function of doping concentration N_D. Green curves (Klaassen): α_min=449 ppm/℃ ; Black curve (Arora): α_min=770 ppm/℃ ; Red curve: α_min=190 ppm/℃. [19]

As shown in Figure 11, the TCR of N-doped reaches to bottom at around $1.5 \times 10^{17}\ at/cm^3$ for the green curve since it fits roughly for the red and the black curves as well.

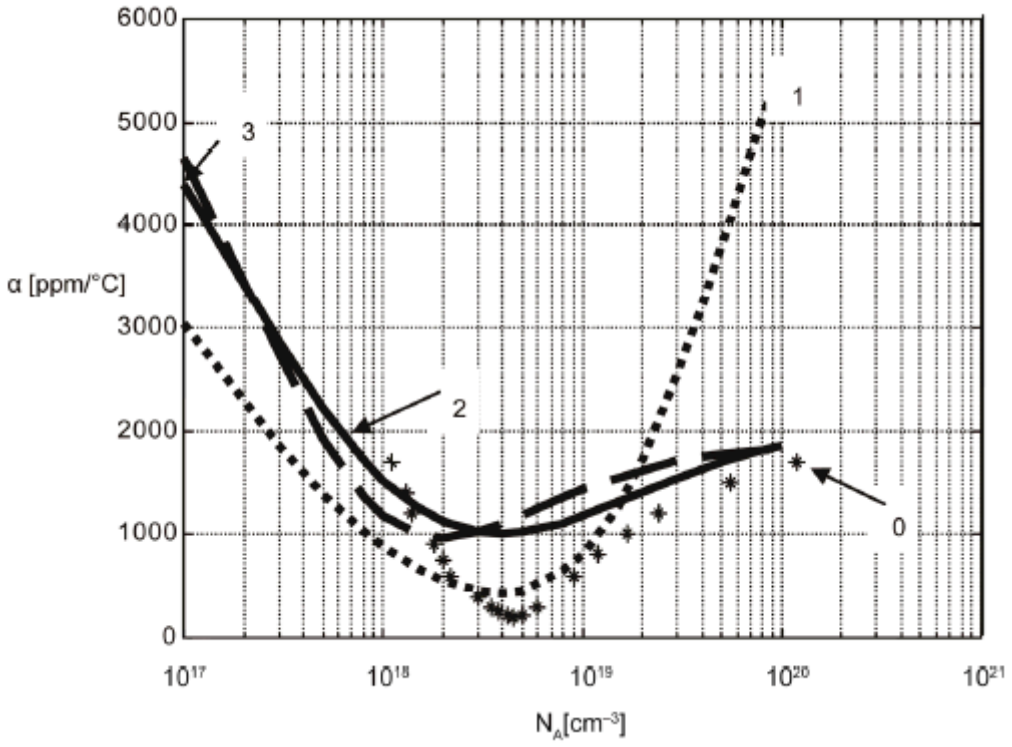

Figure 12: Variations of the thermal coefficient α as a function of doping concentration N_A [20]. 0: Bullis α_min=200 ppm/℃ ; 1: Dorckel α_min=400 ppm/℃ ; 2: Arora α_min=980 ppm/℃ ; 3: Klaassen α_min=1000 ppm/℃ [19]

As shown in Figure 12, the TCR of P-doped has a similar curve as the N-doped, and it reaches a minimum at around $4 \times 10^{18}\ at/cm^3$ for Klaassen's curve.

The doping level of the polysilicon has to be chosen such that a high TCR is achieved for the thermo-resistor structures. Therefore, a doping level far from the minimum of the curves shown in Figures 3.8 and 3.9 must be chosen. This choice directly affects the resistivity of the polysilicon strip. Figure 16 shows the resistivity of n- and p-type silicon for different doping level.

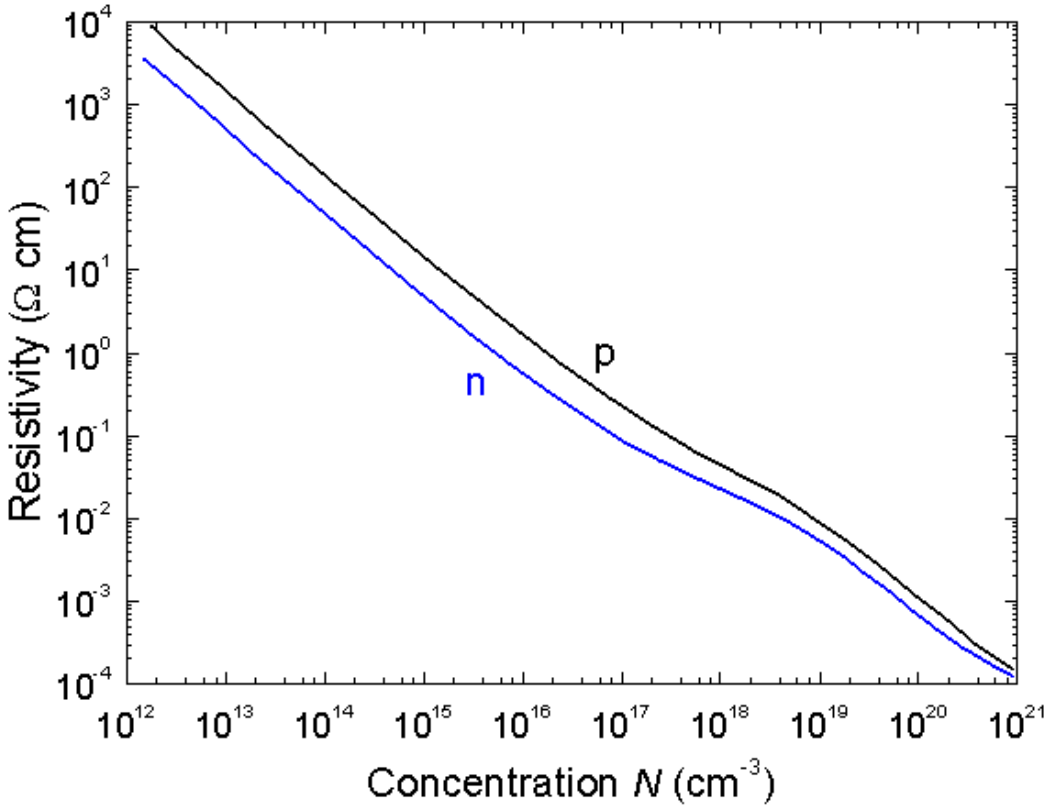

Figure 13: Resistivity versus impurity concentration for Si at 300K [21]

The resistance of a strip with length L and cross section area of A is calculated using Equation 3.9.

$$R = \rho \frac{L}{A} \tag{3.9}$$

Since the choice of resistivity (ρ) is enforced by the TCR, the appropriate resistance can be obtained by selecting the L and A. Therefore, the choice of TCR indirectly affect the dimensions of the thermo-resistors.

Similar to the TCR, the Seebeck coefficient also depends on the doping level. Figures 3.11 and 3.12 show the variations of the Seebeck coefficient by doping in p- and n-type silicon.

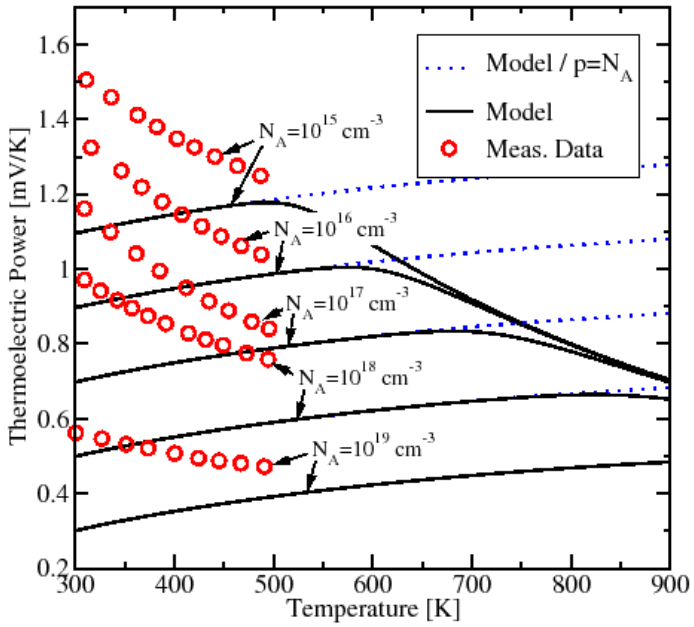

Figure 14: Seebeck coefficients for differently doped p-type silicon samples. Solid lines depict the theoretical models, whereby the decrease at the elevated temperatures results from the increased hole concentration in the intrinsic range.

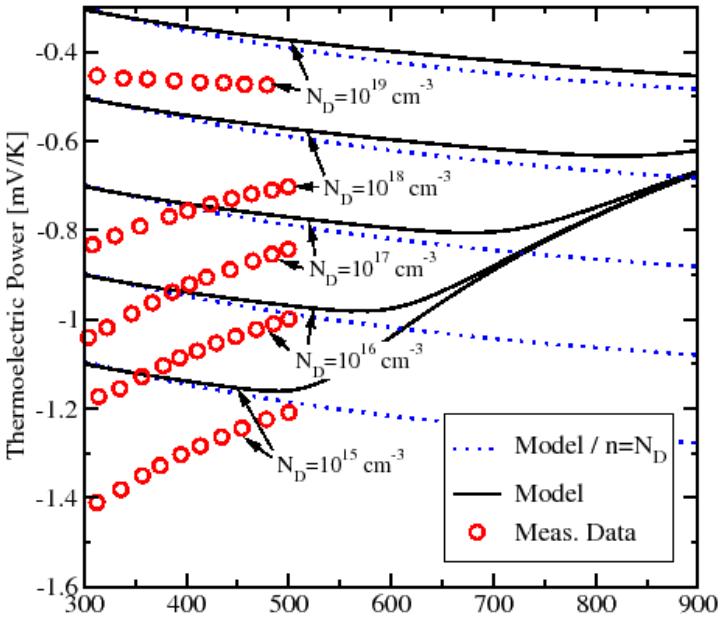

Figure 15: Seebeck coefficient for differently doped n-type silicon samples.

According to the figures, a lower the doping level results in a higher absolute value of the Seebeck coefficient in both p- and n- type silicon. According to Equation 3.8, the higher the absolute values of Seebeck coefficient are, the higher Seebeck voltage creates.

Resistivity and Seebeck coefficient need be taken into consideration since resistivity determines the thermal noise of the signal and Seebeck coefficient determines the voltage

signal, and lower doping gives higher voltage signal and higher thermal noise. So doping needs to be tuned to find the best SNR as

$$SNR = 20\log_{10}\left(\frac{A_{signal}}{A_{noise}}\right) = 20\log_{10}\{\frac{[S_P - S_N]\cdot[T_{HJ} - T_{CJ}]}{\sqrt{4kTR\Delta f}}\} \quad (3.10)$$

Where k is Boltzmann's constant in joules per kelvin, T is the resistor's absolute temperature in kelvins, R is the resistor value in ohms, and Δf is the bandwidth in hertz over which the noise is measured.

Then compromising doping level for n-type and p-type are determined to obtain a resistivity equal to $0.05\ \Omega\cdot\text{cm}$, so $10^{18}\ at/cm^3$ for p-doped and $2.4\times10^{17}\ at/cm^3$ for n-doped are decided for thermopile.

Here for the sake of the simplicity of the fabrication process the same resistivity is also used for both thermopiles and thermo-resistors.

3.5 Heat flux efficiency

Heat that generated at heater could be regarded as current J_h, and this $J_h$partly goes into the liquid mixture as well as partly goes into the substrate. However, most heats that generated at heater are wasted in substrate because the thermal conductivity of substrate is much larger than the thermal conductivity of liquids. Hence many steps need to be taken to lead the heat goes into the liquids instead of substrate. From the perspective of electrical domain as indicated in Figure 6, most current that generates at heater goes into substrate, but we need more current goes into the liquid branch which means that the resistance of substrate should be increased relatively compared to the resistance of liquids, i.e. increase the heat flux efficiency of the structure.

A TCD structure with a length of 1000 µm, width of 10 µm and height of 1 µm for the polysilicon heater and sensor was used for the simulation. Here a piece of silicon with a width of 2000 µm and height of 500 µm is used as the substrate. Finally, a droplet of liquid with a radius of 300 µm is assumed to cover the TCD.

For the sake of simplicity and reducing the needed computation time and resources, the liquid flow was ignored in the finite element simulations. Several customized mesh was constructed (see Figures 3.13 and 3.14) and used for the simulations.

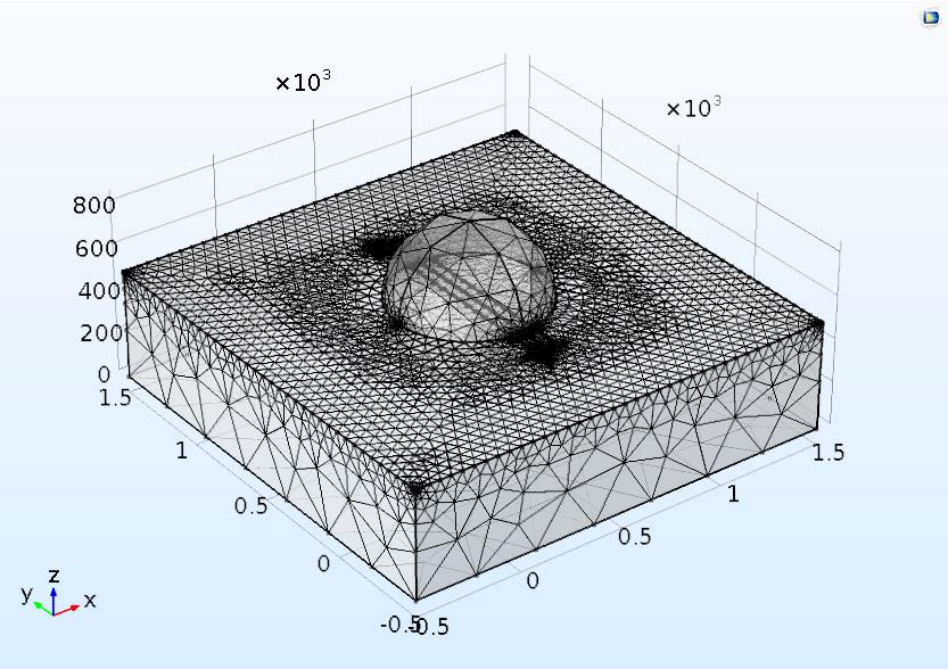

Figure 16: A coarse mesh.

Note that although the mesh is quite coarse over the liquid and substrate, the mesh size in the sensors and heater is sufficiently small and acceptable.

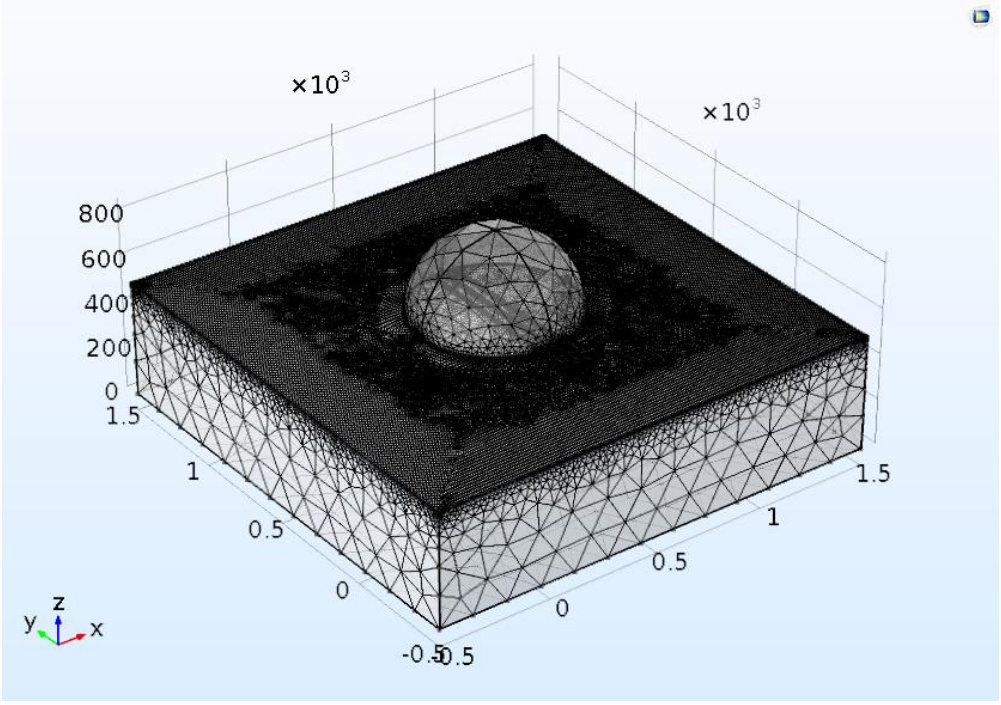

Figure 17: A finer mesh.

The basic theory of finite element analysis is to cut a 3D/2D structure into small pieces (elements), smaller the element, the more accurate simulation is but also requires more computational power. However, a very fine element size is usually unnecessary depending on the model. The element size is hence changes for different domains, i.e. smaller when a dimension of the domain is small. Automated mesh generation using COMSOL multiphysics considers this criteria (see Figure 16). This model consists of only about 29K elements for the coarse mesh but 1873 K elements for a fine mesh. A more optimal mesh can be obtained by manually controlling the mesh type and size for each domain resulting in a model with an accuracy similar to the fine mesh but with a considerable lower element number.

Mesh of "Fine" was used for the simulation because a coarse mesh causes inaccurate simulation result while too intensive mesh would lead to an unnecessarily long computation time.

3.5.1 Optimization analysis of the heat flux efficiency

Sequential steps are taken to improve the heat flux efficiency. First of all, utilizing a thin layer to thermally isolate the TCD structure from the silicon substrate was studied. The relatively low thermal conductivity of silicon-oxide (1.4 W/mK)compared to silicon (34 W/mK) makes it an suitable choice (Figure 18). A thin-film of SiO2 was added to the model and the heat flux for different thicknesses of oxide layer was simulated. The resulting total heat flux along the height of the device is shown in Figure 19.

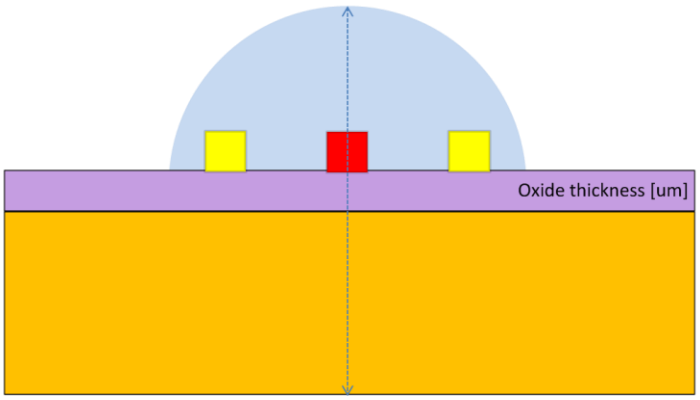

Figure 18: Schematic of cross-section of structure with silicon oxide layer

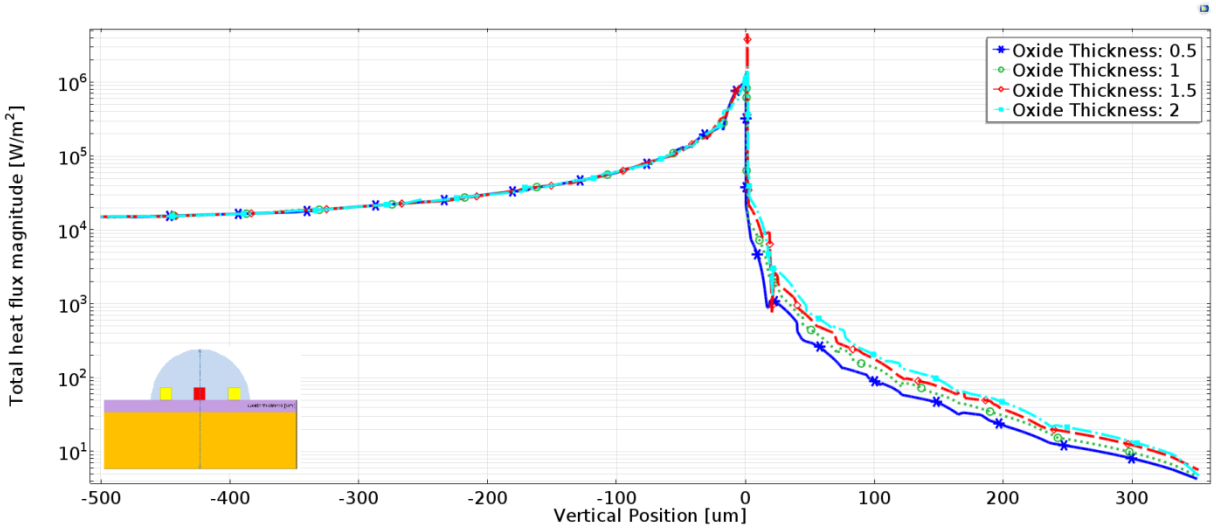

Figure 19: The effect of the silicon oxide thickness on the distribution of total heat flux magnitude

As shown in Figure 19, x-axis indicates the vertical position of the measurement, as shown at the bottom left corner insert, which is a cross-section of the structure, with a blue dashed line that shows the measurement. The negative values correspond to the substrate and positive values are in the liquid. Y-axis shows the total heat flux magnitude. The higher the heat flux is, more heat flow though the certain surface. According to the FEA results a thicker oxide layer results in more heat to be directed into the liquid.

The results however show that the total heat flux to the substrate is still several orders of magnitude higher than to the liquid. Therefore, only a small amount of generated heat is used for the detection of the liquid. An alternative is to make use of air as the thermal isolation layer by under-etching the device area. Figure 20 shows a schematic of such a structure.

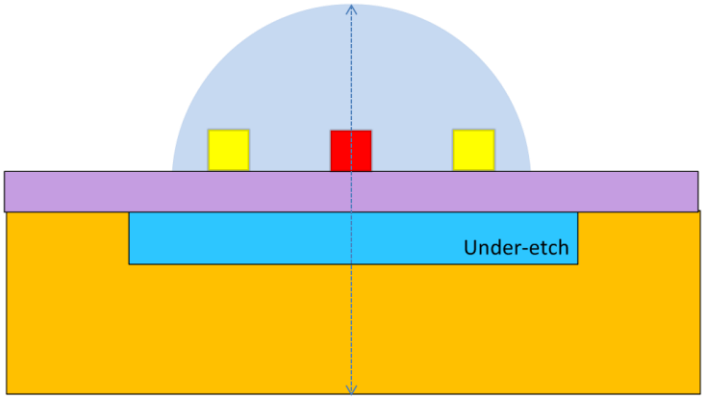

Figure 20: Schematic of cross-section of structure with under-etch

The length of under-etch is 1200 µm and width is 1000 µm, the under-etch layer must be larger than the heater and sensor size to ensure proper isolation between heater and the substrate.

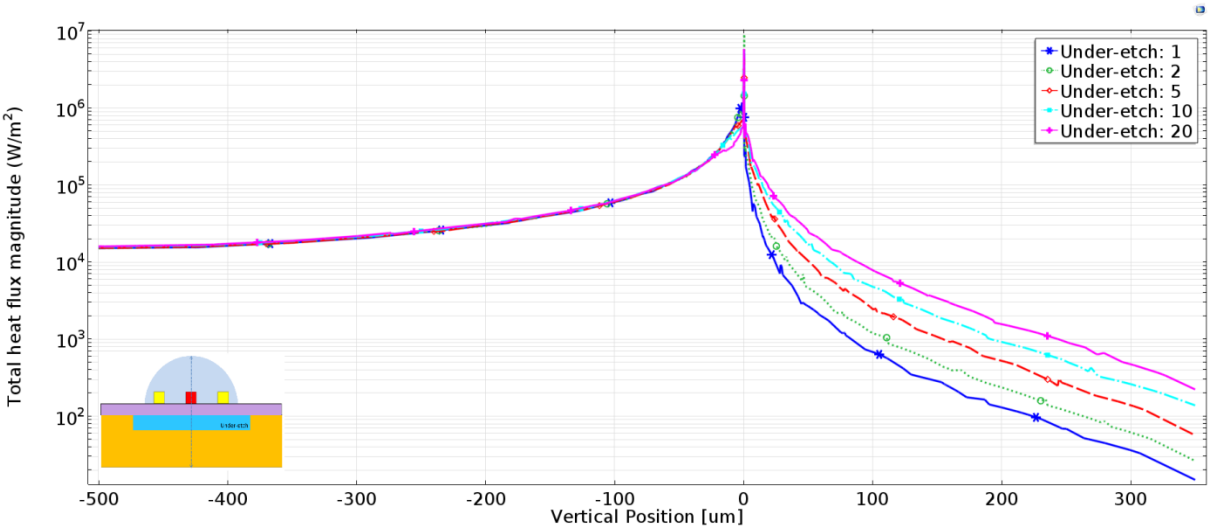

Figure 21: The effect of the under-etch on the distribution of total heat flux magnitude

Figure 21 shows the simulation results for an under-etch filled with air. Vacuum or air has a very low thermal conductivity hence provide the best thermal isolation. According to the results, a 5 µm under-etch layer ensures a high heat flux to the liquid. This is also quite within the feasible range of surface micromachining processes.

At this under-etching gap more than 10% of the heat is directed to the liquid and used for the sensing.

In this case the equivalent, circuit in Figure 6 should be changed into Figure 22.

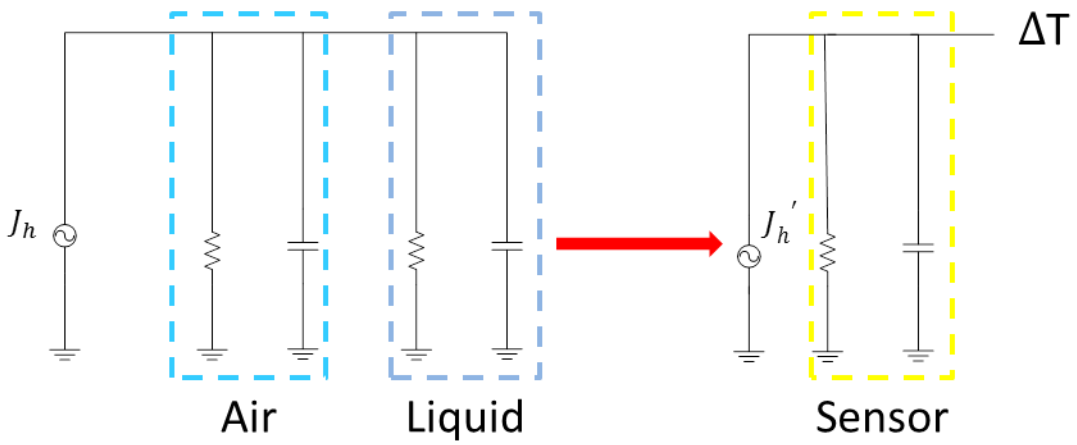

Figure 22: Thermal equivalent circuit with under-etch filled with air

Compared with Figure 6, substrate is replaced by air in under-etch, and if we take 5 μm as the height of under-etch, the resistance and capacitance of under-etch can be easily calculated to 160.25 Ω and $7.386 \times 10^{-12} F$. So Table 3.2 can be extended to Table 3.3.

Table 3.3: Thermal Properties and Electrical Properties at room temperature (with under-etch).

Liquid and Solid	Thermal Cond. [W/(mK)]	Specific Heat Capacity [kJ/(kgK)]	Electrical Resistance [K/W]	Electrical Capacitance [J/K]
Ethanol	0.179	2.443	2540.38	1.730×10^{-4}
Gasoline	0.15	2.22	3031.52	1.433×10^{-4}
Water	0.58	4.182	784.01	3.755×10^{-4}
E85	0.175	2.41	2598.44	1.685×10^{-4}
$Air_{underetch}$	0.026	1.005	160.25	7.386×10^{-12}
Silicon	130	0.7	0.9615	3.26×10^{-6}
Polysilicon	34	0.678	***	***

Figure 23 shows the frequency response of the under-etched device.

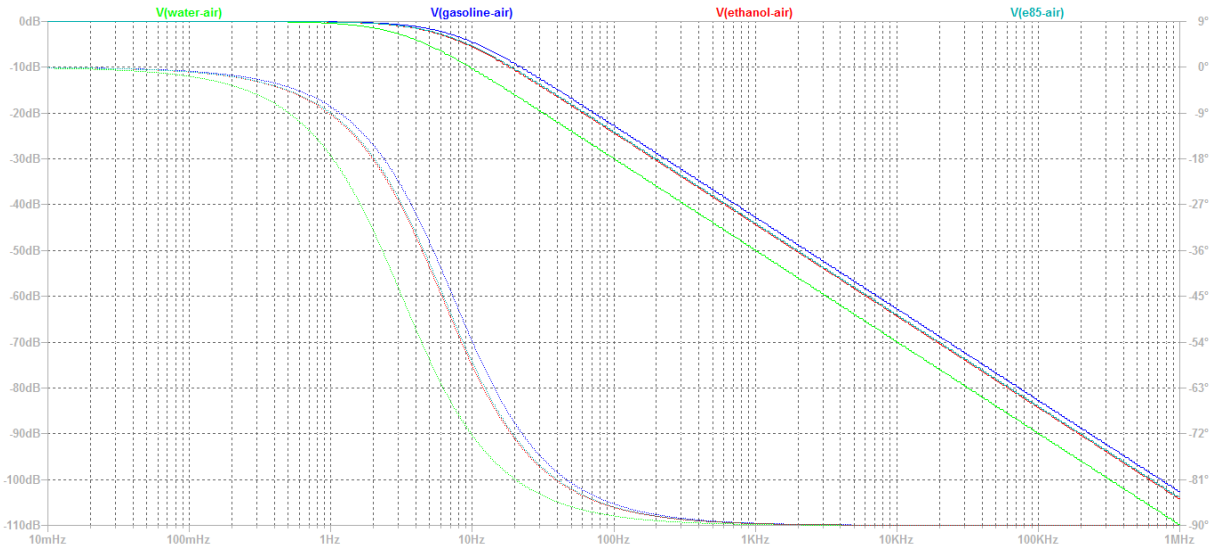

Figure 23: Frequency responses of thermal equivalent circuit with different liquids (with under-etch)

In Figure 23, the bandwidths of each liquids are clearly shorter than that of in Figure 5 because the low resistance of substrate is replaced by a relatively high resistance of air in

under-etch, and more current that generates at heater is led to the liquid branch which increases the sensitivity of liquids to the change of compositions.

Finally, silicon oxide layer is etched away for under-etch, then silicon nitride should be used as the membrane layer due to its high Young's modulus and stiffness and also a tensile stress, which makes it mechanically a good candidate for the membrane layer. Besides, silicon nitride has a relatively low thermal conductivity compared to the silicon substrate.

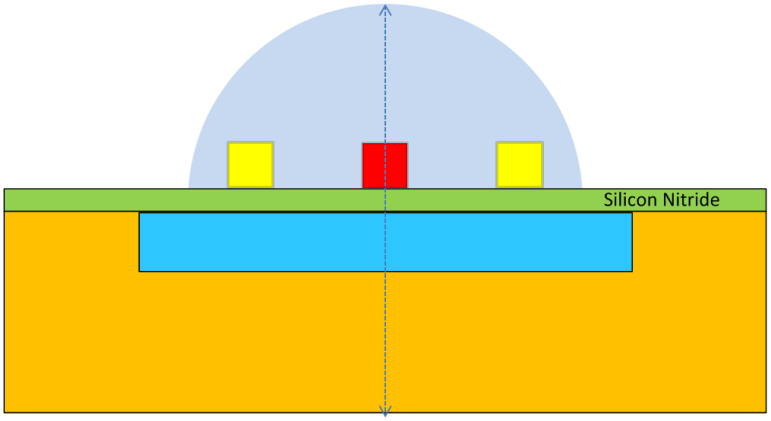

Figure 24: Schematic of cross-section of structure with Silicon Nitride membrane

Schematic is shown in Figure 24. Different thickness of silicon nitride is then simulated to check the heat flux vertically in Figure 25. The high thermal isolation hence increases the sensitivity of the TCD to the change of mixture composition.

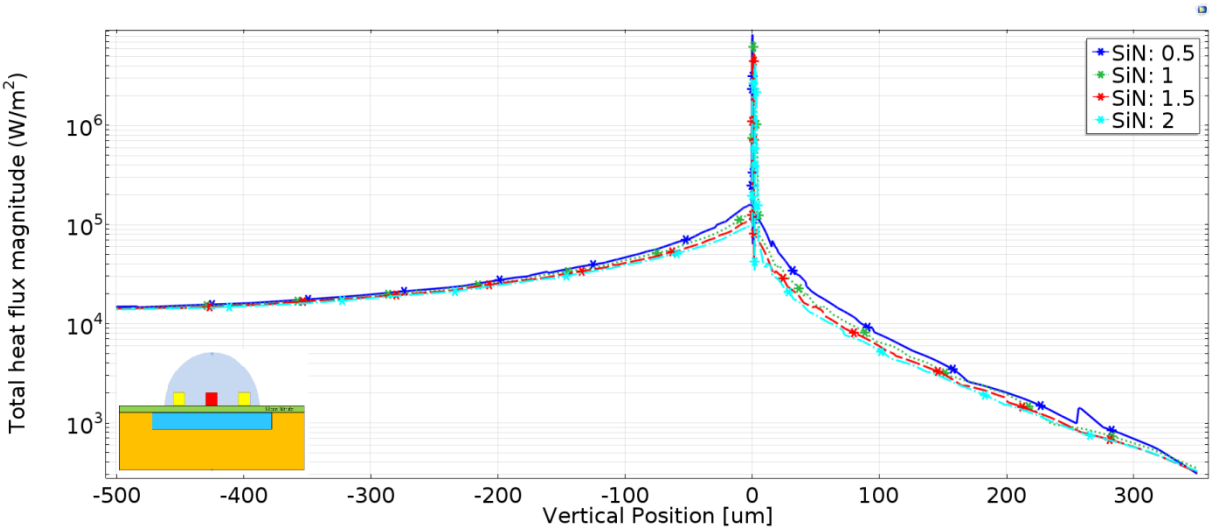

Figure 25: The effect of the silicon nitride on the distribution of total heat flux magnitude

Figure 3.22 shows that the thicker the silicon nitride is, the less heat would be transferred into liquids and substrate. This is because the air cavity under the membrane already provide a

sufficient thermal isolation and it is not affected by the thickness of the nitride layer. On the other hand a thick nitride layer results in an in-plane heat transfer through the nitride layer. Therefore, a thinner layer of nitride is more favourable.

In conclusion, several steps were taken to improve the heat efficiency vertically. Under-etch is the best way to boost the heat flux efficiency while reducing the bandwidth of system at the same time.

3.5.2 Horizontal Analysis

In Section 3.5.1, several steps are taken to improve the heat efficiency in vertical directions, such as adding membrane and under-etch. However, heat flux in horizontal direction also needs to be considered.

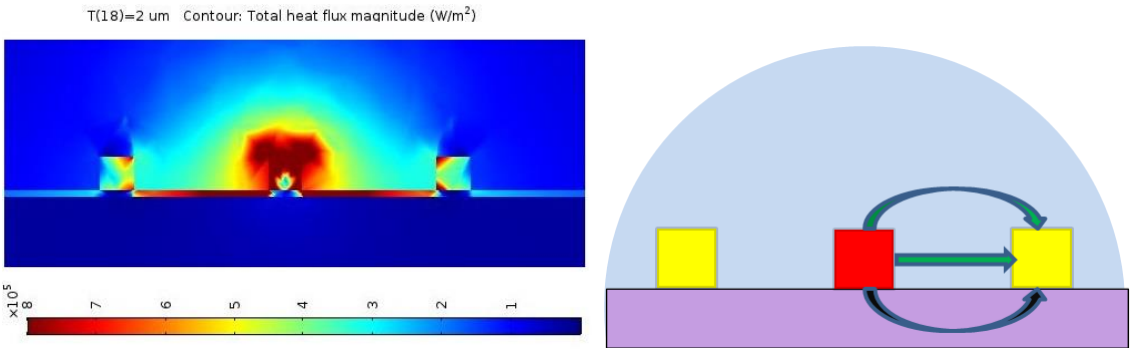

Figure 26: (a) Total heat flux magnitude; (b) schematic diagram

The heat flux magnitude profile in a cross-section area of the TCD is shown in Figure 26. According to the figure, a large amount of heat is transferred via the silicon nitride membrane. The heat transfer to the wafer is however due to the low conductivity of airgap is marginal. This step aims to increase the heat transfer through the liquid as shown by the green arrows in Figure 26. Slits were cut through the membrane as a measure to reduce the heat transfer via the membrane (Figure 27). The resulting heat flux magnitude for different slit sizes are shown in Figure 28.a and b.

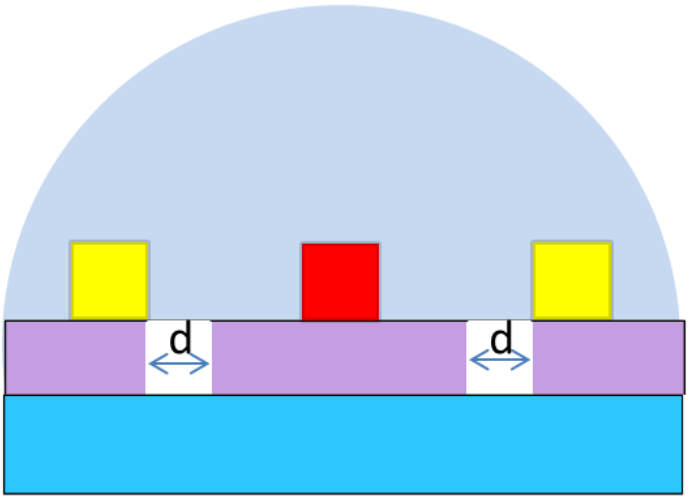

Figure 27: Schematic diagram with Slits in membrane

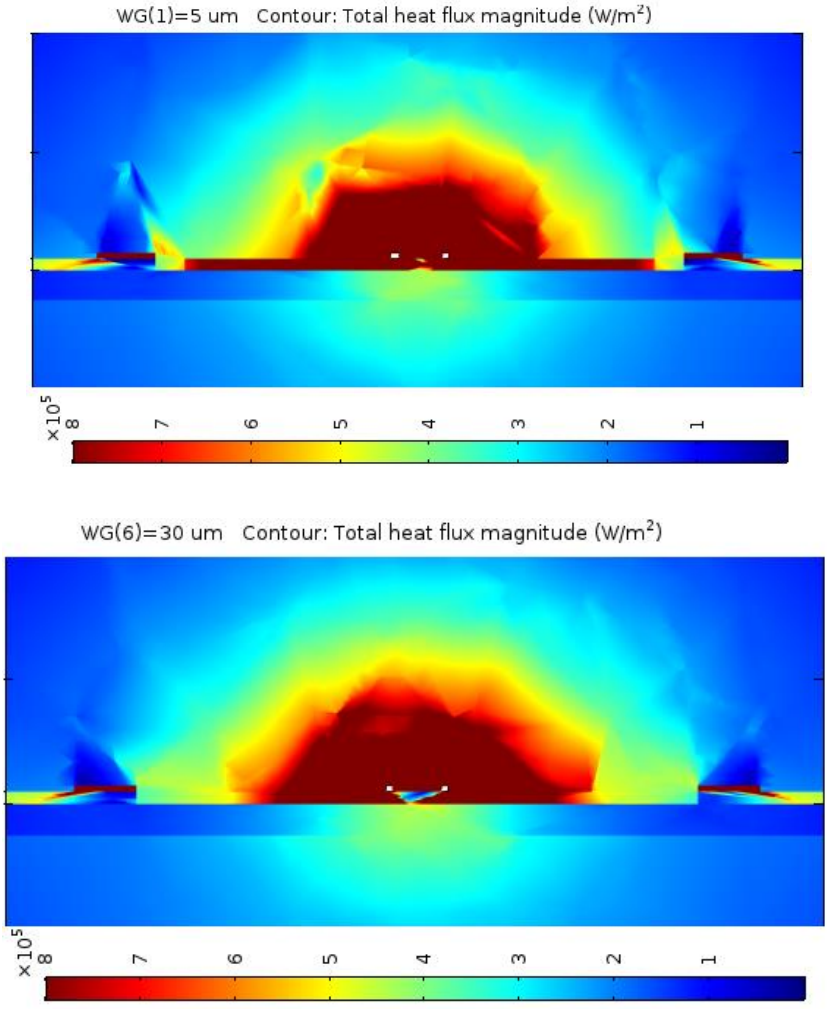

Figure 28: (a) Cross section of heat flux with 5 µm slits (Water-Air) (b) Cross section of heat flux with 30 µm slits (Water-Air)

Silts are used to cut the heat transfer line through the membrane and were found to be more effective when applied near to the sensors.

In Figure 28 (b), 30 µm slits are used between membrane and sensors. In this case, large gap nicely isolates the connection between membrane and sensors, which eliminates the influence of membrane in terms of heat transfer and heat that receive at sensor comes from nowhere but liquids surrounding. However, the 5 um slit size was not found to be as effective.

However, large gap mainly has two drawbacks. Firstly, a large gap may cause membrane break due to the mechanical stress. Secondly, slits would result in the liquid to penetrate under the membrane and fill the under-etching. The schematic of such a structure is shown in Figure 29.

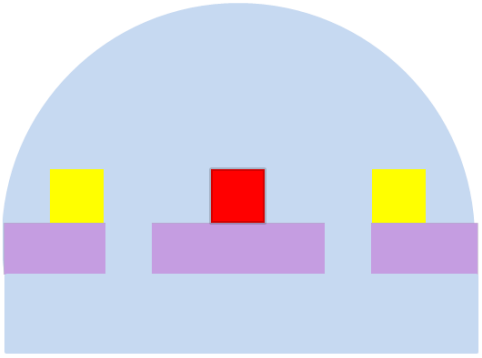

Figure 29: Schematic diagram with slits

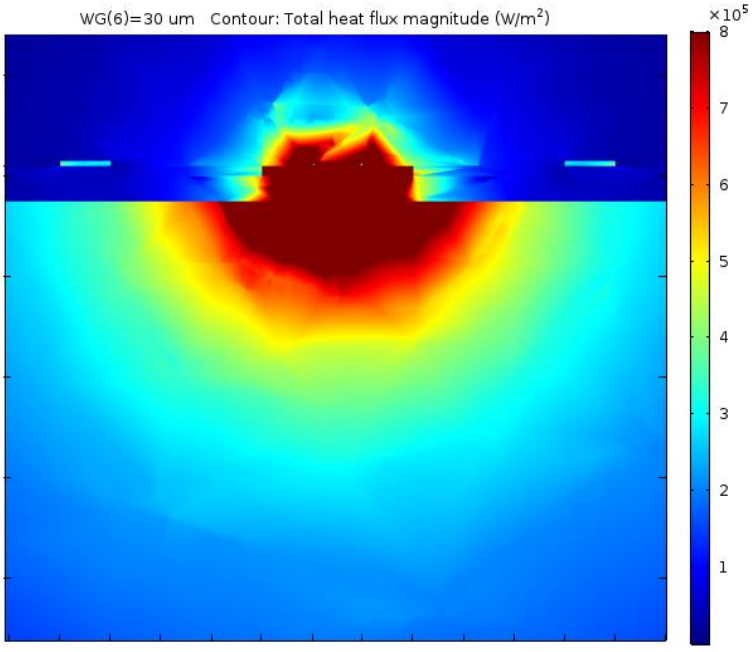

Figure 30: Cross section of heat flux with 30 µm slits (Water-Water)

In Figure 30, heat flux magnitude in the cross section is shown. A large amount of heat flux is transmitted to the liquid in the under-etching. This heat flux also contributes to the sensor

signal. However, a large amount of heat is still transferred to the wafer due to the small height of the under-etching.

Apart from the thickness of silicon oxide and silicon nitride membrane, and under-etch height, there are also few parameters that influence the performance of structures.

First critical design property is the lateral spacing heater and symmetric sensors. Simulation results are shown in Figure 31. As sensor operation is based on the measurement of temperature difference, the lateral spacing should be large enough to cover the area. However, Figure 31 indicates that a lateral spacing larger than 100 µm in the thermocouple (or position of the second polysilicon strip) would not be useful.

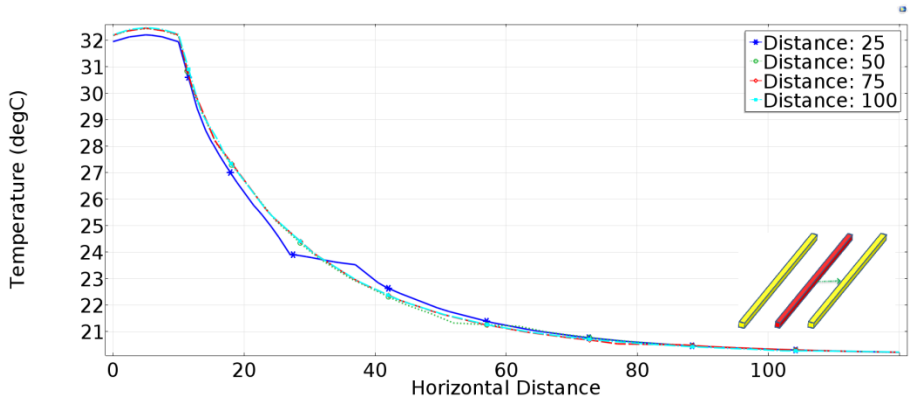

Figure 31: Lateral temperature distribution of the structure shown in the insert in case the under-etch is filled with air biofuel is pure ethanol.

The spacing between heater and sensors is not only important in thermos-resistance structure, but also in thermopile structure.

In conclusion, slits may resolve the problem of membrane-heating-up-sensor, but the problem of slits are fragile of structure, extra fabrication process, and more heat wasted in the substrate. Finally, spacing between heater and sensor is well-defined to find the most compromising value.

3.6 Thermopile Design Process

A thermocouple structure is shown Figure 32.

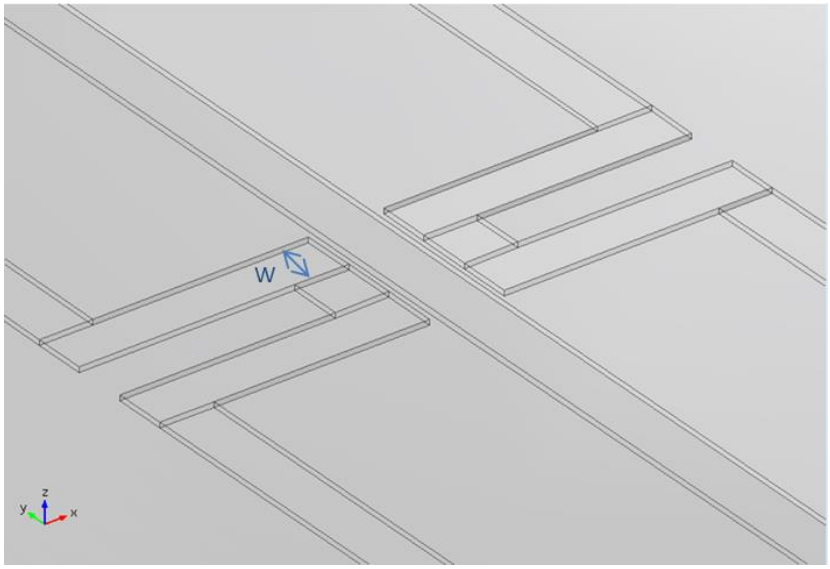

Figure 32: Initial thermopile structure

As discussed in section 3.3, a temperature difference between the high and cold junctions creates a Seebeck voltage proportional to the temperature difference between hot junction and cold junction due to Seebeck effect.

To increase the Seebeck voltage, the temperature of the cold junction must be decreased by optimizing the thermocouple structure. This can be achieved by optimization of the length of the thermopiles.

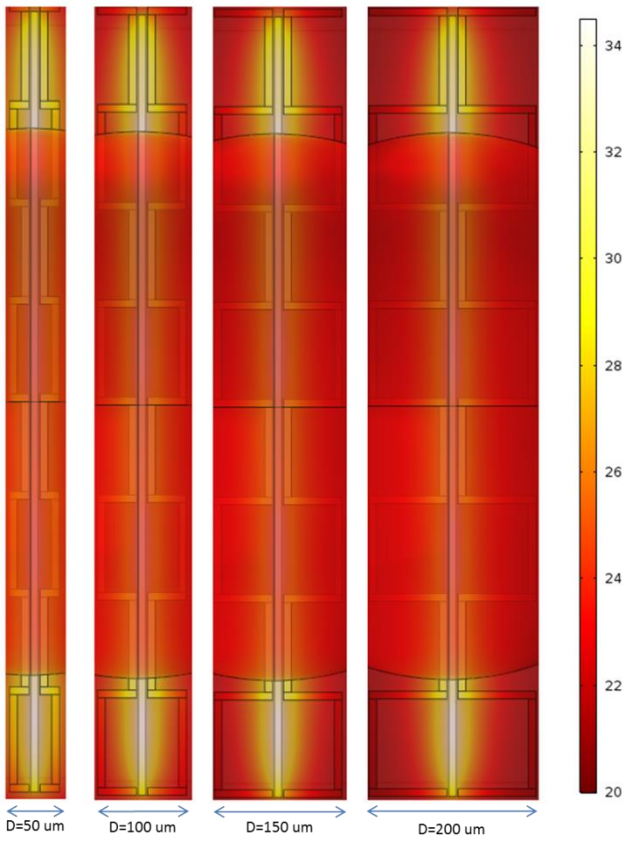

Figure 33: Top view of thermopile temperature with different spacing

Figure 33 shows that when cold junctions are placed too close to the hot junction, such as 3.25 µm at the most left side, the temperature difference would be too small, hence Seebeck voltage would be too small to measure. On the contrary, temperature difference would no longer increase when cold junctions are placed too far away from the hot junction, such as 100 µm.

This is similar to the thermo-resistor case. The difference between thermo-resistor and thermopiles however is the increase in electrical resistance with a longer thermopile legs. This increase the Johnson-Nyquist noise (i.e. thermal noise).

A compromise needs to be made for spacing since larger spacing gives higher thermal noise but also higher Seebeck voltage (signal). Therefore, signal noise ratio (SNR) needs to be calculated to find the optimized spacing.

Apart from decreasing the temperature of cold junction, the temperature of hot junction could be increased to the temperature of heater as close as possible.

First design to increase the temperature of hot junction is to place hot junction on top of the heater, which is shown in Figure 34. This configuration results in a temperature of hot junction closer to the heater temperature.

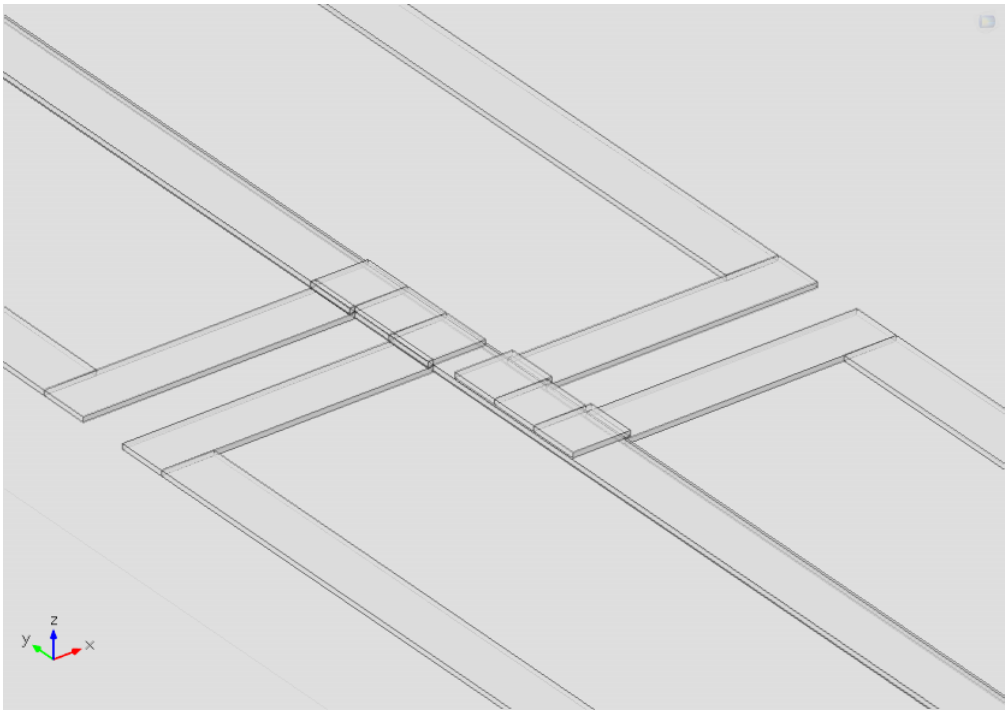

Figure 34: Hot junction on top of heater

However , this configuration requires an extra mask for photo-lithography for fabrication, so this method is avoided in order to decrease the complication of fabrication. An alternative configuration can be obtained by placing metal (aluminium) pad on top of hot junction while hot junction is still close to heater, as is shown in Figure 35.

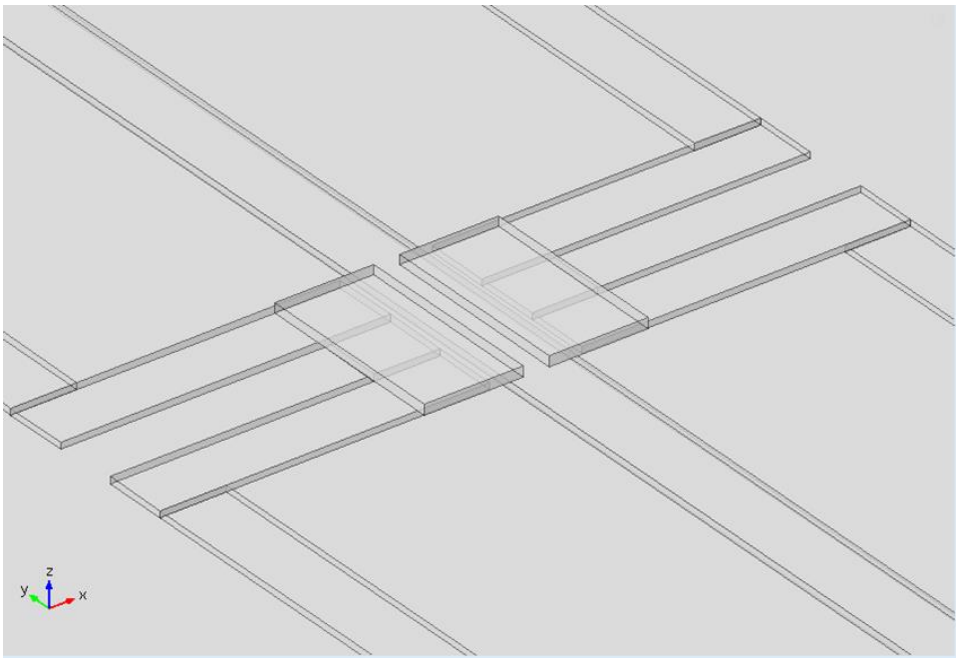

Figure 35: Metal on Top of hot junction

In Figure 35, metal is placed on top of hot junction and parts of hot junction, to act as the thermal shorted material and contact the temperature between hot junction and heater. However, the result turns out to be not as good as we assumed because the metal itself is also a good thermal radiant material with large thermal conductivity, which absorbs the heat in hot junction. So instead of being the thermal shorted material that increase the temperature of hot junction, metal pad releases the heat from hot junction and heater.

To prevent this heat leakage, another layer of silicon nitride is added covering the metal pad, shown in Figure 36.

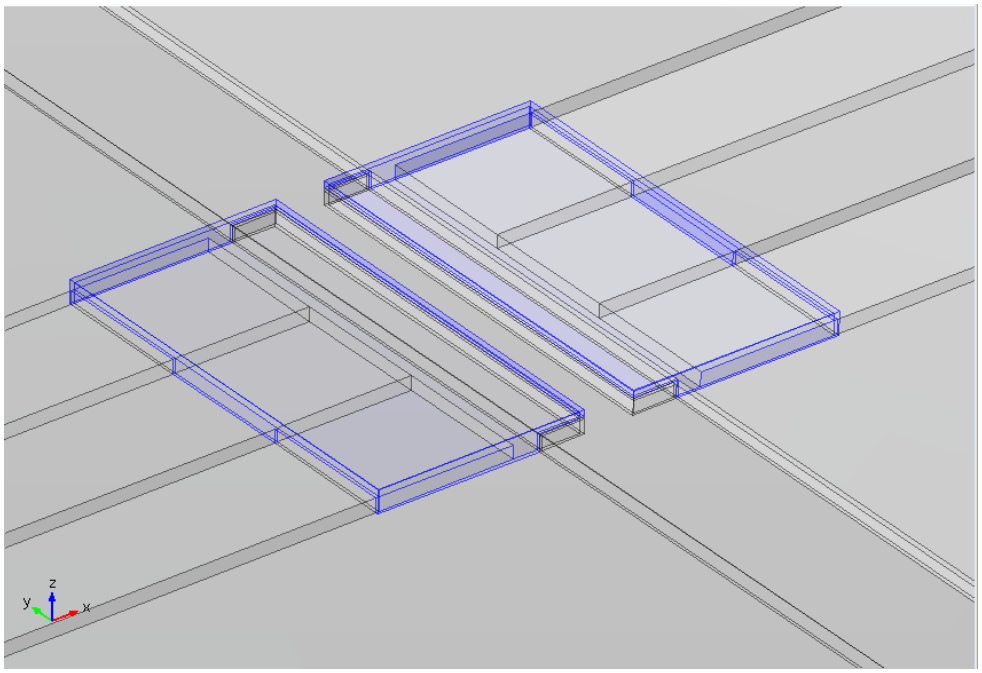

Figure 36: Silicon nitride on top of metal

In Figure 36, the blue boxes are added to prevent heat leakage from metal, and results turned out to be promising, thanks to the low thermal conductivity of silicon nitride, silicon nitride has the property of electrical isolated that could be used to isolate the interaction between electrical conduct metal and liquids.

Finally, the comparison is made between the structures of Figure 16, 3.29, 3.32 and 3.33. Shown in Figure 37.

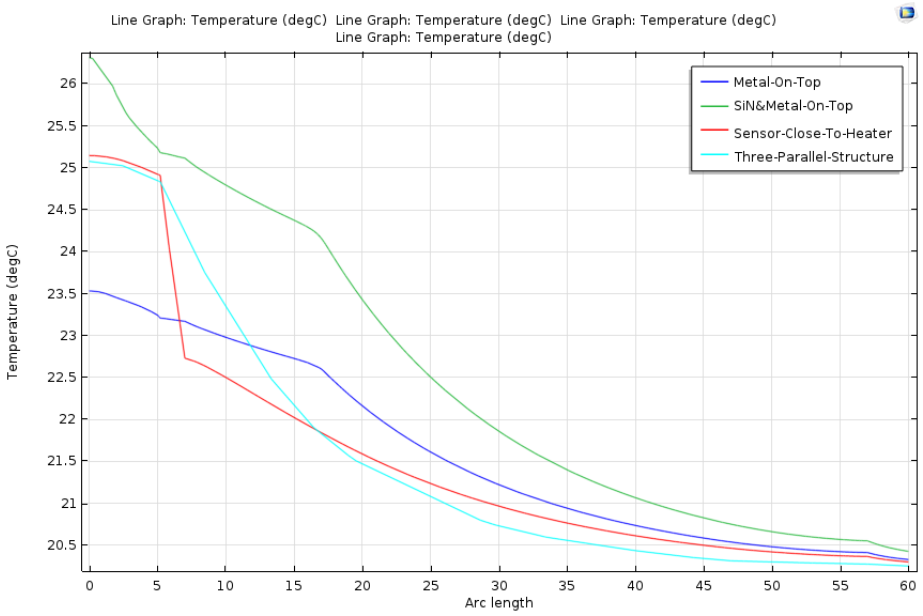

Figure 37: Comparison between different structures

In Figure 37, different structures are compared as x-axis is the spacing with heater, and y-axis is the temperature according to x-axis. The temperature of hot junction is highest when metal and silicon nitride are both placed on top of heater, which is shown in the green curve. Increasing the temperature of hot junction without making too much difference of cold junction is the best achieved in the structure of Figure 36.

Second critical design property is the width of thermopile which also needs to be determined. Width of the polysilicon strips in a thermopile slightly change the temperature of cold junction because more heat would be transfer through the polysilicon lines (instead of liquids) to the cold junction if width is larger. The heat transfers results a smaller causes less temperature difference thus a smaller Seebeck voltage.

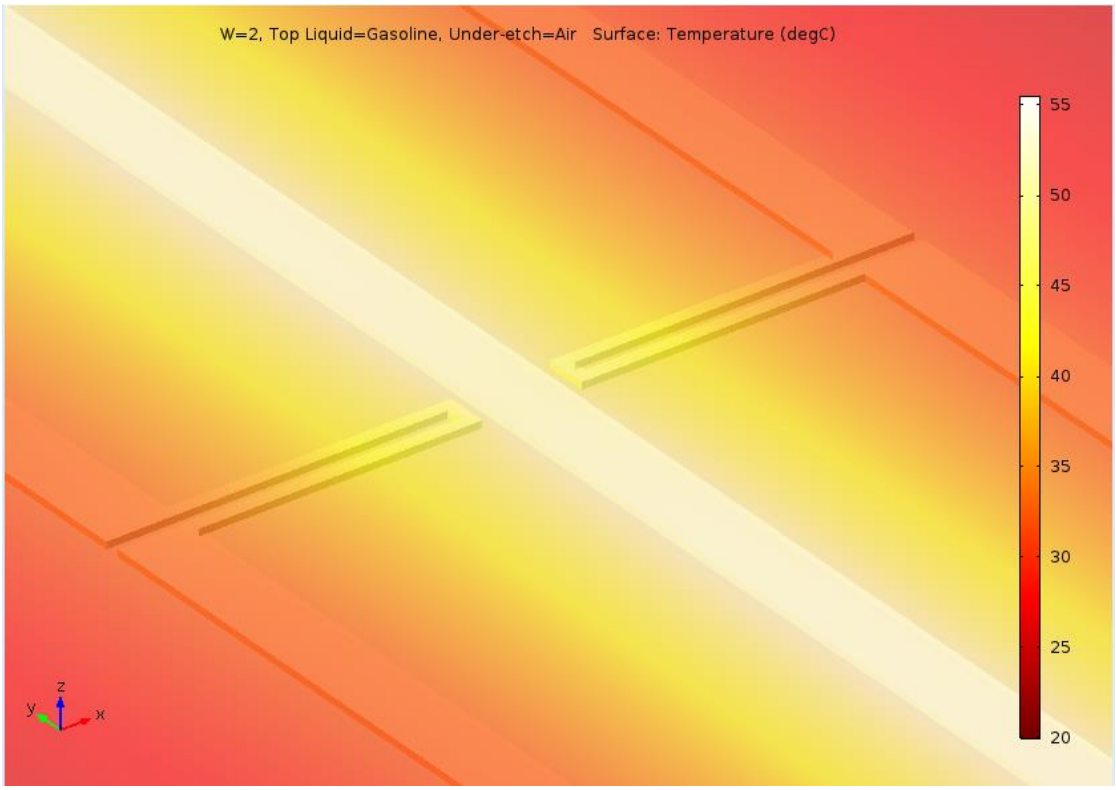

Figure 38: Width of 2 µm with gasoline and air

Figure 39: Width of 10 µm with gasoline and air

In Figure 38 and 39, the temperature profile of two different widths of thermopiles are shown. The width would not influence the temperature of cold junction since cold junction is already placed far away enough from hot junction, and temperature of hot junction decreases with the increment of width of thermopile.

However, larger width leads to less resistance and less thermal noise. The increase of thermopile width leads both to a decrease in the Seebeck voltage and thermal noise, which makes the calculation of SNR more complicated. Just like spacing between hot and cold junction, width also requires compromise and find the optimized values.

Besides, number of thermopile is also a critical design property that needs to be considered. Increase in the number of thermopile leads to multiple times of Seebeck voltage that generates at each thermopile, but higher number of thermocouples increases the total length of sensors and further increase the electrical resistance hence increases the thermal noise.

3.7 Conclusion

In conclusion, the design process and parameters can be summarized in Figure 40.

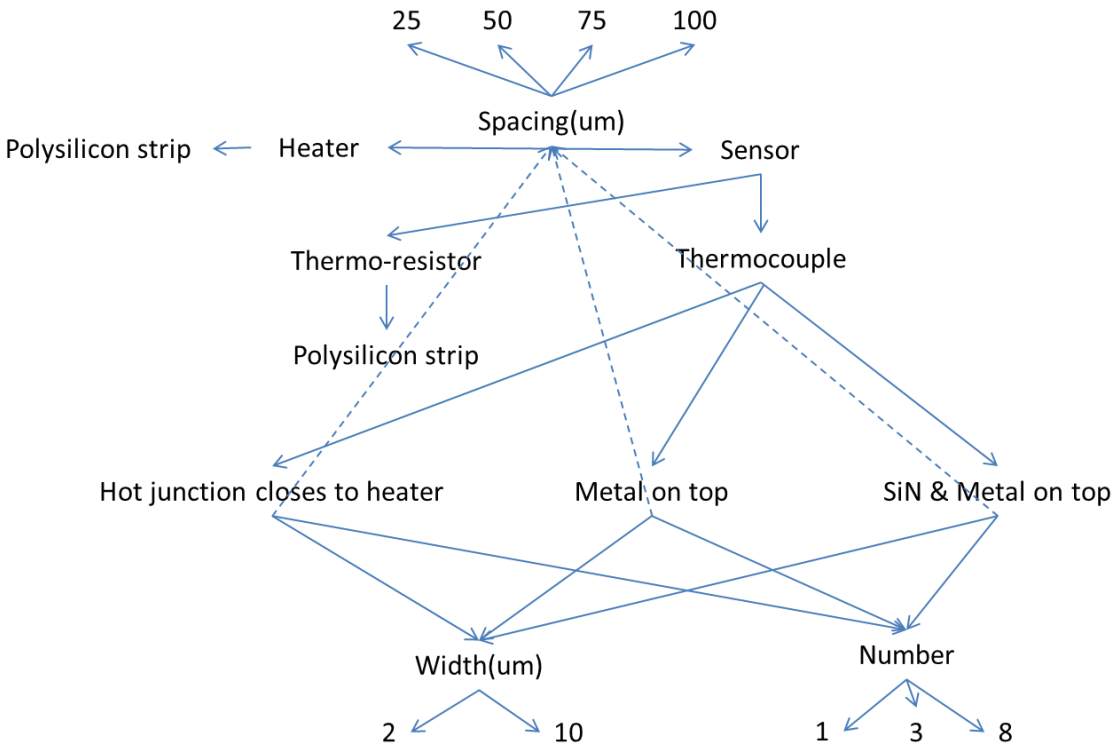

Figure 40: Schematic of Design Process and Design Properties

Material choices discussed in this chapter are shown in the figure. As heater is made of polysilicon strip, sensor is either thermos-resistor or thermocouple, and thermocouple can be further divided into three subsequence classifications as hot junction closes to heater, metal on top, and Silicon nitride on top. Besides, these three different structures could be further extended because of the variation in width of thermocouple, spacing between hot and cold junction, and number of thermopiles.

Reference

[1] Choi S R, Kim J, Kim D. 3 ω method to measure thermal properties of electrically conducting small-volume liquid[J]. Review of scientific instruments, 2007, 78(8): 084902.

[2] Moon I K, Jeong Y H, Kwun S I. The 3ω technique for measuring dynamic specific heat and thermal conductivity of a liquid or solid[J]. Review of scientific instruments, 1996, 67(1): 29-35

[3] Park B K, Park J, Kim D. Note: Three-omega method to measure thermal properties of subnanoliter liquid samples[J]. Review of Scientific Instruments, 2010, 81(6): 066104.

[4] Park B K, Yi N, Park J, et al. Note: Development of a microfabricated sensor to measure thermal conductivity of picoliter scale liquid samples[J]. Review of Scientific Instruments, 2012, 83(10): 106102.

[5] Schiffres S N, Malen J A. Improved 3-omega measurement of thermal conductivity in liquid, gases, and powders using a metal-coated optical fiber[J]. Review of Scientific Instruments, 2011, 82(6): 064903.

[6] Hong J, Kim D. Measuring the thermal conductivity of flowing liquid samples using the three omega method[J]. Journal of Heat Transfer, 2012, 134(9): 094502.

[7] Hong J, Chang Y S, Kim D. Development of a micro liquid-level sensor for harsh environments using a periodic heating technique[J]. Measurement science and technology, 2010, 21(10): 105408.

[8] Hong J, Chang Y S, Kim D. Development of a micro thermal sensor for real-time monitoring of lubricating oil concentration[J]. International journal of refrigeration, 2011, 34(1): 374-382.

[9] Roder H M. A transient hot wire thermal conductivity apparatus for fluids[J]. J. Res. Natl. Bur. Stand, 1981, 86(5): 457-493.

[10] Cahill D G. Thermal conductivity measurement from 30 to 750 K: the 3ω method[J]. Review of scientific instruments, 1990, 61(2): 802-808.

[11] Swartz E T, Pohl R O. Thermal resistance at interfaces[J]. Applied Physics Letters, 1987, 51(26): 2200-2202.

[12] Bruschi P, Dei M, Piotto M. An offset compensation method with low residual drift for integrated thermal flow sensors[J]. IEEE Sensors Journal, 2011, 11(5): 1162-1168.

[13] Bruschi P, Diligenti A, Navarrini D, et al. A double heater integrated gas flow sensor with thermal feedback[J]. Sensors and Actuators A: Physical, 2005, 123: 210-215.

[14] Choi S R, Hong J, Kim D. A micromachined AC thermal sensor for monitoring the liquid–gas interface in a microchannel[J]. Sensors and Actuators A: Physical, 2009, 150(1): 40-45.

[15] http://edadocs.software.keysight.com/pages/viewpage.action?pageId=5688994

[16] Van Herwaarden A W, Sarro P M. Thermal sensors based on the Seebeck effect[J]. Sensors and Actuators, 1986, 10(3-4): 321-346.

[17] Nieveld G D. Thermopiles fabricated using silicon planar technology[J]. Sensors and Actuators, 1982, 3: 179-183.

[18] https://en.wikipedia.org/wiki/Thermoelectric_effect

[19] Kerrour F, Boukabache A, Pons P. Modelling of thermal behavior N-doped silicon resistor[J]. Journal of Sensor Technology, 2012, 2(03): 132.

[20] Boukabache A, Pons P. Doping effects on thermal behaviour of silicon resistor[J]. electronics letters, 2002, 38(7): 342-343.

[21] http://www.ioffe.ru/SVA/NSM/Semicond/Si/electric.html

[22] Wagner M. Simulation of thermoelectric devices[M]. na, 2007.

Chapter 4. Fabrication and Layout

The design and simulation of the TCD structures were discussed in the previous chapters. Several parameters affecting the performance of the sensors were studied using finite element analysis and considering the fabrication constraints. This resulted in several material choices and structural optimizations of the sensors. The fabrication process leading to manufacturing of the detectors is discussed in this chapter.

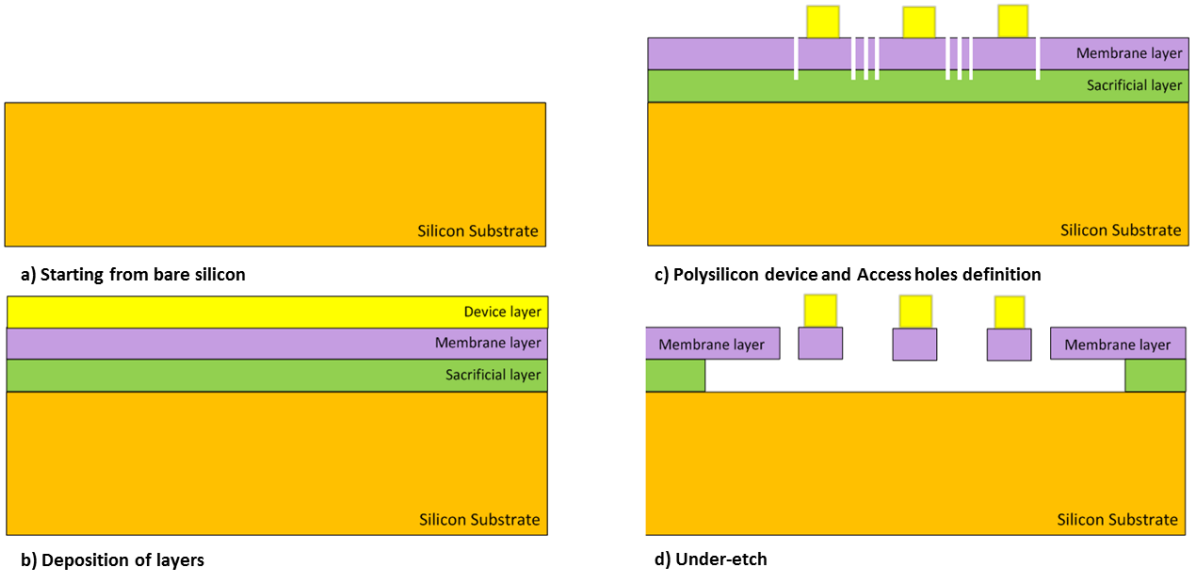

Figure 41: General process of schematic diagrams of fabrication

The main steps in the fabrication process is presented in Figure 4.1. The fabrication starts with bare silicon substrate. Afterwards, different layers with different purposes are deposited. Followed by the polysilicon device and access holes definition. Last step is to etch away the sacrificial layer of silicon oxide, which creates an under-etch layer.

In the following of this chapter, the fabrication process are firstly presented step by step in detail. Secondly, overview of layout design for lithography is introduced to give a large-scale general picture. Afterwards, as discussed in the conclusion of previous chapter, different design parameters such as the number of thermocouples, length of heater and sensors, doping for heater and sensors are discussed. Besides, special design consideration such as pillar array, vertically-used as well as horizontally-used structures and test structures are presented. Finally, some fabrication results and images will be illustrated and the challenges are discussed.

4.1 Fabrication Process

A bulk or surface micromachining process can be used to transfer the ideas MEMS devices. Both processes begin with a bare silicon wafer upon which structure is formed by patterning, etching, and deposition. The main difference between surface and bulk micromachining is that in bulk micromachining the silicon substrate is etched, while in the surface micromachining layers are deposited and etched on top of a silicon wafer.

Surface micromachining can be easily integrated with a CMOS compatible process, hence was selected for the fabrication process. The fabrication was carried out in Else Kooi Lab (formerly known as DIMES) in Delft University of Technology. Figure 42 shows the fabrication steps.

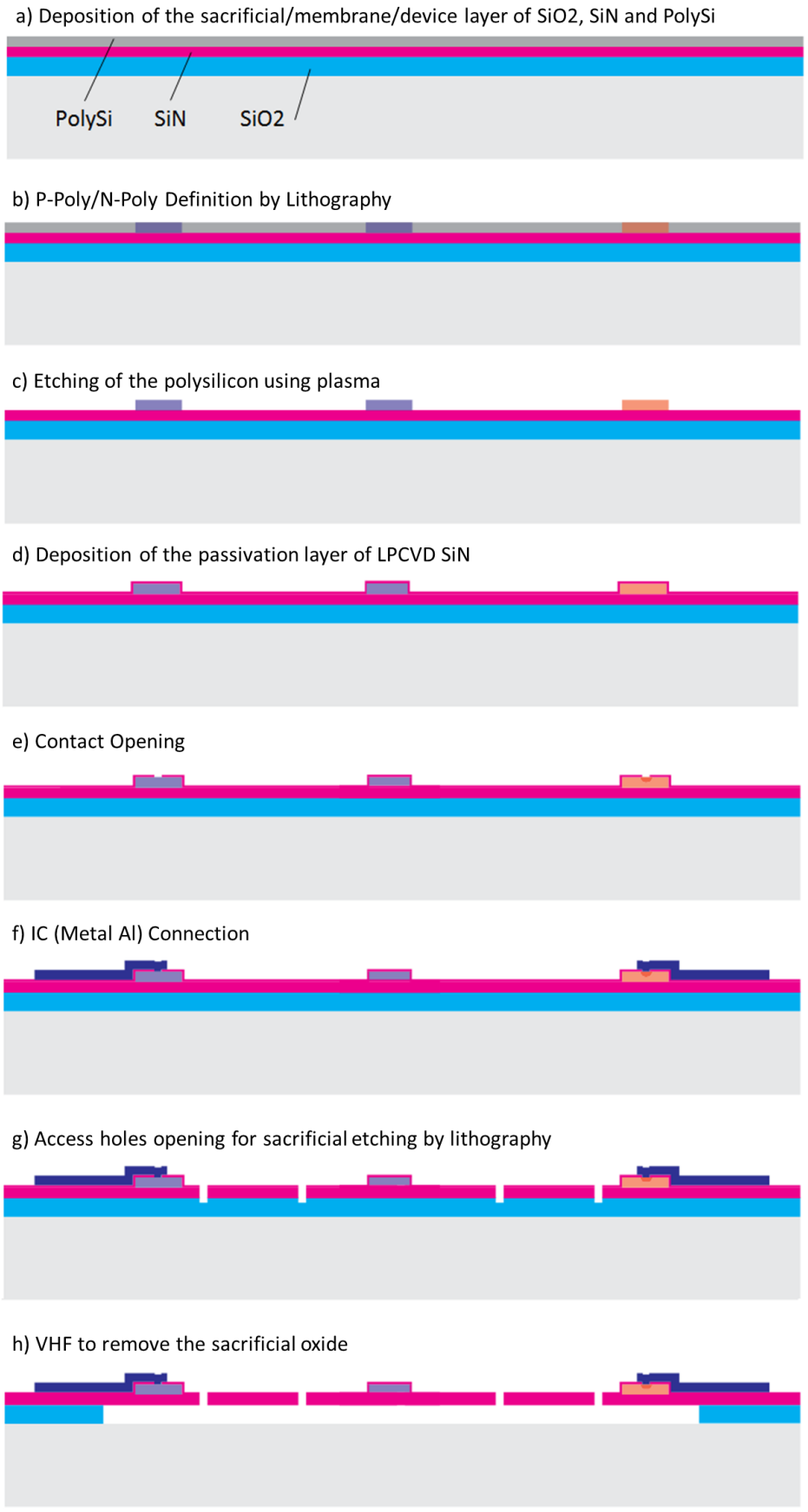

Figure 42: Fabrication process.

Silicon oxide layer with thicknesses between 5 to 10 µm were deposited on bare silicon wafers as the sacrificial layer with plasma enhanced chemical vapor deposition (PECVD) method due to its high deposition rate. Secondly, 0.6 µm low-pressure chemical vapor deposition (LPCVD) SiN as the membrane layer was deposited. Thirdly, 0.3 µm LPCVD PolySi is deposited as the device layer. These three steps are conducted in order, which makes up of Figure 42 (a). Afterwards, P poly and N poly definitions are realized by lithography, followed by Boron doping and Phosphorous doping respectively in step (b). Then, the PolySi layer is pattered and etched in using plasma etching (c). Hereafter, step (d) is fulfilled when a 200 nm SiN layer is deposited on the wafer through using LPCVD as the passivation layer, which could be used as the electrical isolated layer that prevents liquid from directly touching the surface of polysilicon during the measurement. Subsequently, N contact opening and P contact opening were performed in step (e) by lithography, dry etching and doping. Next, IC connection in step (f) that contacts opening polysilicon was realized firstly by Al sputtering which deposits a metal layer on the wafer. Then, lithography was to specifically locate the contact. Then, dry etching was used to etch extra Al and landing on SiN. Subsequently, sacrificial access holes were patterned and etched in step (g) by lithography and dry etching. Lastly, vapour HF is used in step (h) to remove the sacrificial oxide to create the under-etch.

As for fabrication, there is no doubt that the lithography is the most important parts that have been used in many steps. Furthermore, the pattern that lithography makes depends on the design of lithography mask. Thereby, to achieve different types and configurations of structures, the layout for lithography masks should be investigated in detail.

4.2 Overview of Layout

Lithography is essentially the key step in transferring design to real devices by means of the photomasks.

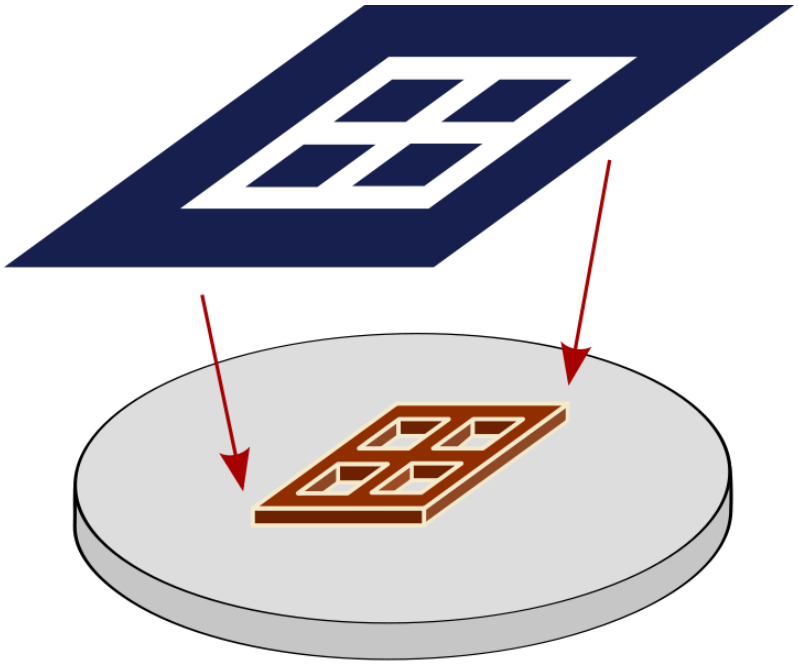

Figure 43: Schematic illustration of a lithography process [2]

Figure 43 is the typical schematic diagram of lithography process, which requires the dark blue mask on top, and integrated circuit is created using this mask when the resist is exposed with ultraviolet (UV) light.

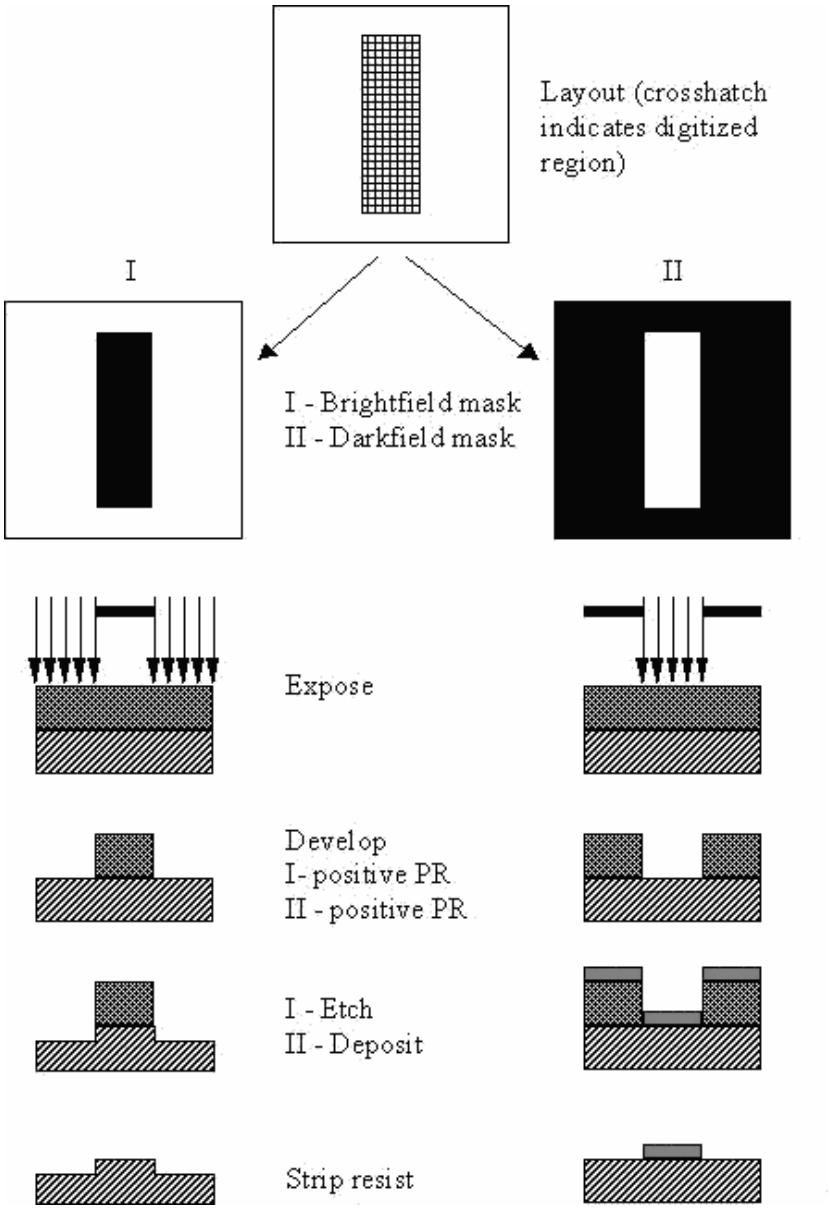

Figure 44: Positive and negative mask polarity images [3]

As shown in Figure 44, the left side is a subtractive process which uses the positive mask. In this case, the resist is exposed with UV light where the underlying material is to be removed [4]. In positive photoresist, the chemical structure of the parts that are exposed to UV light changes so that it becomes more soluble in the developer. Furthermore, the exposed resist is washed away by the develop solution, leaving windows of the bare underlying material.

At the right side of Figure 44, negative mask is shown and it behaves in the opposite way of positive mask. In our case, positive mask is used to implement the process of lithography.

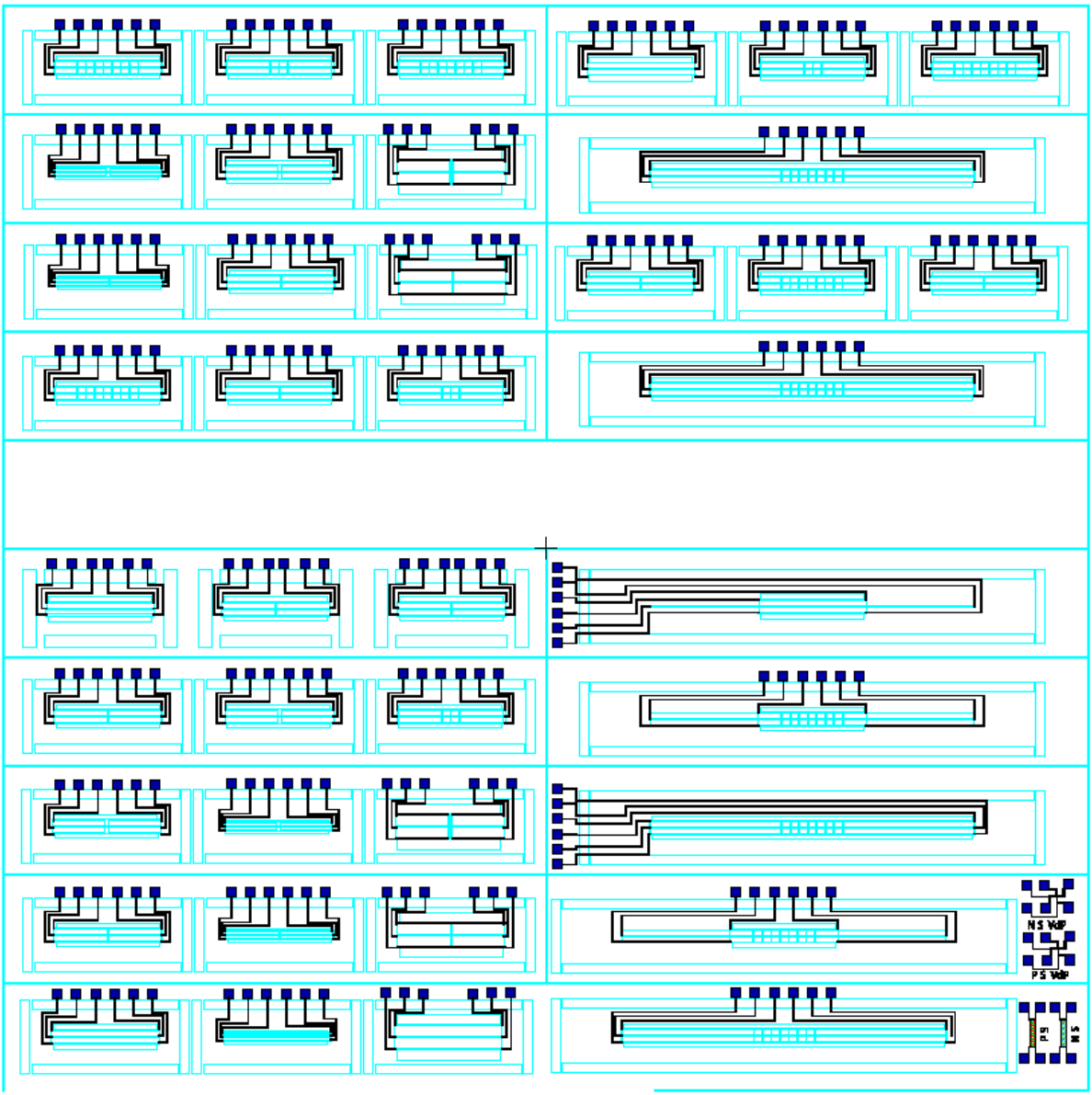

Figure 45: Overview of layout of photolithography mask

In Figure 45, the overview of layout of photolithography mask is shown. The mask was designed by L-Edit. The entire mask is in the size of 10,000 µm x 10,000 µm (10x10 mm^2). As indicated before, these structures are designed based on the different design properties. To make it more clearly, Table 4.1 is summarized to show all designed structures that corresponds to Figure 45.

Table 4.1: Overview of layout design

Structure Type	Number of thermcouples	Width of Sensors (um)	Width of thermpile (um)	Distance heater & Sensor (um)	Length of Heater (um)	Length of Sensors (um)	Dope for Heater	Dope for Sensors
TR	None	2	None	50	1000	1000	p	p
TR	None	10	None	25	1000	1000	p	p
TR	None	10	None	50	1000	1000	p	p
TR	None	10	None	100	1000	1000	p	p
TR	None	10	None	50	3000	1000	p	p
TC(CtH)	1	10	2	25	1000	1000	p	p
TC(CtH)	1	10	2	50	1000	1000	p	p
TC(CtH)	1	10	2	50	1000	1000	n	p
TC(CtH)	1	10	2	100	1000	1000	p	p
TC(CtH)	1	10	10	25	1000	1000	p	p
TC(CtH)	1	10	10	50	1000	1000	p	p
TC(CtH)	1	10	10	100	1000	1000	p	p
TC(CtH)	3	10	2	50	1000	1000	p	p
TC(CtH)	3	10	2	50	1000	1000	n	p
TC(CtH)	8	10	2	50	1000	1000	p	p
TC(CtH)	8	10	2	50	3000	1000	p	p
TC(CtH)	8	10	2	50	3000	3000	n	n
TC(CtH)	8	10	2	50	1000	1000	p	n
TC(CtH)	8	10	2	50	1000	1000	n	n
TC(CtH)(MoT)	1	10	2	25	1000	1000	p	p
TC(CtH)(MoT)	1	10	2	50	1000	1000	p	p
TC(CtH)(MoT)	1	10	2	50	1000	1000	n	p
TC(CtH)(MoT)	1	10	2	50	1000	1000	p	n
TC(CtH)(MoT)	1	10	2	50	1000	1000	n	n
TC(CtH)(MoT)	1	10	2	100	1000	1000	p	p
TC(CtH)(MoT)	1	10	10	25	1000	1000	p	p
TC(CtH)(MoT)	1	10	10	50	1000	1000	p	p
TC(CtH)(MoT)	1	10	10	50	1000	1000	n	p
TC(CtH)(MoT)	1	10	10	100	1000	1000	p	p
TC(CtH)(MoT)	3	10	2	50	1000	1000	p	p
TC(CtH)(MoT)	3	10	2	50	1000	1000	n	p
TC(CtH)(MoT)	8	10	2	50	1000	1000	p	p
TC(CtH)(MoT)	8	10	2	50	3000	1000	p	p
TC(CtH)(MoT)	8	10	2	50	3000	3000	p	p
TC(CtH)(MoT)	8	10	2	50	3000	3000	p	n
TC(CtH)(MoT)	8	10	2	50	3000	3000	n	n
TC(CtH)(MoT)	8	10	2	50	1000	1000	n	p
TR(LDP)	None	10	None	25	1000	1000	p	p
TC(CtH)(MoT)(LDP)	1	10	2	50	1000	1000	p	p
TC(CtH)(LDP)	1	10	2	50	1000	1000	p	p

As shown in Table 4.1, forty different structures are listed based on the different types of structures and design properties. A short explanation goes to the abbreviations of first column

in Table 4.1. TR is for thermos-resistors, TC is referred as thermocouple and CtH means hot-junction-closes-to-heater which is shown in Figure 32. MoT is for metal-on-top-of-heater which is shown in Figure 35. LDP means low density of Pillars which will be explained in later subsection.

Several design parameters such as distance between heater and sensor as well as width of thermopile have been presented in Chapter 3. Remaining design parameters such as number of thermocouple, length of heater and sensors, and choice of the doping type for heater and sensors will be described in the following subsections.

4.2.1 Number of Thermocouple

The effect of thermocouple on the TCD signal was briefly introduced in the last part of Chapter 3.5.3.

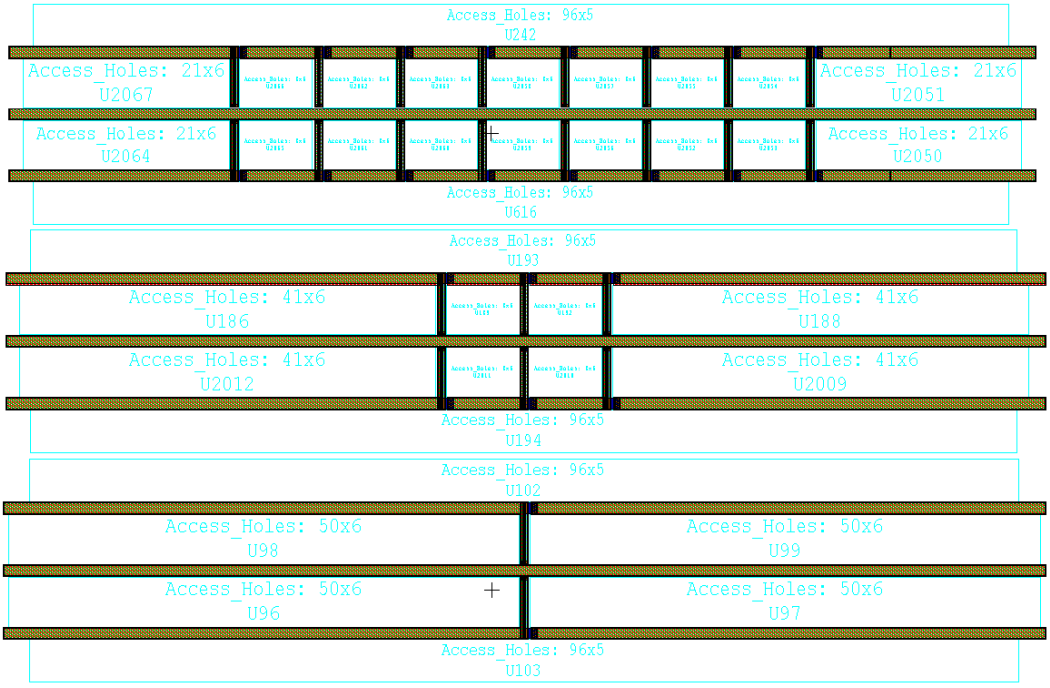

Figure 46: Different number of thermocouples (Top: 8, Middle: 3, Bottom: 1)

In Figure 46, different number of thermocouples are shown. Multiple thermocouples are placed in the same distance of 80 µm between each other. Like the discussion in Chapter 3.5.3, increasing number of thermocouple leads to multiple times of Seebeck voltage. For example, the Seebeck voltage that is generated at only one thermocouple structure is 5 mV, assuming that the same temperature difference remains the same between hot junction and cold junction

in the structure with three thermocouples, then the Seebeck voltage would be $3 \times 5\,mV = 15\,mV$ in the structure with three thermocouples. Thus, we can draw the conclusion that more thermocouple structure has multiple time of sensitivity compared to single thermocouple structure.

However, this conclusion is based on the assumption that the temperature difference between hot and cold junction remains the same at the same given electrical power in the heater. While this assumption is not quite true since multiple thermocouples would reduce this temperature difference, i.e. each thermocouple for multiple thermocouples would generates less Seebeck voltage than single thermocouple. Nevertheless, this temperature difference decrement could be somehow ignored because this decrement is much less than the increment due to multiple thermocouples. In conclusion, multiple thermocouples are always preferred to be designed due to its high sensitivity even though multiple thermocouples leads to the increment of thermal noise due to higher total resistance of thermopiles.

4.2.2 Length of Heater and Sensors

As shown in Figure 45, there are few designed structures which are bigger than the other structures. Parts of these structures are shown in Figure 47.

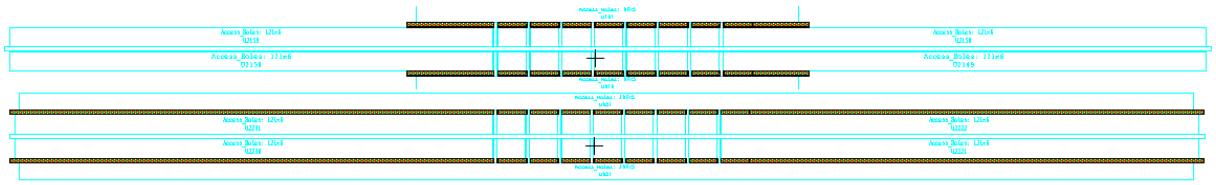

Figure 47: Different length of heater and sensors (Top: 3000 µm heater with 1000 µm sensors, Bottom: 3000 µm heater and sensors)

In Figure 47, both structures have the larger length of heater of 3000 µm compared to the regular structures that show in Figure 46. whereas, top structure's sensors are still 1000 µm long and bottom structure's sensors are 3000 µm long.

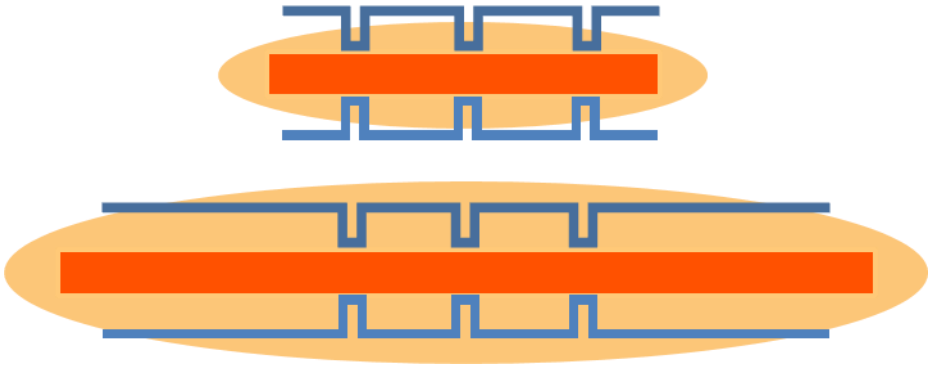

Figure 48: Thermal analysis with different length of heater (Top: short heater; Bottom: Long heater)

The reason why long heater is designed is shown in Figure 48. as it is common knowledge that the thermal(heat) distribution due to a rectangle heater is in the shape of oval. Thermal distribution is the widest around the middle of heater. To cover all the thermocouple, heater is designed as long as possible and sensors are placed as close to each other around middle as possible.

Heater is designed for the length of 3000 µm to avoid out-region of cold junction. In additions, long sensors are designed correspondingly. However, the drawback of these longer heater or sensors structures is obvious that the size of entire structure would be much more bigger than other regular structures.

4.2.3 Doping type of Heater and Sensors

As discussed in Chapter 3.4, doping level is the critical properties of determining temperature coefficient of resistance, resistivity, and Seebeck coefficient.

Figure 49: Different type of doping (n doped in light green; p doped in dark yellow)

In Figure 49, different types of doping are presented instead of different level of doping. N type and/or P type of doping are designed for heater and/or sensors respectively. As discussed in Chapter 3.4, the only property that matters in heater is resistivity. Given the same electrical voltage source in heater, the lower resistance of heater is preferred to generate more power. Then p doped for heater is desired to give more power at the same doping level.

As for sensors, since thermocouple is always the combination of n doped and p doped. The parts that matters in terms of doping-choosing is for the rest of sensors line. Thus, Seebeck coefficient does not matter anymore because the parts where are not in thermocouple are not related to Seebeck effect. Additionally, temperature coefficient of resistance (TCR) does not matter either because TCR only matters in terms of thermos-resistor (also known as thermistors). Furthermore, resistivity for the rest of sensors parts should be as low as possible

to reduce the thermal noise. Consequently, n doped is preferred to give lower resistivity at the same doping level for n and p doped.

In conclusion, p doped for heater and n doped for sensor is preferred for the structure of thermocouple. In terms of thermos-resistors (thermistors), p doped is still preferred for heater to generate more power if it is voltage-driven. P doped achieves higher TCR around $10^{17}\ cm^{-3}$ than n doped.

4.2.4 Pillars Array

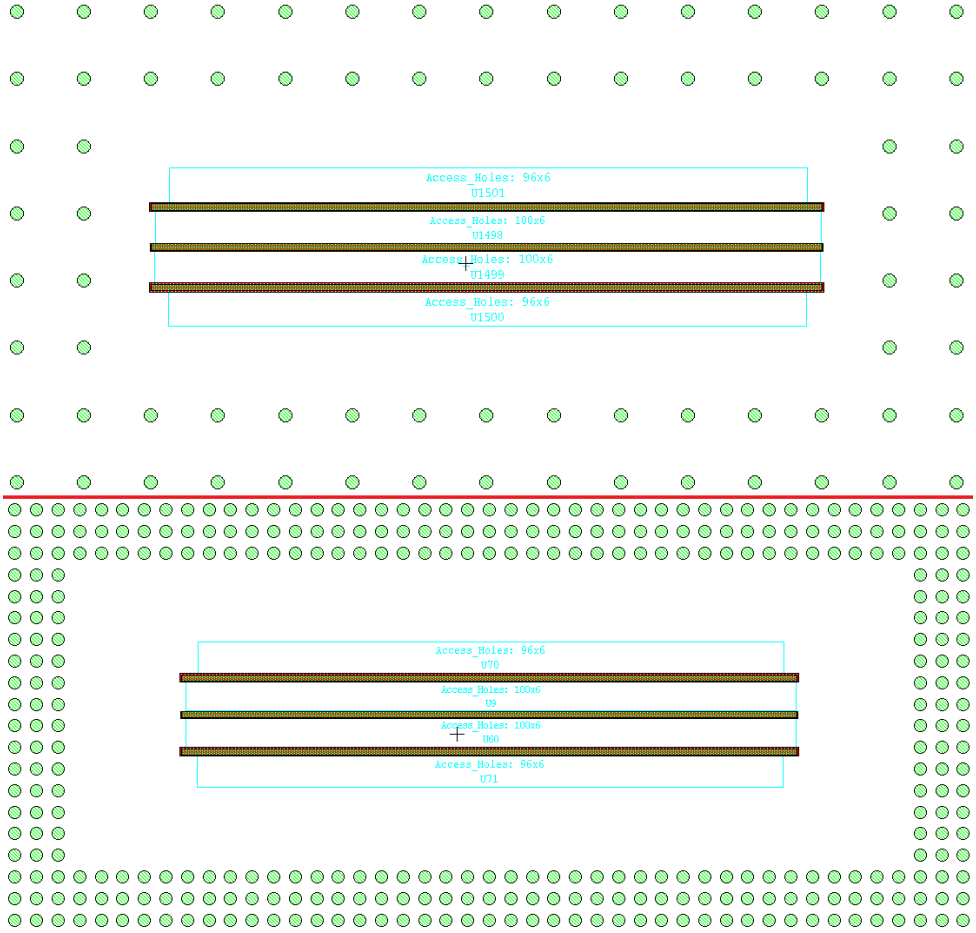

Figure 50: different density of pillar (Top: low density, Bottom: high density)

An array of polysilicon pillars were designed (Figure 50) to results in a localized hydrophilic surface, which is used for containing the liquid of fuel during the measurement. Pillar array are designed to surround the structure to maintain the liquid drop in the shape of half sphere otherwise droplet of liquid would spread flat on a wide solid surface [5-8].

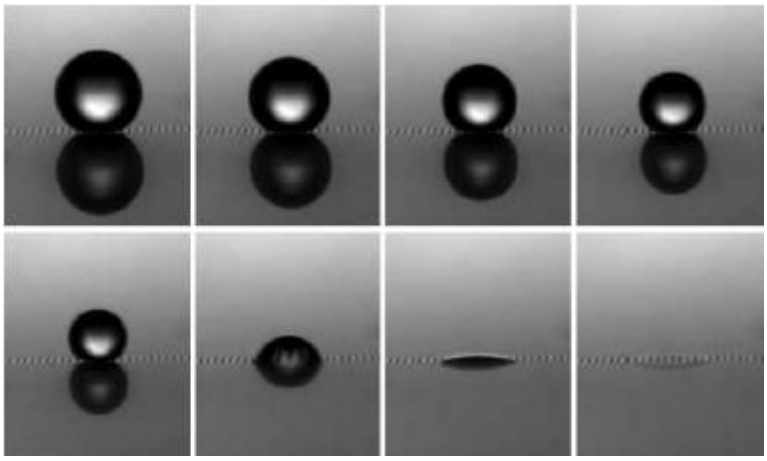

Figure 51: Diagram of liquid drop on a hydrophobic surface with pillars [8]

As shown in Figure 51, first five and last two cases are intended to be avoid on the surface of structure in our case since there is not enough interface area between liquids and structure in the first five case. Whereas last two liquids spread flat on the surface, which causes the height of liquids so small that liquids is not enough to consume the heat. Therefore, the size of each pillar and distance between each pillars are well tuned and defined to optimize the droplet surface to keep the contact angle of liquid in an acceptable range such as the sixth case in Figure 51.

4.2.5 Vertically-used structure and testing structure

Most structures that show in Figure 45 are horizontally used, which means that droplet is placed on top of the flat structure. However, some structures are designed to be used vertically, which are shown in Figure 52.

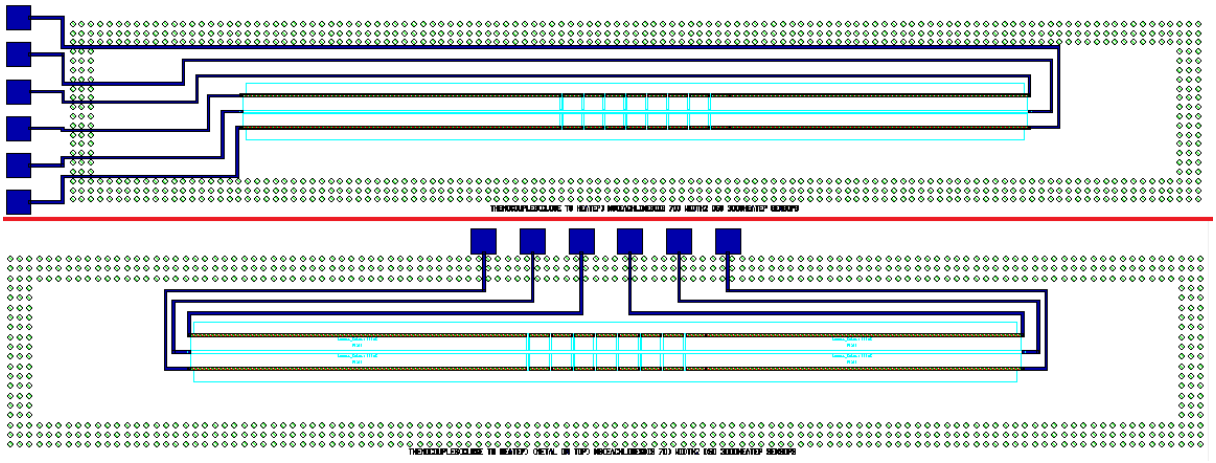

Figure 52: Vertically versus Horizontally structures (Top: Vertically-used; Bottom: Horizontally-used)

The top structure of Figure 52 is designed to be vertically used because the contact pads which are made of metal aluminium are placed at the left side of the structure. Thus, this structure could be used as a dip-stick vertically with the right parts vertically immersed in the liquid while left contact pads remain outside of the liquid. Bottom structure is the regular structure that can be used horizontally and actually also vertically, but it is clearly that the function of bottom structure are not as good as the top structure in terms of vertically-used.

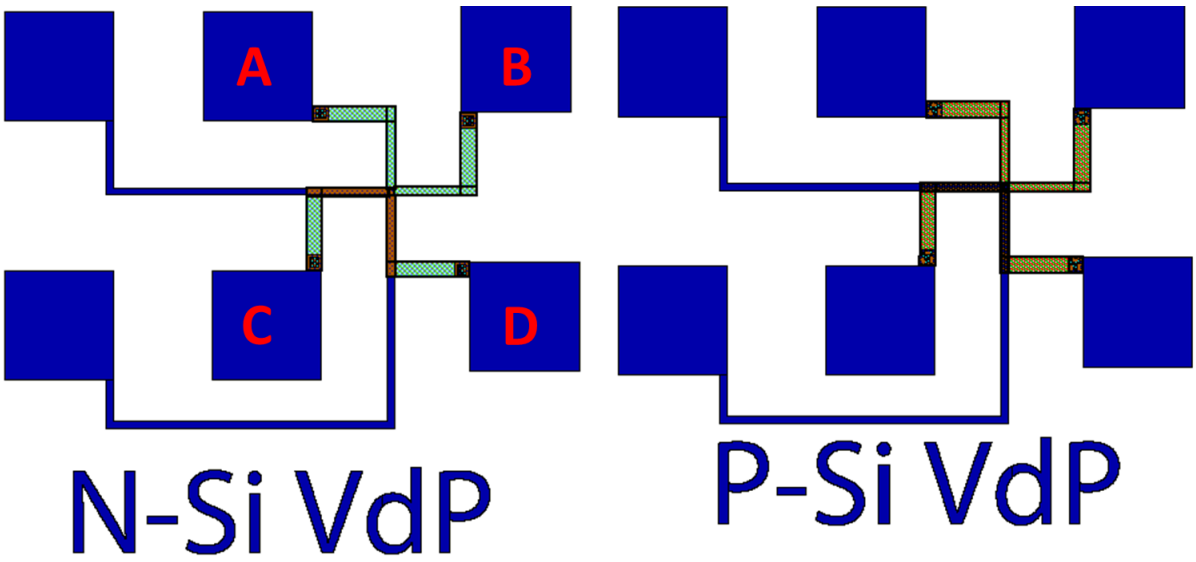

Figure 53: Van Der Pauw Structure (Left: N doped; Right: P doped)

There are few testing structures that have been designed and showed in the right bottom of Figure 45. It is more specifically showed in Figure 53 for the well-known van der Pauw structure for the measurement of sheet resistance, which was firstly introduced by L. J. van der Pauw of Philips [9]. Based on the measurement on these structures, the resistivity, doping type, sheet resistance and etc. can be determined. Take the left side of Figure 53 for instance, current is feed through pad A to C, and voltage needs to be measured between pad B and D. Furthermore, current is feed through B to C, and voltage is measured between A and D. Therefore, the sheet resistance can be derived.

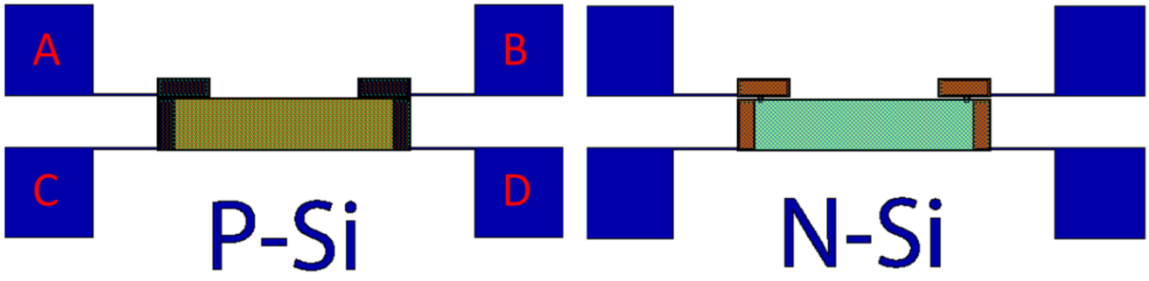

Figure 54: Test structures (Left: P doped; Right: N doped)

Another different testing structures to measure sheet resistance are showed in Figure 54. Take left side of Figure for instance, current is feed through pad C and D, then voltage between A and B can be measured. Therefore, the sheet resistance could be derived.

4.3 Fabrication results

In this subsection, the fabrication results of before-under-etch and after-under-etch will be illustrated to explain what we have achieved and state out the problem via presenting the images under Scanning Electron Microscope (SEM).

Firstly, the images under SEM before under-etch are shown in Figure 55-57.

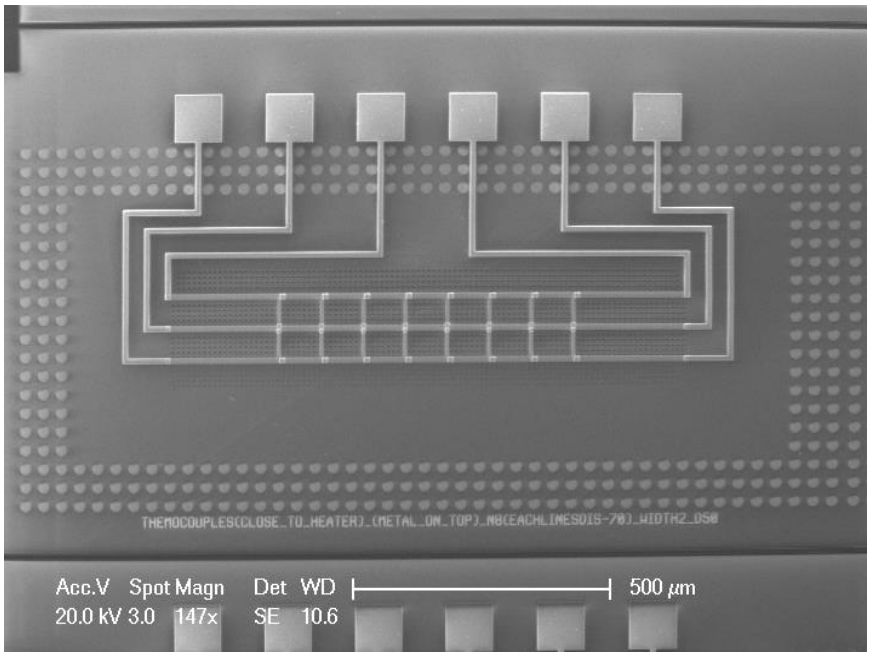

Figure 55: SEM images (thermocouple before under-etch)

Figure 55 shows the thermocouple structure before under-etch, which is corresponded to the top picture structure Figure 46. The zoom in of this images at the central part is shown in Figure 56.

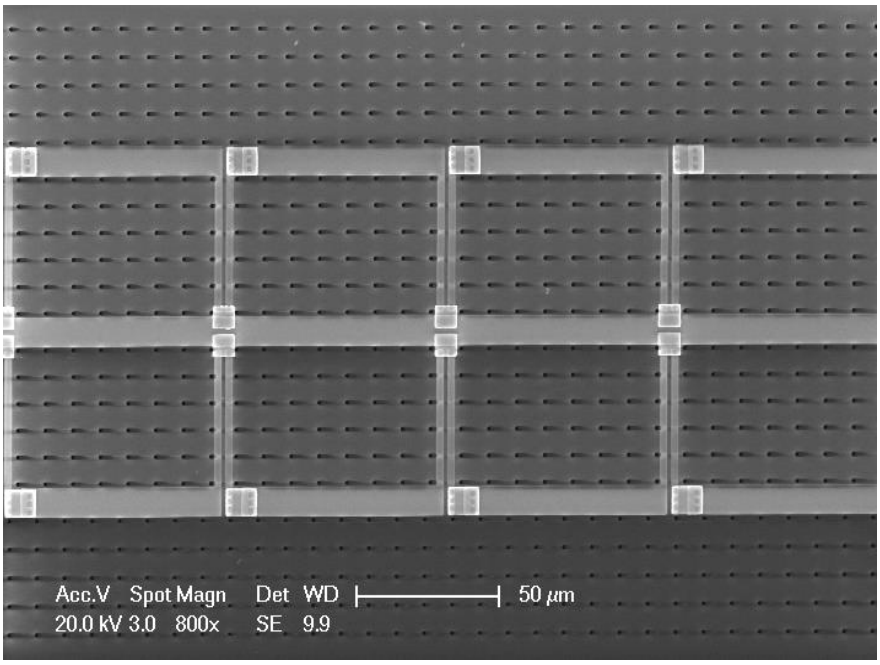

Figure 56: SEM images (thermocouple with metal-on-top zoom-in)

The access hole array could be seen clearly in the pictures. Furthermore, the spacing between each access holes are well defined because this spacing would define the under etching duration. A large spacing between the under-etching holes hence result in over etching of the membrane layer due to limited etch selectivity of the VHF. On the contrary, a short under-etching length would result to a fragile membrane.

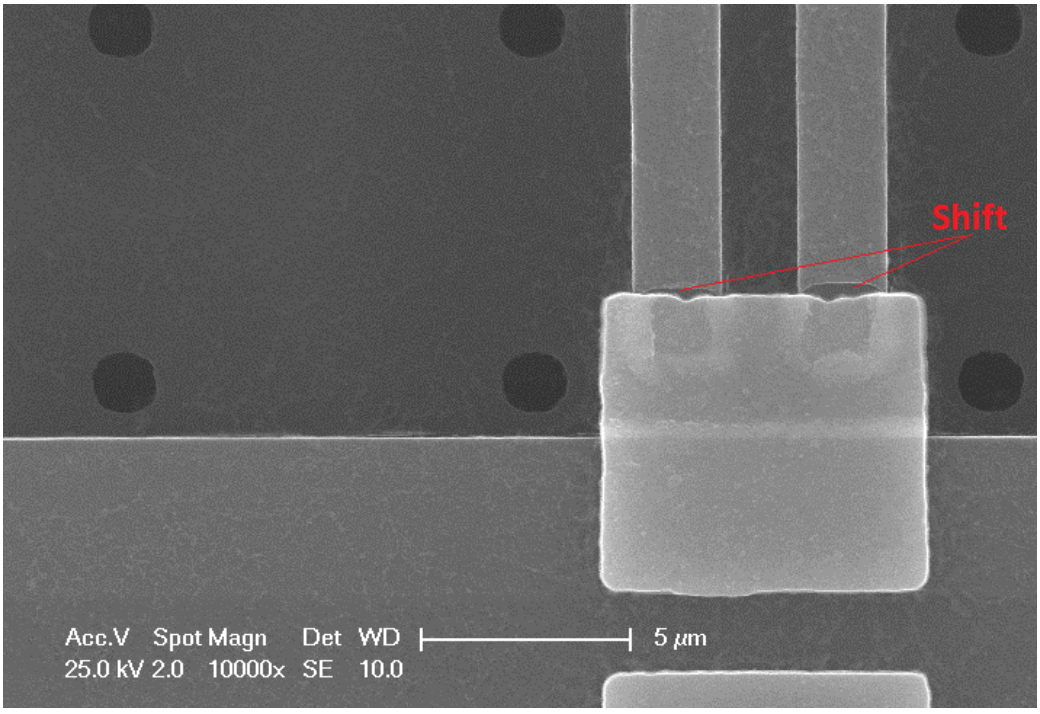

Figure 57: SEM images (metal-on-top part)

In Figure 57, the bright rectangle is the metal part that connects thermocouple and covers parts of heater, which increases the temperature of hot junction. However, as indicated in the Figure, the metal should cover the connect-holes on the polysilicon thermocouple. A certain shift happens due to non-comprehensive photolithography layout design which should be larger than it is needed since this shift is inevitable. This shift would cause a certain increment of resistance of thermocouple depending on how much it shifts. However, the thermocouple would still work unless this shift is so large that it does not cover the connect-hole on thermocouple.

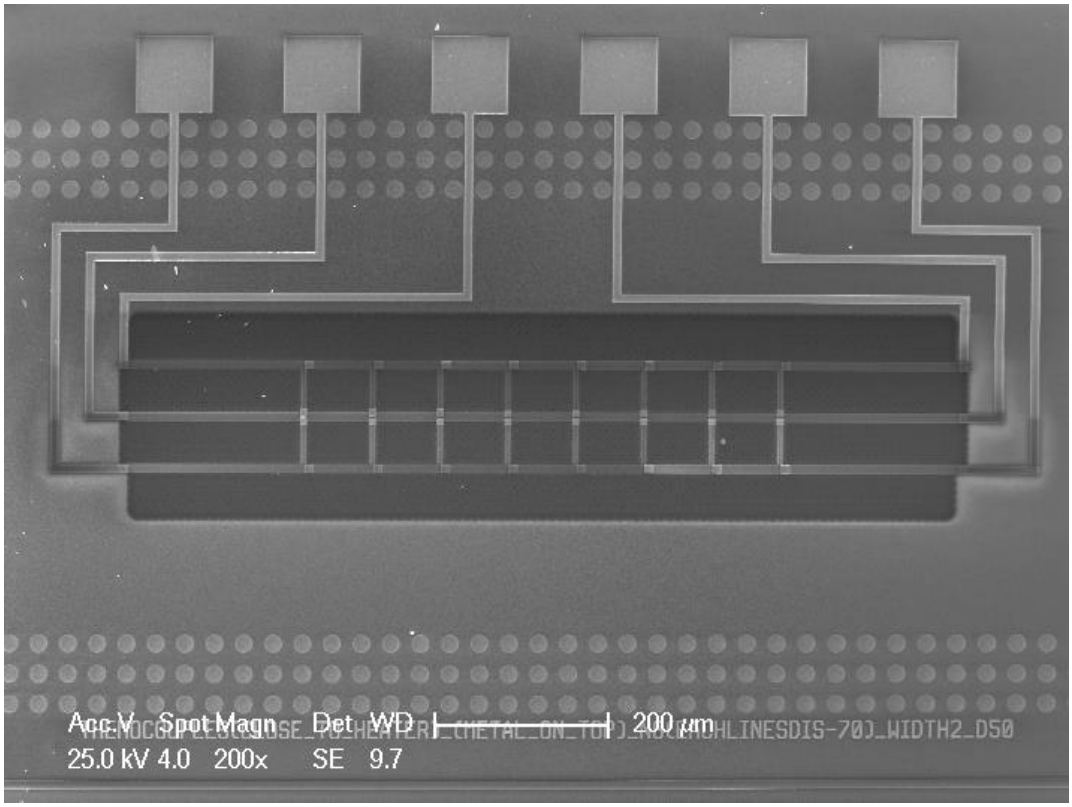

Figure 58: SEM images (thermocouple after under-etch)

Similar to Figure 55, Figure 58 shows the same structure but after under-etch. A large etch-away hole could be seen in the Figure, which prevents the heat going into the substrate as discussed in Chapter 3.5.

4.4 Conclusion

In this chapter, the general idea of fabrication was firstly presented. Followed by the detail of fabrication process which explained the procedure of fabrication. The overview of layout for

lithography was discussed, and different structure properties such as doping, length, number of thermocouple and etc. At the very last, some images under SEM concerning before and after under-etch are showed to present what we have achieved and state out the problem of shifting.

Reference

[1] Chen, Shuoxi. "Surface-micromachined thermal conductivity gas sensors for hydrogen detection." (2010).

[2] https://en.wikipedia.org/wiki/File:Mask_illustration.svg

[3] https://www.mems-exchange.org/users/masks/guidelines.html

[4] http://www.microchem.com/Prod-LithographyOverviewPosNeg.htm

[5] Susarrey-Arce, A., et al. "One-step sculpting of silicon microstructures from pillars to needles for water and oil repelling surfaces." Journal of Micromechanics and Microengineering 23.2 (2012): 025004.

[6] Yoshimitsu, Zen, et al. "Effects of surface structure on the hydrophobicity and sliding behavior of water droplets." Langmuir 18.15 (2002): 5818-5822.

[7] Gao, Jianlong, et al. "Dimensional effects of polymer pillar arrays on hydrophobicity." Surface Engineering 32.2 (2016): 125-131.

[8] Quéré, David, and Mathilde Reyssat. "Non-adhesive lotus and other hydrophobic materials." Philosophical Transactions of the Royal Society of London A: Mathematical, Physical and Engineering Sciences 366.1870 (2008): 1539-1556.

[9] van der Pauw, Leo J. "A method of measuring specific resistivity and Hall effect of discs of arbitrary shapes." Philips research reports 13 (1958): 1-9.

Chapter 5. Measurement

The fabrication process of the TCD was discussed and the results were shown in Chapter 4. The die which contains different types of thermopile, thermistor and testing structures is shown in Figure 59.

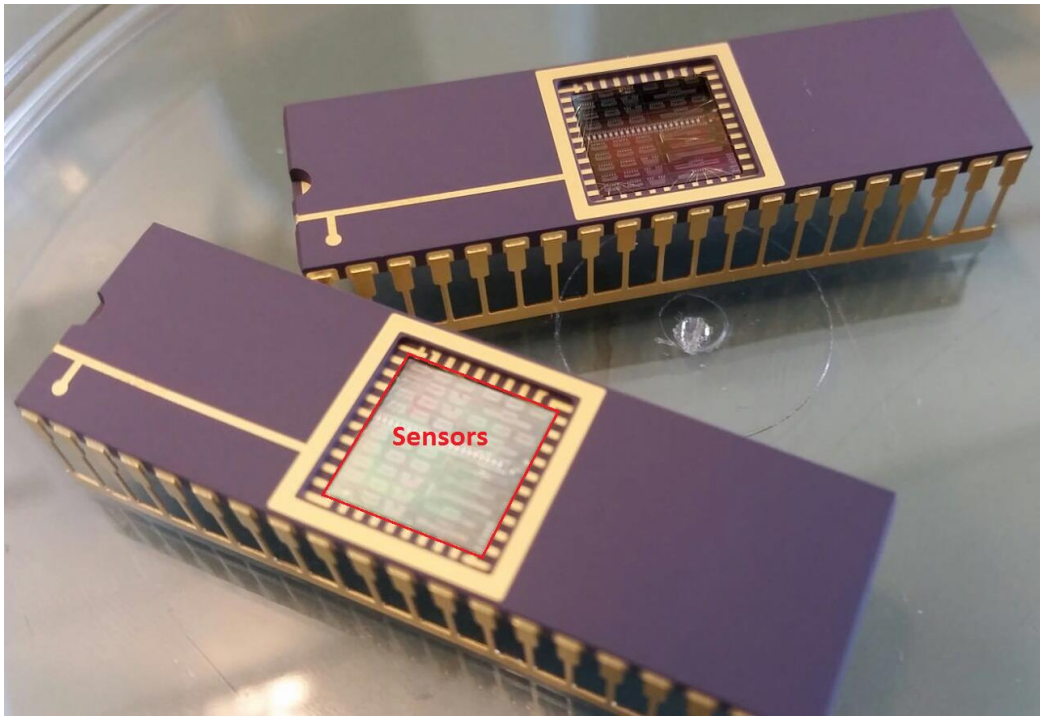

Figure 59: Die in the package

Figure 59 shows a fabricated die in a package, which is the fabrication results based on Chapter 4 and was used for measurements of liquids. A DIL40 is used for packaging, which has 40 pin-connections. However, more than 40 different sensors systems exist on this 10x10 mm^2 die, and each system has 6 pads that need to connected. Meaning that it requires at least 240 pin-connections to connect all sensors system. Therefore, only some of the sensor system can be chosen to be connected and used.

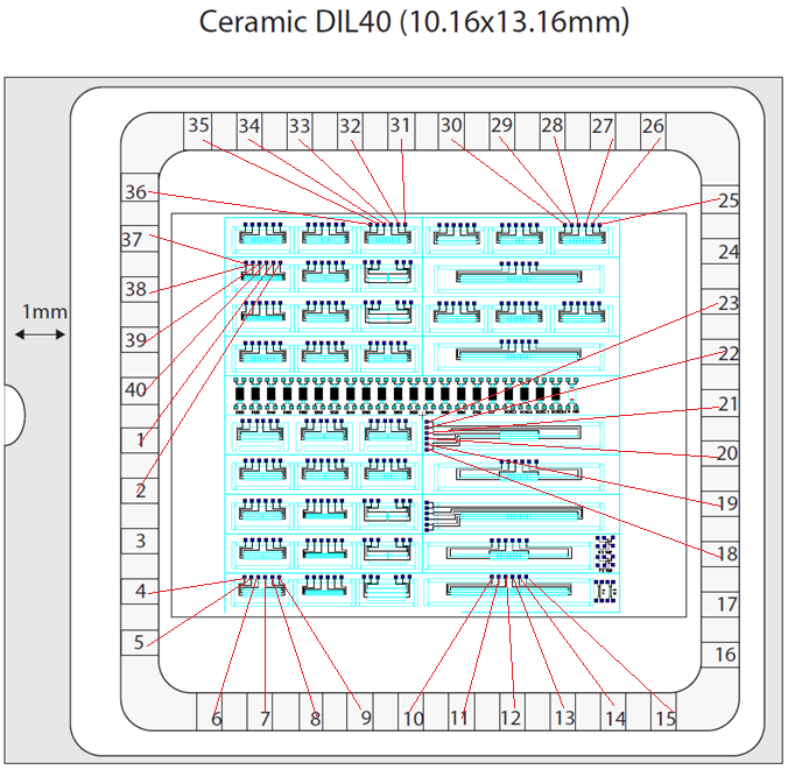

Figure 60: Wire-bonding for the package

Figure 60 shows the design of wire-bonding. Only six sensor systems are chosen to be connected depending on its structure properties. Two out of six are thermistor and other four are thermopile. Two chosen thermistors have the same length of sensors, but one with long heater of 3000 µm and another one with short heater with 1000 µm. Three out of four thermopiles have the same length of heater and sensors, but two out of these three have eight thermocouples and other one has only one thermocouple, two eight-thermocouple have different type of n and p doping. The last thermopile has 3000 µm length of heater and sensors.

Based on this package of die, different measuring and testing are conducted and showed in this chapter sequentially: Firstly, resistivity and TCR of n and p doped polysilicon are measured and presented. Secondly, Seebeck coefficient is measured via measuring the temperature difference of hot and cold junction as well as the Seebeck voltage. Thirdly, droplets of several liquids are placed on top of the package to measure the amplitude of Seebeck voltage at the frequency range of 10 – 10,000 Hz. Lastly, the conclusion of this chapter will be drawn.

5.1 Resistivity and Temperature Coefficient of Resistivity

The resistivity and the temperature coefficient of resistivity (TCR) were measured in a controlled oven over a range of 25 °C to 100 °C. Resistance was then measured by a multi-meter at a given length (L) and cross area (A). The resistivity was then can be calculated using Equation 3.9 and the results for n and p doped polysilicon is shown in Figure 61.

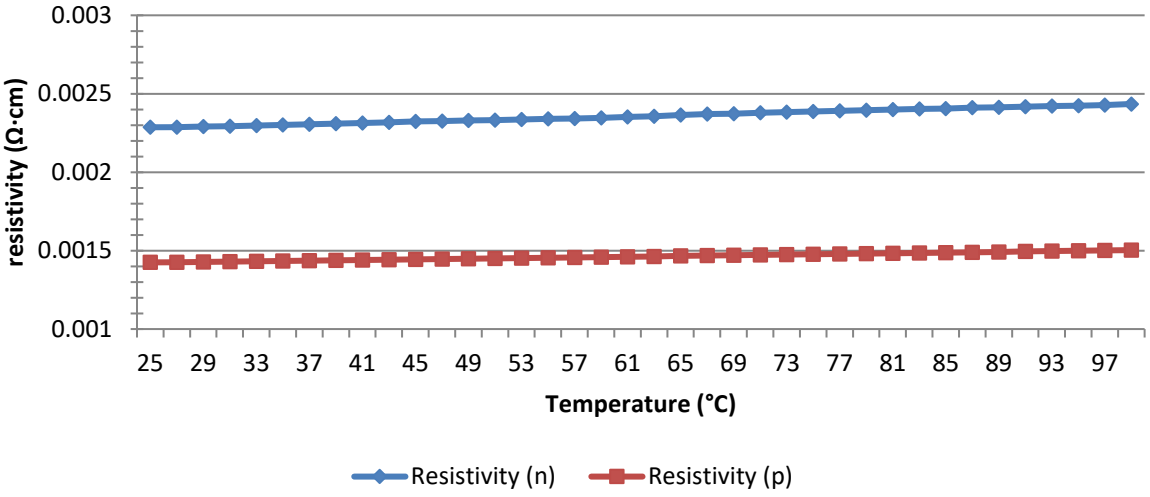

Figure 61: Resistivity of n and p doped

According to Figure 61, the resistivity of n type is around 0.15 Ω·cm and p type is around 0.24 Ω·cm, which is lower than the expected resistivity of 0.5 Ω·cm that was discussed in Chapter 3.4. This is due to the fact that the doping level during fabrication was different from what we have designed, and this variation of doping level results in the variation of resistivity.

The thermal coefficient of resistivity discussed in Equation 3.7 in Section 3.3 shows only the first order TCR of α. However, this equation can be extended to include the second order TCR of β, as shown in Equation 5.1 below.

$$R = R_{ref}[1 + \alpha(T - T_{ref}) + \beta(T - T_{ref})^2] \quad (5.1)$$

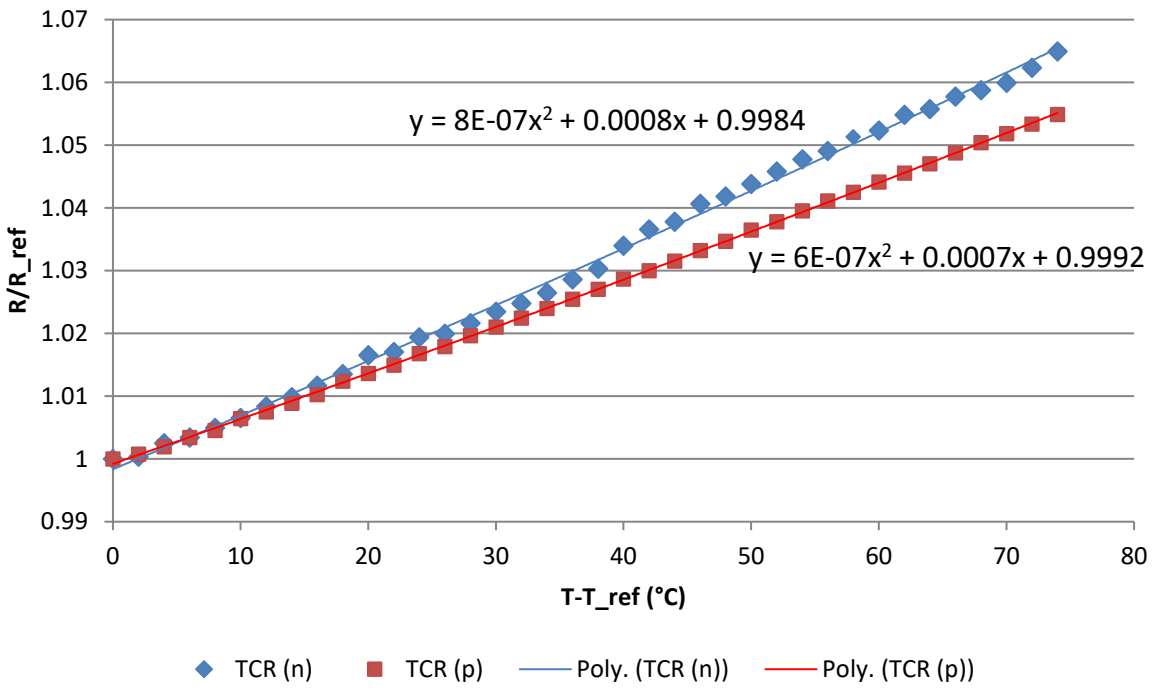

Figure 62: TCR of n and p doped

The variation of resistivity with respect to the temperature difference is shown in Figure 62. In this figure the x axis is $(T - T_{ref})$, and y axis is R/R_{ref} where T_{ref} and R_{ref} are respectively the room temperature (25 °C) and the resistivity of polysilicon at room temperature. The polynomial trend-line was fitted over the data and showed in the figure. The α for n doped is 0.0008 and α for p doped is around 0.0007. Second order coefficient β for n doped is 8×10^{-7}, and β for p doped is 6×10^{-7}. The measured TCRs in Figure 62 are a little higher than the theoretical results in Figure 11 and 12 which are based on doping level according to the measured resistivity in Figure 61. These deviations would not affect the performance of TCD significantly since these TCRs are close to the minimum values.

5.2 Seebeck Coefficient

The Seebeck coefficient can be derived based on Equation 5.2.

$$S = \frac{\Delta V}{\Delta T} = \frac{V_{Seebeck}}{T_{hot} - T_{cold}} \tag{5.2}$$

The Seebeck coefficient can be derived by measuring the Seebeck voltage and Temperature of hot and cold junction, and the temperature difference can be derived by measuring the

resistance of heater and sensors. Here the temperature of the cold junction was assumed to be the room temperature.

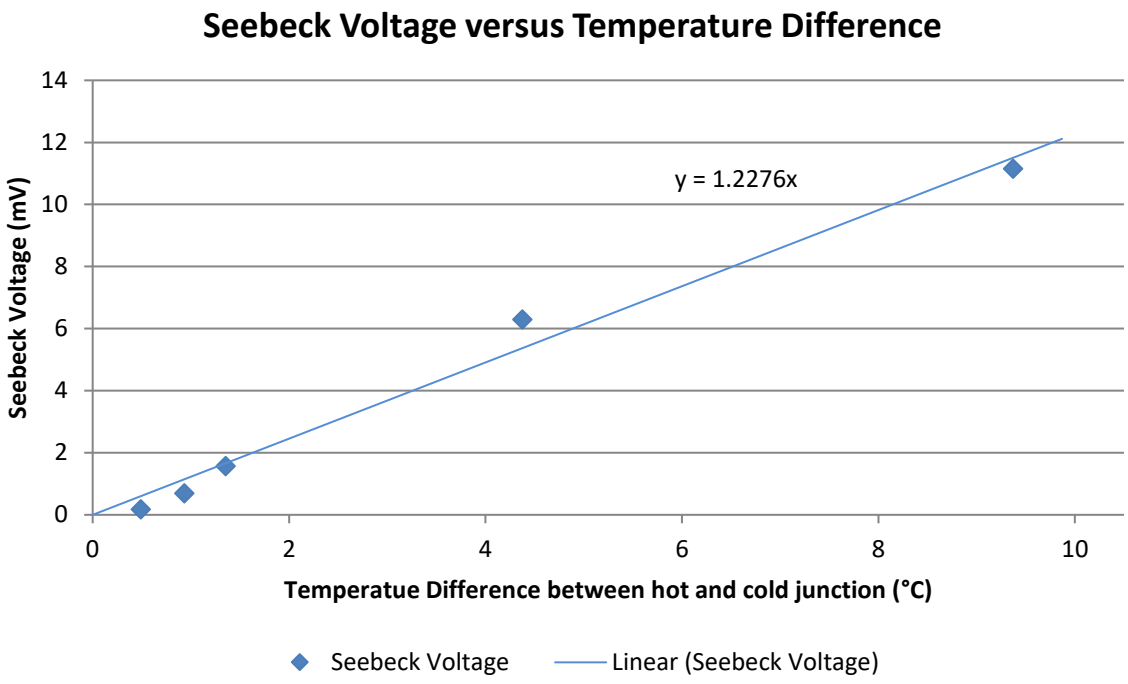

Figure 63: Seebeck Voltage versus Temperature Difference

In Figure 63, Seebeck voltage versus temperature difference under air is shown. Linear fit over the data points is shown in Figure 63. According to Equation 5.2, the slope of this trend-line should be the Seebeck Coefficient, which is 1.2276 mV/ °C. However, this number should be divided by 8 since there are 8 thermocouple in the thermopile, which should be 0.153 mV/ °C (which is larger than type K (chromel-alumel) of 41 $\mu V/℃$ [1], thanks to the use of polysilicon). This result is in agreement with the model data presented in Figure 14 and 15. The calculated Seebeck coefficient is less than expected because the temperature of hot junction was regarded as the temperature of heater, whereas the temperature of heater is expected to be higher than hot junction. By doing so, the denominator of Equation 5.2 was increased, which leads to the decrease of calculated Seebeck coefficient. The temperature of hot junction is replaced by the temperature of heater because the temperature of hot junction cannot be measured directly while temperature of heater can be derived by measuring the resistance of heater associated with the TCR in Figure 62.

5.3 Liquid Measurement

In this section, droplet of different liquids are placed on top of the device to measure the frequency-dependence second harmonic Seebeck voltage. A droplet of water on top of device is showed in Figure 64.

Figure 64: Droplet on top of device

A pipette, shown in Figure 65, was used for putting droplet on the surface of device. In Figure 64, a DI water droplet was placed on surface of device which formed shape of a sphere as was expected. However, droplet of ethanol or gasoline does not form the shape of sphere during measurement due to the higher surface tension of water than ethanol and gasoline. Thus, droplet of gasoline or ethanol spread on the surface of device. The pillar array that was discussed in Figure 51 in Chapter 4.2.4 does not shaped ethanol or gasoline into sphere because the height of pillars were too small designed.

Figure 65: Pipette for droplet

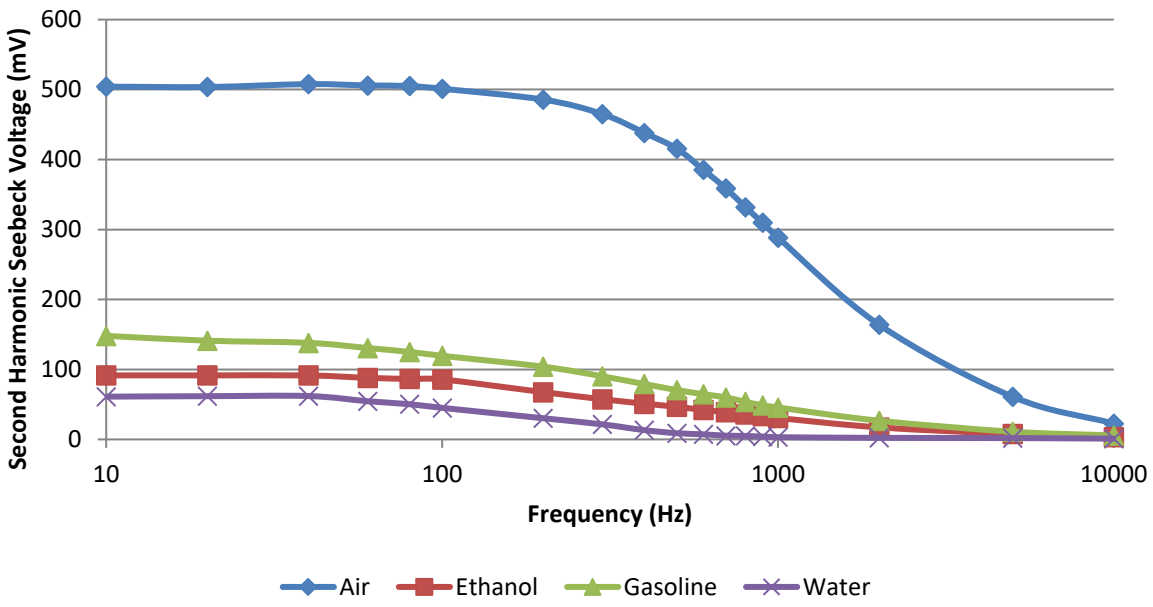

Figure 66: Second Harmonic Seebeck Voltage

A sine wave voltage was generated using a Lock-in amplifier (SR830) at different frequencies and amplitudes and was used to power the heater. The output of the thermopile is then measured by the Lock-in amplifier. The second harmonic component of the measured voltage corresponds to the Seebeck voltage. Figure 66 shows the measurement results for different liquids at different frequencies. The measured Seebeck voltage for the air shows a clear first order system behaviour with a pole at 635 Hz. The response of the TCD to the other liquids cannot be as easily analysed. This is mainly due to the fact that the pole is at a very low frequency as it was also expected from the simulation results. In order to find the poles for the liquids more easily, the data is log-log plotted in Figure 67. Spectral response curves could be summarized as DC impedance and pole position. In Figure 66 and 67, DC impedance for air was around 538 mV, ethanol was around 78 mV, gasoline was around 132 mV and water was around 68 mV. The -3dB poles calculated for air was around 635 Hz, gasoline was around 251 Hz, ethanol was around 333 Hz and water was around 116 Hz.

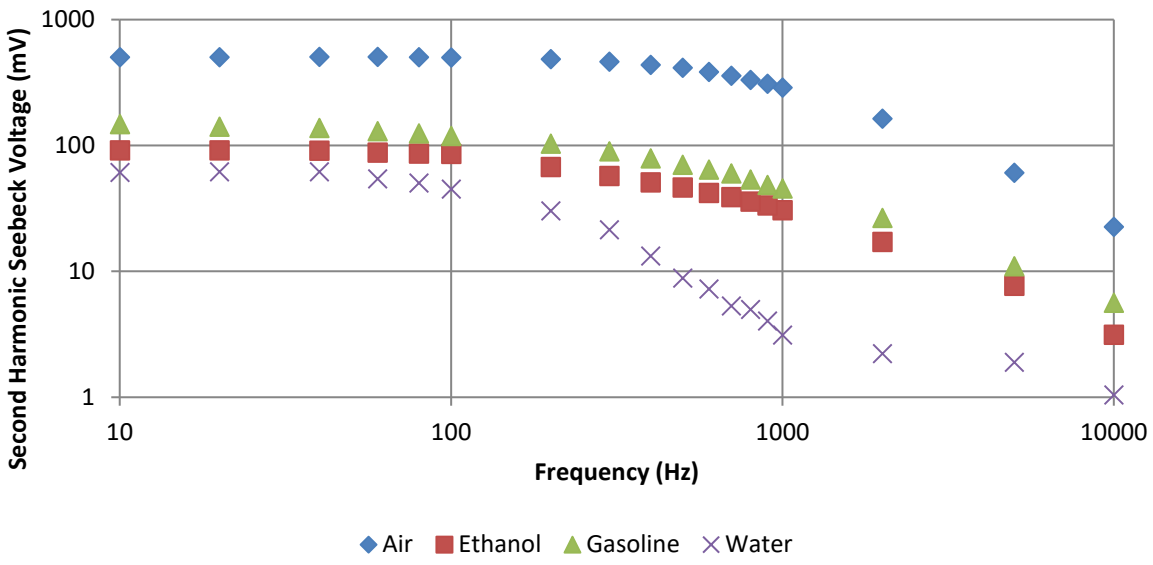

Figure 67: Second Harmonic Seebeck Voltage (both x and y axis in logarithmic)

From the frequency responses of the thermal equivalent circuit shown in Figure 8, the pole for water can be calculated as 438 Hz, ethanol 940 Hz and gasoline around 1130 Hz. However, these results were simulated based on a TCD fabricated on top of a silicon substrate. The measurement results are however, obtained using under-etched devices. This results in a higher thermal isolation hence a lower measured pole of the system. It should be noted that the results shown in Figure 23 on the other hand correspond to case were under-etching is filled with air, whereas in the current devices the liquid penetrates and fill the gap under the membrane. Therefore, a more accurate modelling is required to obtain the correct response.

Several challenges were also encountered during the measurement of the sensors. Firstly, sensor has some offset primarily due to the gradual heating of the whole liquid. Therefore, the temperature difference between cold and hot junction would be different which results in an offset in measurements. Secondly, the disturbance such as air flow around device, which comes from surrounding is inevitable during the measurement. Thirdly, the fuel resources were not well sealed and have been preserved for a long time, while most importantly, these fuel resources such as ethanol would absorb water from air. Gasoline blends without ethanol would have a shelf life of many years if well sealed [2]. Lastly, droplet of ethanol/gasoline blend evaporates within a minute, which requires continually-adding of droplet while it usually takes a few seconds for heating up and electronic instrumentation's response, this causes insufficient interface between fuel and sensors surface, which further leads to unstable measured results.

Table 5.1 can be used to summarize the measured (Figure 66 and 67) and simulated results (Figure 8 and Table 3.2) in terms of DC impedance and poles positions for different liquids. The unit of DC impedance for measured and simulation results are different but somehow useful to refer to.

Table 5.1: DC impedance and Pole position for measured and simulation results

Liquid	DC Impedance [mV](Measured)	Pole Position [Hz](Measured)	DC Impedance [K/W](Simulation)	Pole Position [Hz](Simulation)
Ethanol	78	333	2540.38	940
Gasoline	132	251	3031.52	1130
Water	68	116	784.01	438

5.4 Conclusion

In this chapter, TCD device, packaging and measurement set-up were introduced. Secondly, resistivity and TCR for n and p doped were measured, and some deviation were found compared to design but still at an acceptable range. Seebeck Coefficient were measured to test the performance of thermopile. Lastly, liquids measurement were conducted for thermopile to measure the second harmonic Seebeck voltage which agree to the simulation results and thermal equivalent circuit model. Instead of measuring both real and imaginary part of the signals, we only measured the real part because the imaginary part (phase) was not stable and trustworthy during the measurement. Thermos-resistors, on the other hand, were not tested due to the limitation of time.

Reference

[1]http://www.analog.com/en/analog-dialogue/articles/measuring-temp-using-thermocouples.html

[2] http://www.fuel-testers.com/expiration_of_ethanol_gas.html

Chapter 6. Conclusions and future work

6.1 Conclusions

In this thesis, a fuel sensor that is capable of determining the composition of the ternary mixture of ethanol, water and gasoline has been presented. Operation is based on thermal impedance spectroscopy. The main design challenge is to have the heat injected into the liquid rather than the substrate and to have a temperature-difference measurement not affected by the presence of the thermal conductive substrate. Two types of sensors were designed to achieve bio-fuel composition sensing: The first type is composed of a thermo-resistor (thermistor) for heating and temperature sensing at the heat injection node and two thermoresistors on either side at a well-defined distance. The second type is composed of the same heater/thermoresistor, but with thermopile to measure the temperature difference due to injected heat.

Since injected heat is an energy, the squared value of the amplitude of the current injected at the heater node is taken for the heat and the resulting temperature rise between the heater node and the sensing node. Therefore, the amplitudes of second harmonic of the Seebeck voltage is taken. The preliminary study has shown that frequency band of interest in the range of 10 to 10000 Hz. These two types of sensors were designed, integrated and fabricated on a 10×10 mm^2 die based on the different parameters, such as: doping type (n or p), length (1000 µm or 3000 µm) and width (2 µm or 10 µm) of heater and sensor as well as different distance (25 µm or 50 µm or 100 µm) between heater and sensor for thermistor while doping type (n or p) and length (1000 µm or 3000 µm) of heater and sensor, number of thermocouples in the thermopile (1 or 3 or 8) and width (2 µm or 10 µm) of thermocouple, as well as different distance (25 µm or 50 µm or 100 µm) between heater node and sensor node.

Special features have been explored for improved performance, such as structures with the hot-junction-close-to-heater, metal-on-top and SiN-with-metal-on-top and implemented in different thermopile designs. Most of the structures are based on thermopiles, with 34 out of 40 sensor designs on the chip layout thermopiles and 6 out of 40 sensors all-thermistor design. A CMOS compatible design flow was design and successfully implemented for the fabrication of actual devices. Under-etch of 5 to 10 µm was designed and realized to increase heat flux injection efficiency into the liquid instead of substrate. Devices were tested and performance was in reasonable agreement with simulations in terms of DC impedance and

poles positions but discrepancies results from electrical noise and offset of measurement instrumentation, disturbance from surrounding, contamination of fuel and evaporation of fuel during measurement.

The measurement results on resistivity demonstrated that a too high implantation dose was used for fabrication. Reducing the dose from $2 \times 10^{18}\ N/cm^{-3}$ to $2.4 \times 10^{17}\ N/cm^{-3}$ for n dope and from $2 \times 10^{18}\ N/cm^{-3}$to $10^{18}\ N/cm^{-3}$ for p dope, TCR and Seebeck coefficient were also different from expectation, due to the different doping concentrations. However, good agreement was obtained after running the simulations at the actual values, Measuring were based on the second harmonic of the Seebeck voltage and demonstrated basic operation. Typical power consumption is 0.13 mW.

Compared to electrical impedance spectroscopy and other state-of-the-art fuel sensors, the approach of thermal impedance spectroscopy are described in this thesis for the first time is capable of determining ternary mixtures using only one physical domain. This feature has high potential for reducing system complexity as compared system operating different domains.

6.2 Future work

Improvement on the measurement and design of readout circuit could be the main work that needs to be done in the future work. Suggestion for future work on this project are summarized as follows:

- As shown in Figure 59, the whole die of 10 x 10 mm^2 was used for the packaging with 40 pins. However, this die consists of 40 different sensor systems which could be diced into small dies and replaced by a package with only 6 pins. By doing so, the area of each device could be reduced considerably.
- More measurements should be conducted for a certain different gasoline blends such as E10, E22 and E85 and other, which was the initial intention of this project and this thesis.
- A dedicated package could be made using 3D printing to prevent the evaporation of liquid during measurement.
- The ‘dipstick’ design should be improved to enable continuous biofuel composition measurement rather than by sampling.

- The special surface profiling tested for having a localized hydrophilic surface did not work as planned. This idea should again be investigated in more detail.
- Measurements were mainly on thermopiles. The 3-omega technique should be implemented to enable the testing of the all-thermoresistor designs.
- Dedicated readout circuit should be designed for providing gain of the Seebeck and for interfacing the off-chip lock-in amplifier, as shown schematically and simplified in Figure 69.

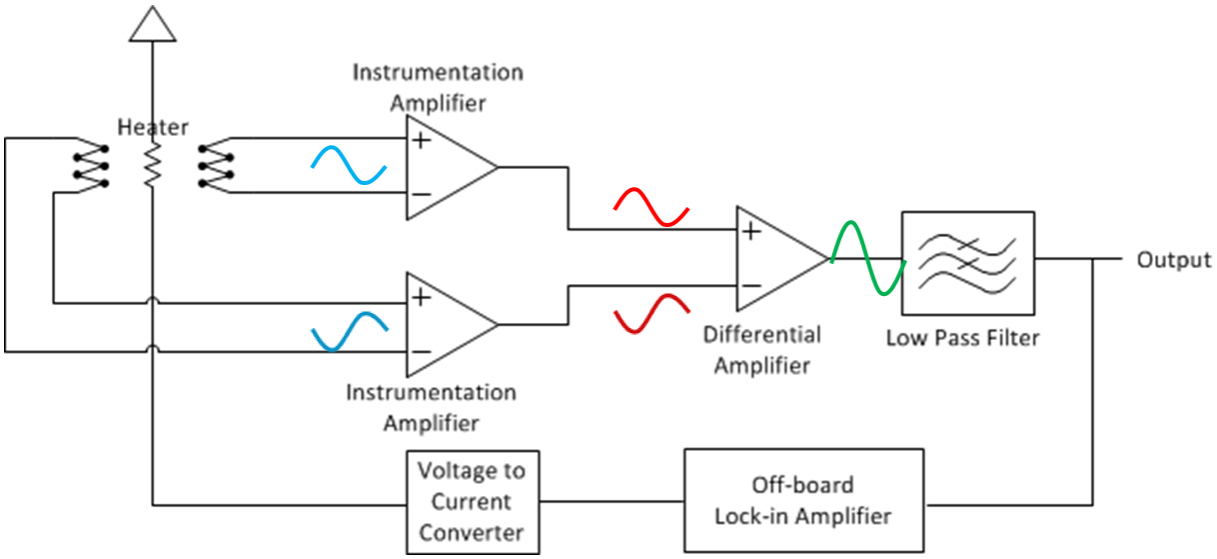

Figure 68: Proposed readout circuit

In Figure 69, instrumentation amplifiers such as AD8429 are used as preamplifier due to its high CMRR based on three-op-amp topology. Followed by the differential amplifier that further amplifies the difference of two inputs and cuts off offset. Low pass filter filters out the unnecessary low frequency range signals noise. The output is measured by off-board Lock-in amplifier and followed by voltage to current converter which provides some amplification and transfers the voltage signal into current sources to the heater.